

UNIVERSITÀ DEGLI STUDI DI NAPOLI FEDERICO II



PhD IN CHEMICAL SCIENCES

XXVII CYCLE

***DEVELOPMENT OF LAB-ON-CHIP INTEGRATED  
SYSTEMS BASED ON BLOCK COPOLYMERS FOR  
ADVANCED SENSING***

**SUPERVISORS**

PROF. CLAUDIO DE ROSA  
PROF. FINIZIA AURIEMMA

**COORDINATOR**

PROF. LUIGI PADUANO

**PhD STUDENT**

ANNA MALAFRONTE

# INDEX

## **CHAPTER I - BLOCK COPOLYMERS NANOSTRUCTURES AND DESCRIPTION OF THE THESIS WORK**

	<b>PAG.</b>
<b>1.1</b> Introduction to Chapter I	<b>1</b>
<b>1.2</b> Block Copolymers: general principles and morphologies	<b>4</b>
<b>1.3</b> Orientation of block copolymer morphologies on long-range scale	<b>9</b>
<b>1.3.1</b> Solvent evaporation	<b>10</b>
<b>1.3.2</b> Directional eutectic crystallization and epitaxy	<b>11</b>
<b>1.4</b> Applications of block copolymers	<b>15</b>
<b>1.4.1</b> Block copolymers based nanocomposites	<b>16</b>
<b>1.4.2</b> Block copolymers based nanoporous materials	<b>19</b>
<b>1.4.3</b> Block copolymers as additive to create nanostructured resins	<b>23</b>
<b>1.5</b> Description of the thesis work	<b>29</b>
Bibliography of Chapter I	<b>32</b>

## **CHAPTER II - NANOCOMPOSITES BASED ON POLYSTYRENE-*BLOCK*-POLY(ETHYLENE OXIDE) COPOLYMERS (PS-*b*-PEO) AND PALLADIUM NANOPARTICLES**

	<b>PAG.</b>
<b>2.1</b> Introduction to Chapter II	<b>37</b>
<b>2.2</b> Materials and Methods	<b>39</b>

<b>2.3</b>	Results and discussion	<b>43</b>
<b>2.3.1</b>	Characterization of as received block copolymers (BCPs)	<b>43</b>
<b>2.3.2</b>	Preparation and characterization of thin films of the neat BCPs and BCP nanocomposites containing Pd precursor	<b>58</b>
<b>2.3.3</b>	BCP-based nanocomposites with Pd nanoparticles prepared in solution	<b>64</b>
<b>2.3.4</b>	Preparation of PdO nanoparticles on silicon substrates	<b>72</b>
<b>2.4</b>	Conclusions to Chapter II	<b>76</b>
	Bibliography of Chapter II	<b>78</b>

**CHAPTER III - BLOCK COPOLYMERS BASED NANOPOROUS MATERIALS FOR BIOMOLECULES IMMOBILIZATION**

		<b>PAG.</b>
<b>3.1</b>	Introduction to Chapter III	<b>81</b>
<b>3.1.1</b>	Biosensors: general principles	<b>81</b>
<b>3.1.2</b>	Immobilization of the biological element	<b>83</b>
<b>3.1.3</b>	Description of the chapter work	<b>89</b>
<b>3.2</b>	Materials and Methods	<b>93</b>
<b>3.2.1</b>	Materials	<b>93</b>
<b>3.2.2</b>	Preparation and characterization of the nanomaterials	<b>94</b>
<b>3.2.3</b>	Experiments of myoglobin adsorption	<b>96</b>
<b>3.2.4</b>	Experiments of peroxidase activity	<b>98</b>
<b>3.2.5</b>	Experiments of <i>esterase 2</i> activity	<b>100</b>
<b>3.3</b>	Preparation and characterization of the nanoporous material	<b>102</b>

<b>3.4</b>	Experiments of myoglobin adsorption	<b>114</b>
<b>3.5</b>	Catalytic performance of immobilized Horseradish Peroxidase (HRP)	<b>126</b>
<b>3.6</b>	Immobilized Esterase 2 (EST2) as biosensor for the detection of specific organophosphate pesticides	<b>135</b>
<b>3.6.1</b>	Catalytic performance of immobilized EST2	<b>137</b>
<b>3.6.2</b>	EST2 residual activity after contact with paraoxon	<b>142</b>
<b>3.7</b>	Conclusions to Chapter III	<b>147</b>
	Bibliography of Chapter III	<b>148</b>

**CHAPTER IV - DIMETHACRYLATE BASED PHOTOPOLYMERIC SYSTEMS  
MODIFIED WITH A POLYSTYRENE-BLOCK-POLY(ETHYLENE OXIDE)  
COPOLYMER FOR 3D PRINTING**

	<b>PAG.</b>	
<b>4.1</b>	Introduction to Chapter IV	<b>153</b>
<b>4.2</b>	Materials and Methods	<b>160</b>
<b>4.3</b>	Results and discussion	<b>163</b>
<b>4.3.1</b>	Fourier transform infrared spectroscopy (FT-IR) measurements	<b>163</b>
<b>4.3.2</b>	Differential scanning calorimetry (DSC) experiments	<b>169</b>
<b>4.3.3</b>	Small-Angle X-ray Scattering (SAXS) and transmission electron microscopy (TEM) experiments	<b>174</b>
<b>4.4</b>	Conclusions to Chapter IV	<b>178</b>
	Bibliography of Chapter IV	<b>179</b>
	<b><u>CONCLUSIONS</u></b>	<b>180</b>
	<b><u>APPENDIX</u></b>	<b>185</b>

---

---

# CHAPTER I

---

---

## **BLOCK COPOLYMERS NANOSTRUCTURES AND DESCRIPTION OF THE THESIS WORK**

### **1.1 Introduction to Chapter 1**

Today's materials science deals increasingly with nanostructures, that is, with structures of characteristic dimensions between 1 and 100 nm. Nanostructured materials have proven as one of the most powerful tool in new trend of technology and research due to their absolutely peculiar properties at nanometer size scale. Clearly, the synthesis of new nanomaterials and the control of their composition, size, shape and morphology are essential cornerstones for the application of nanomaterials in a new generation of submicron scale electronic, optical and sensing devices.

With the "top-down" methods (lithography and etching processes), solid-state physics and electronics have advanced towards the field of nanostructures. These "top-down" approaches permit the synthesis of pre-set addressable structures with a high degree of structure control but, as a result of the strong UV absorption of the polymer masks, there is a natural limit at about 100 nm for lithographic methods which does not allow the structural elements to be down-sized deep into the submicrometer range. One of the great challenges facing physics, chemistry, and materials science today is to find a way to structure

molecules so as to enable them to build functional nanostructures by self-organization (“bottom-up” approach). In chemistry the term “self-organization” is used when well-defined structures result spontaneously from the components of a system by non-covalent forces (self-assembly), for example, in liquid crystals, micelles, oscillating reactions.

Block copolymers (BCPs) are macromolecules, consisting of two or more chemically distinct polymer fragments (blocks) covalently bonded together, which, as a result of self-organization, can build up a wide variety of nanostructures with a typical length scale in the range 10-100 nm. BCPs have attracted much attention because of their great versatility. By tuning molecular parameters (molecular weight, composition, species, concentration), indeed, nanometric domains with a variety of motifs, chemistries, tailored size and periodicity may be created. So the spontaneous self-assembly of these materials can be used to prepare a large number of tailor-made nanostructured materials, that can be used as nanoscopic device components or templates.

For all these reasons, BCPs microphase separation has been the focus of intense research activity, both fundamental and applied, spanning the last 30 years. These efforts have produced a solid foundation of theoretical and experimental understanding of the rich behaviour of these systems and provided insight into how this spontaneous nanoscopic pattern formation might be harnessed for use in a variety of technological schemes.

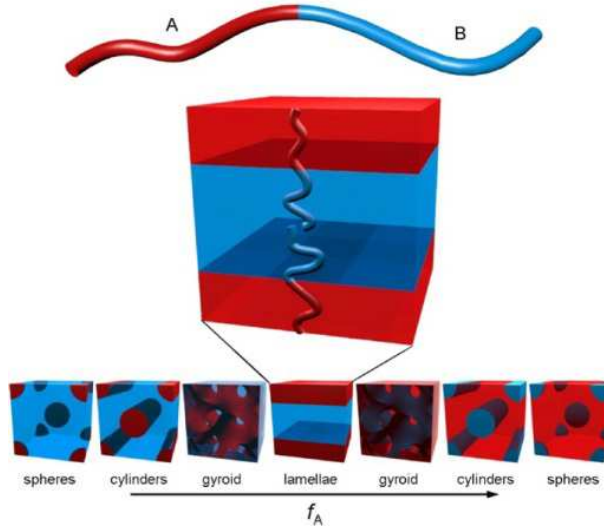
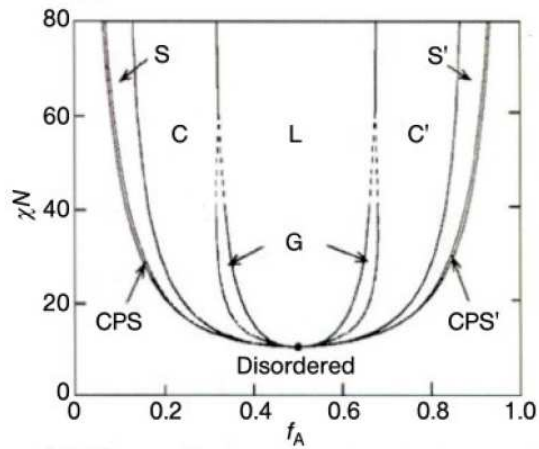
By exploiting the self-assembly properties of these macromolecules, new frontiers in miniaturization and integration at the nanoscale level, that overcome several of the intrinsic limitations of current top-down fabrication technologies, may be reached.

The assembly of nanostructures on common substrates (glass, silicon, etc.) is the first step for the creation of innovative Lab-On-Chip devices, that is a combination and integration of fluidic elements, sensor components and detection elements to perform the complete sequence of a chemical reaction or analysis, including sample preparation, reactions, separation and detection [1].

The aim of this introductory chapter is to give a brief overview of the different nanostructures that can be obtained by di-block copolymers self-assembly (paragraph 1.2) and of the most used methods to order them (paragraph 1.3). Some specific BCPs applications will be described in paragraph 1.4. The attention will be mainly focused on BCPs thin films. In particular, attention will be devoted to BCPs based nanocomposites (paragraph 1.4.1) and nanoporous materials (paragraph 1.4.2). In the paragraph 1.4.3, another BCPs application will be briefly described, that is the use of BCPs as additive in resins. Finally, in the last paragraph (1.5), the aim and the organization of present thesis work will be illustrated.

## **1.2 Block Copolymers: general principles and morphologies**

Block copolymers (BCPs) are macromolecules composed of two or more chemically distinct polymer blocks covalently bound together. This thesis will focus only on the simplest and most studied category: the A-B diblock copolymer composed of a linear polymeric chain of type A bound on one end to a linear polymeric chain of type B (Fig. 1.1A). The structure of BCP materials leads to a variety of useful properties; indeed, industrial applications for BCPs in thermoplastic elastomers, foams, adhesives, etc. have been around for decades. More recently, renewed attention has been directed at these materials for applications in nanotechnology because of their capability to form by self-assembly structures with periodicity at nanometric scale [2-5]. This is due to the thermodynamic incompatibility between the A and B blocks that drives a collection of A-B diblock molecules to self-organize via microphase separation in order to minimize the contact between dissimilar blocks (Fig. 1.1A). Phase separation is induced on a scale that is directly related to the size of the copolymer chains, which results in morphologies typified by a pattern of chemically distinct domains of periodicity in the 10-100 nm range [2, 6].

**A****B**

**Fig. 1.1** **A)** The chains of the A-B diblock copolymer, depicted as a simple two-color chain for simplicity, self-organize such that contact between the immiscible blocks is minimized. The list of morphologies formed by diblock copolymers in the bulk is reported. The final morphology (spheres, cylinders, gyroid or lamellae) is determined primarily by the relative lengths of the two polymer blocks ( $f_A$  is the volume fraction of block A). Reproduced from ref. 6 *b*. **B)** Theoretical phase diagram for linear AB diblock copolymers. Four equilibrium morphologies are predicted: spherical (S), cylindrical (C), gyroid (G), and lamellar (L), depending on the composition  $f_A$  and combination parameter  $\chi N$ .  $\chi$  is the Flory-Huggins interaction parameter and  $N$  is the degree of polymerization. The schematic representation of the equilibrium microdomain structures as  $f_A$  is increased for fixed  $\chi N$  values is reported in A. Reproduced from [7].

The common periodic morphologies for A-B diblock copolymers are depicted in Fig. 1.1A with the diblock molecules represented as simplified two-color chains. The final morphology mainly depends on the relative block length, parameterized as the volume fraction of one of the constituent blocks ( $f_A$ ). The possible morphologies are bodycentered cubic A spheres in a B matrix (spheres, S), hexagonally packed A cylinders in a B matrix (cylinders, C), bicontinuous gyroid (gyroid, G), and lamellae (L). The four theoretical equilibrium morphologies, calculated by “self-consistent mean field” treatments, can be mapped out on a phase diagram, as shown in Figure 1.1 B [7]. The phase diagram plots the product  $\chi N$  on the ordinate versus the volume ratio,  $f_A$ , on the independent axis.  $\chi$  is known as the Flory-Huggins interaction parameter, which quantifies the relative incompatibility between the polymer blocks, and is inversely related to the temperature of the system.  $N$  is the degree of polymerization, which is the total number of monomers per macromolecule. The volume fraction is represented by  $f_A = N_A/N$ , where  $N_A$  is the number of A monomers per molecule. For very low concentrations of A monomer, no phase separation will occur and the two polymers will mix homogeneously. However, at slightly higher compositions, where  $f_A \ll f_B$ , the A blocks form spherical microdomains in a matrix of B (S). Increasing the volume fraction to  $f_A < f_B$  leads to an increase in the connectivity of the microdomains, triggering the spheres to coalesce into cylinders that arrange on a hexagonal lattice (C). A roughly equal amount of both A and B blocks ( $f_A \approx f_B$ ) will result in the formation of alternating layered sheets, or lamellae, of the A and B blocks (L). Any further increase in  $f_A$  ( $f_A > f_B$ ), will cause the phases to invert, which means that the B block forms the microdomains in the matrix of A.

Except for some specific instances, the majority of block copolymers nanostructures applications proposed to date rely on the use of BCPs thin film (thickness in the nanometric range). In thin films, in addition to composition and molecular weight, the domain structure is also dependent on the surface energies of the blocks and on geometrical constraints introduced by confinement in a thin film [8]. Block copolymer thin films are usually prepared by the spin-coating technique, where drops of a solution of the copolymer in a volatile organic solvent are deposited on a spinning solid substrate. The polymer film spreads by centrifugal forces, and the volatile solvent is rapidly driven off. With care, the method can give films with a low surface roughness over areas of square millimetres. The film thickness can be controlled through the spin speed, the concentration of the block copolymer solution or the volatility of the solvent, which also influences the surface roughness [9]. In figure 1.2 two literature examples of BCPs thin films with different morphologies are reported [10, 11].

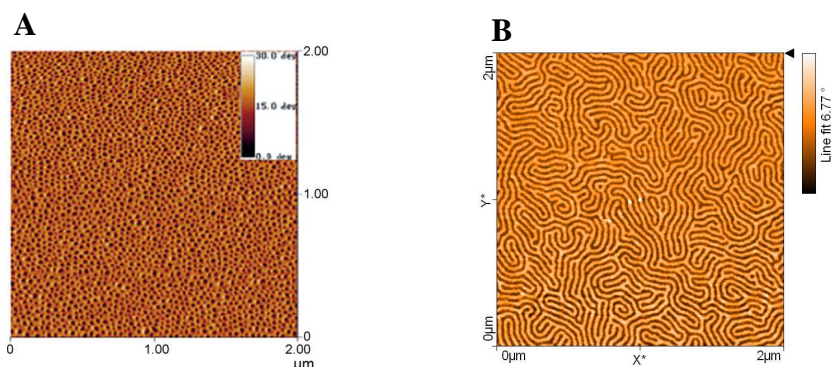


**Fig. 1.2** AFM phase contrast images of a PS-*b*-PEO cylinder forming thin film (PEO cylinder) (**A**) and of a PS-*b*-PMMA lamellar forming thin film (**B**). Two distinct phases can be identified on the samples surfaces corresponding to the two phase separated blocks of the copolymer. Reproduced from ref. 10 and 11.

In particular, in Fig. 1.2A an atomic force microscopy (AFM) images of a 255 nm thick, spin-coated polystyrene-*block*-poly(ethylene oxide)

(PS-*b*-PEO) film is reported [10]. An array of nanoscopic cylindrical domains is seen at the surface of the film, where the minor component, PEO, forms the cylindrical domains (darker in the image) and PS, the major component, constitutes the matrix (lighter in the image). The cylindrical PEO domains are oriented normal to the surface of the film and span the entire film thickness. This ordering of the copolymer is induced by controlling the rate of solvent evaporation during the spin coating process (this method will be discussed later in the paragraph 1.3.1). In figure 1.2 B an example of a lamellar forming polystyrene-*block*-poly(methyl methacrylate) (PS-*b*-PMMA) copolymer is reported [11]. The film thickness, prepared by spin coating from a BCP toluene solution, is about 20 nm. Defect-free disordered lamellar arrangement is observed. Two distinct phases can be identified on the sample surface corresponding to the phase separated PMMA and PS blocks of the copolymer.

From this brief overview it is clear that block copolymers represent an extremely versatile class of materials for generating interesting nanoscopic structures. Modern synthetic chemistry provides virtually limitless possibilities for BCP structure and function. The ability to design a polymer molecule with a specific length scale and geometry affords an opportunity to prepare idealized nanostructures for a wide variety of applications. However, for some specific applications, it is essential that both the orientation and lateral ordering of the BCP nanoscopic domains be controlled to fully realize the potential of these materials. This aspect will be discussed in the next paragraph.

### **1.3 Orientation of block copolymer morphologies on long-range scale**

The development of BCPs thin films into practical routes suitable for industrial applications will only be fully exploited when the nontrivial problem of large area ordering and precise orientation of BCPs domains will be solved. The spatial and orientational control of BCP nanodomains is necessary for a few of the possible applications of BCPs, such as in the creation of addressable, high-density information storage media, writing and replication processes in microelectronics and BCPs use as templates to obtain ordered array of nanoparticles. The long-range alignment of nanostructures in block copolymer films can be obtained using different strategies, that can be classified into three different approaches [12]:

*1. Control of orientation by applying external fields*, such as electric [13], magnetic, thermal [14], mechanical [15] and solvent evaporation [16].

*2. Modulation of substrate and surface interactions* as a result of: preferential interaction of one block with the surface, neutralization of attractions to the substrate or to the surface [17], epitaxial crystallization of domains onto a crystalline substrate, directional eutectic crystallization of a BC solvent, graphoepitaxy and 2-D geometric confinements.

*3. Induction of large-area ordering by facilitating the self-assembly, generally of thin films, using templates either topographically or chemically nanopatterned* [18].

Here, we will describe in more detail only the two techniques used in the present thesis work that is the control of solvent evaporation

(belonging to the first strategy) and the directional eutectic crystallization (belonging to the second strategy).

### 1.3.1 Solvent evaporation

The observation of lamellar and cylindrical microdomains in thin films perpendicular to the surface as a result of solvent evaporation was first reported by Turturro and coworkers [16 *a*] and then investigated in more detail by Kim and Libera for a similar triblock copolymer [16 *b, c*]. They demonstrated that a perpendicular orientation of cylinders can be obtained for sufficiently high solvent evaporation rates, as previously showed in Figure 1.2A. A necessary condition to produce perpendicular cylinders through solvent evaporation is that a good solvent for both blocks be used, and that one block only is below its glass transition temperature at room temperature. It was noted that as the solvent evaporates, a concentration gradient front propagates through the film and the system passes through a disorder-order transition. The structure formed can be trapped if one block goes through its glass transition. A schematic representation of the proposed mechanism is reported in Figure 1.3.

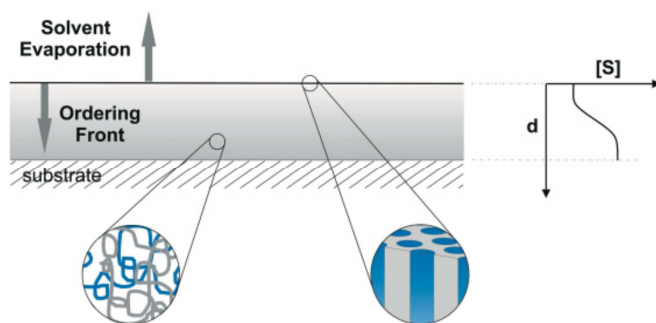


**Fig. 1.3** Schematic of the solvent evaporation in a diblock copolymer thin film [10]. The diffusion produces a gradient in the concentration of the solvent,  $[S]$ , as a function of depth,  $d$ , which induces an ordering front from the film surface to the substrate.

At the beginning of film deposition the glass transition temperature ( $T_g$ ) of the swollen film is still well below room temperature, thus allowing free chain mobility. With the decrease in the solvent concentration, the BCP undergoes a transition from the disordered to the ordered state and, as the diffusion of the solvent produces a gradient of concentration along the thickness of the thin film, the ordering front rapidly propagates from the air surface to the substrate. The consequent decrease of  $T_g$  below room temperature, for at least one block, locks in the structures, which, due to the high directionality of the solvent gradient, are highly oriented normal to the surface. This behavior has been reported so far for films with thickness less than one-half micron, as for instance in the case of polystyrene-*block*-polybutadiene (PS-*b*-PB) systems [10, 16 a], polystyrene-*block*-poly(ethylene oxide) (PS-*b*-PEO) [19] and polystyrene-*b*-poly(ferrocenyl dimethylsilane) (PS-*b*-PFS) [20]. However this mechanism holds to any BCPs having the  $T_g$  of one block above room temperature. If both blocks are glassy, as in polystyrene-*block*-poly(methyl methacrylate) (PS-*b*-PMMA) diblocks, this effect is not observed.

### **1.3.2 Directional eutectic solidification and epitaxy**

The methods of directional eutectic solidification and epitaxy to create large-sized, well-oriented cylindrical and lamellar microdomains of block copolymers in thin films was proposed by De Rosa and co-workers [21]. The method of directional eutectic solidification is based on the use of crystalline organic materials, which are solvents for the block copolymers above their melting temperatures, and, when cooled and directionally crystallized, act as a substrate on which thin films of the

block copolymers are formed. The aspects of the directional eutectic solidification can be realized by dividing the process into three stages using a hypothetical solvent-polymer phase diagram. The phase diagram of a system formed by an high molecular mass ( $M_n$ ) polystyrene-*block*-poly(L-lactide) (PS-*b*-PLLA) copolymer and an appropriate solvent is reported in figure 1.4A [22]. An important feature of the phase diagram is the presence of an eutectic due to the intersection of the melting-point depression liquidus curve of the crystallizable solvent with the order-disorder temperature depression liquidus (that is the microphase separation) curve of block copolymer. The corresponding morphological evolution, following the stages 1, 2, 3 e 4 of Figure 1.4A, is indicated in Figure 1.4B.

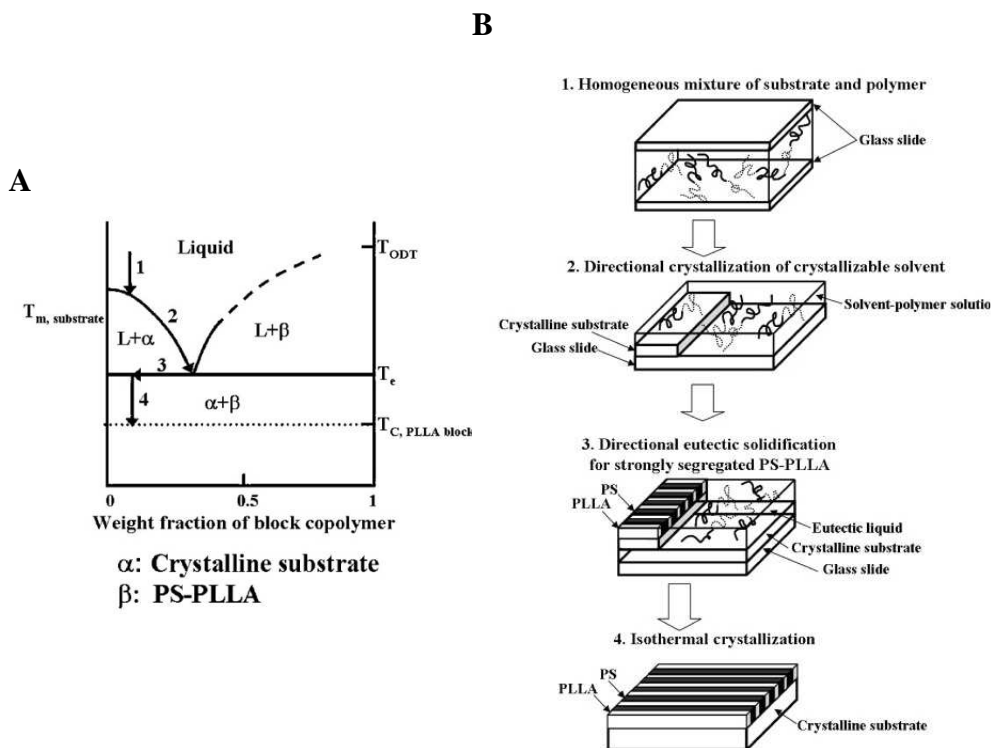


**Fig. 1.4** A) Phase diagram of crystallizable solvent-polymer systems for strongly segregated high  $M_n$  PS-*b*-PLLA. B) Illustration of morphological evolution for the oriented microstructures in PS-*b*-PLLA.

At high temperature, the solvent-polymer solution system is a homogeneous liquid (stage 1). When decreasing the temperature below the melting-point depression liquidus curve, solvent starts to crystallize and forms an oriented crystalline substrate while the polymer concentration in the remaining solution increases (stage 2). When temperature reaches the eutectic temperature, the solution with eutectic composition begins to directionally solidify on the preexisting crystalline substrate and large-scale lamellar PS-*b*-PLLA microstructures are formed (stage 3). After directional eutectic solidification, well-oriented lamellar microstructures with an alternation of flat-on single layers of crystalline PLLA lamellae and of amorphous layers of PS is formed (stage 4). In this scenario, the formation of large-sized, oriented PS-*b*-PLLA microstructures results mainly from directional eutectic solidification. It has to be noted, however, that, when a semicrystalline block copolymer is used, also the existence of epitaxial relationship between crystalline block and crystallizable solvent has to be considered. Epitaxy is defined as the oriented growth of a crystal on the surface of a crystal of another substance (the substrate). The growth of the crystals occurs in one or more strictly defined crystallographic orientations defined by the crystal lattice of the crystalline substrate [23]. The resulting mutual orientation is due to a 2D or, less frequently, a 1D-structural analogy, with the lattice matching in the plane of contact of the two species [23 *a*]. The term epitaxy, literally meaning “on surface arrangement”, was introduced in the early theory of organized crystal growth based on structural matching. Inorganic substrates were first used for the epitaxial crystallization of polymers [24]. Successive studies demonstrated the epitaxial crystallizations of polyethylene (PE) and linear polyesters onto crystals of organic substrates, such as condensed aromatic hydrocarbons

(naphthalene, anthracene, phenanthrene, etc.), linear polyphenyls and aromatic carboxylic acids [25].

When block copolymers containing a crystallizable block are used and there is an epitaxial relationship between crystalline block and crystallizable solvent, the lattice matching can improve the orientation order of the microdomains. In this case, the process involves two driving forces, i.e., (1) directional solidification and (2) epitaxy that together produce oriented microdomains via crystallization of the crystalline block onto the surface of the performed crystals of the organic solvent. The combination of the two types of interactions determined the kinetically driven microstructures [21 *a, b*].

Orientation of block copolymer microdomains via directional crystallization of a solvent and epitaxy is an effective way to develop unidirectional long-range ordering of block copolymers. The orientation of microdomains occurs within a few seconds without any long time annealing procedures. Depending on the nature of semicrystalline block copolymers and on the properties of organic crystallizable solvents (melting temperature, crystalline structure, the fast growth direction of the crystals), and on the epitaxial relationship between crystalline block and crystallizable solvent, versatile patterned textures can be achieved.

## 1.4 Applications of block copolymers

Until recently, most industrial applications of BCPs were as adhesives or related to their mechanical properties (e.g. as thermoplastic elastomers). Only in the past 20 years researchers have taken BCPs into the “high-technology” area, to the so-called “nanotechnologies”. An idea of the wide range of BCPs applications in the nanotechnologies field is given in figure 1.5. Self assembled BCP microstructures with 10 to 100 nm dimensions are useful as nanometer scale porous membranes, templates for fabrication of nano-objects such as metal, ceramic nanodots and wires, as 1-, 2- and 3D photonic crystals, and as nanopattern masks for fabrication of high density information storage media. One focus of great interest has been in the patterning of microelectronics components on a length scale inaccessible by optical lithography.

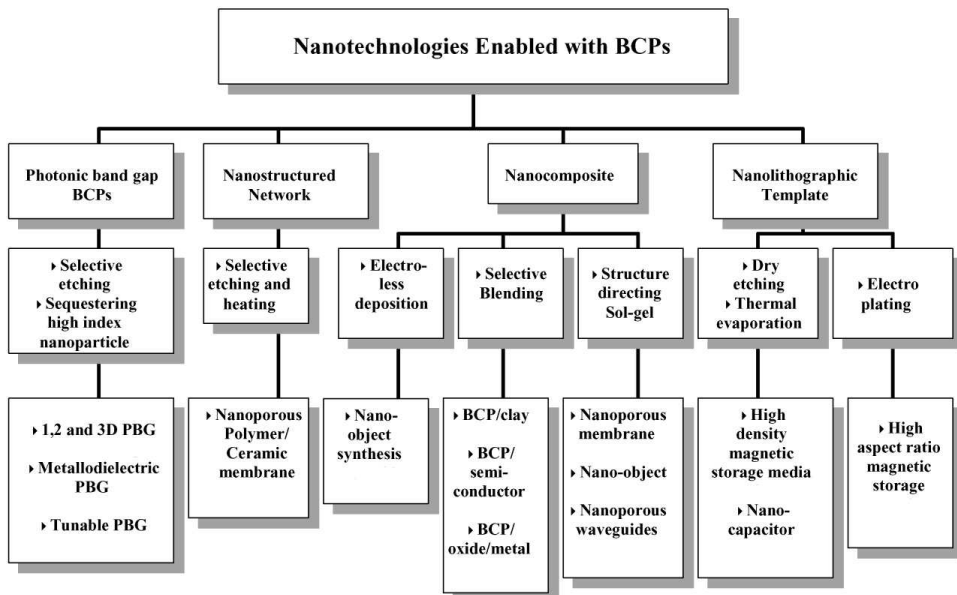


**Fig. 1.5** Schematic representation of nanotechnologies enabled with BCPs. Reproduced from ref. 26.

In particular, block copolymer thin films are of particular interest because of the possibility of obtaining two-dimensional patterns with very high registry and regularity. So, although block copolymers have also made extensive inroads to bulk applications ranging from drug delivery to structural materials, this section will focus mainly on applications of thin films. In particular, two specific nanotechnological applications enabled with BCPs thin films will be outlined: the use of BCPs as tool to obtain composites with nanoparticles at surfaces and the fabrication of nanoporous materials, through the selective removal of one block from self-assembled BCPs. Additionally, in paragraph 1.4.3, the use of block copolymers as additive in photopolymerizable resins will be discussed.

#### **1.4.1 Block copolymers based nanocomposites**

Nanocomposites represent a class of materials constituted by a polymeric matrix and nanoparticles (NPs). Particles in the nanometer size range (NPs) are attracting increasing attention with the growth of interest in nanotechnological disciplines because they display unique electronic, optical and catalytic properties, very different from bulk materials, originating from their quantum-scale dimensions [27]. In order to tailor new generations of nanodevices and smart materials, ways to organize the nanoparticles into controlled architectures must be found. So the construction of nanoparticles ordered arrays on surfaces has gained significant attention in the last years and the diversity of building blocks, architectures, and construction techniques that have been reported is impressive [27]. To fabricate an ordered array of nanoparticles, it is necessary to deposit them in perfect two-dimensional order on the solid substrate from the solution of nanoparticles. However, a perfect array of

nanoparticles is rarely achieved, particularly over an extended area, because of uncontrolled formation of defects in the self-assembling process of the nanoparticles induced by the solvent evaporation [28]. To fully exploit the nanoparticles' functionality, more effective ways to organize nanometer-sized particles on the micron and submicron scale has to be found. Effective fabrication of a two-dimensional array of nanoparticles on solid substrates has been demonstrated by the utilization of block copolymers (BCPs) in a self-assembled arrangement [29]. Nanodomains of self-assembled BCPs may act as *hosts* for sequestering nanofillers producing nanocomposites with different morphologies [29] (Fig 1.6). The size and shape of the NPs containing nanodomains may be conveniently tuned by changing the molecular weights and compositions of the BCPs [30].

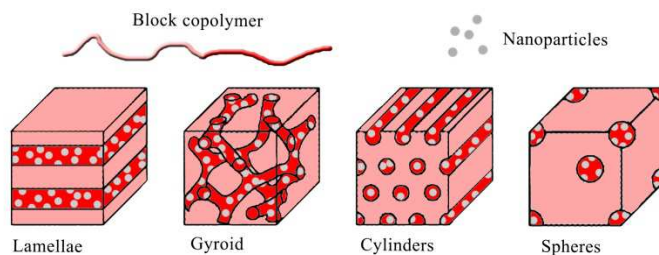


**Fig. 1.6** Nanodomains generated from BCPs (lamellae, gyroid, cylinders or spheres) may act as hosts for sequestering guest nanoparticles (NPs), to obtain nanocomposites where the distribution of the NPs is guided by the ordering of the BCP matrix.

Usually, two synthetic approaches are used for the preparation of nanocomposites based on BCP matrix: a) *ex-situ* synthesis of nanoparticles that are surface-tailored in order to allow preferential sequestering within a target domain of the BCP matrix; b) *in-situ* synthesis of inorganic particles within a BCP domain that is preloaded with a suitable precursor, generally a salt of a metal. In the second approach, used in the present thesis work, block copolymer nanodomains are used as “nanoreactors” for the in situ synthesis of inorganic

nanoparticles. Cohen and coworkers systematically examined the preparation of diblock copolymer nanoreactors, which are subsequently loaded with a salt that is then reduced to form metal nanodomains. They demonstrated the patterning of complexes of silver [31], gold [32] and zinc [33] using polynorbornene-based block copolymers. An example of the obtained BCP/Ag NPs composite is reported in Fig. 1.7. The nanoparticles, formed after the reduction of the metal salt, result selectively included in the norbornene-based block of a lamellar forming block copolymer.

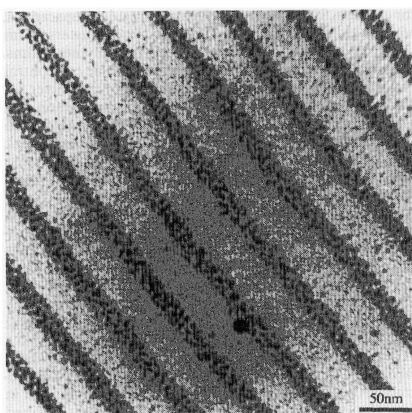


**Fig 1.7** TEM image showing patterning of silver clusters within a BCP lamellar microdomain structure. The two polymeric blocks forming the lamellar copolymer are a polynorbornene-derivative polymer and a methyltetraacyclododecene (MTD). The silver is dispersed within the polynorbornene-derivative lamellae; the other domains (MTD) appears bright in the TEM image. Reproduced from ref. 31 *c*.

The employment of nanostructures from block copolymers is one of the most promising ways to locate nanoparticles in a controlled way on solid substrates. The key for the engineering of these materials is the ability to control the final morphology of BCP nanostructures and to achieve a selective infiltration of nanoparticles in the target nanodomains. Advantages arising from the possibility of inducing long range order in the block copolymers nanostructures and, correspondingly, in the positioning of nanoparticles, consist in the fact that the nanoparticles will not randomly distribute in the polymeric matrix but sequestered in the ordered microdomains and consequently in an ordered manner all over

the matrix and they will not form aggregates. The possible outlooks linked to the development of such materials depend strictly on the kind of new proprieties that could emerge from the presence of long-range order of the nanoparticles, taking advantage of both the physical properties of the polymeric matrix and the nano specific characteristics of the included component.

#### **1.4.2 Block copolymers based nanoporous materials**

Porosity represents an important structural feature of many inorganic and organic materials. It may be used to vary important material properties such as electrical and thermal conductivity, refractive index, density, mechanical strength, and toughness. Additionally, porosity may be used for any kind of transport process as well as for molecular recognition. Both inorganic and organic porous materials, for example in the form of membranes [34], find broad application in many areas of separation science such as membrane filtration for the clean up of biologically relevant compounds and fluids (haemodialysis), for the gas separation and as ionselective membranes [35]. Membranes for these applications usually consist of either isolated polymer networks or porous polymer films [36].

Diblock copolymers (BCPs) represent a class of materials that exhibit a great versatility in the creation of nanoporous materials [37]. They can self-assemble, as previously discussed, to form different structures in which nanodomains of one polymeric block alternate to nanodomains of the other block. By using block copolymers in which one polymeric component can be selectively removed (etched), a large variety of nanoporous organic materials can be obtained (Fig. 1.8). The pores

morphology and dimensions of the resultant nanoporous materials can be precisely tailored by varying the morphology and the molecular weight of the initial block copolymer.

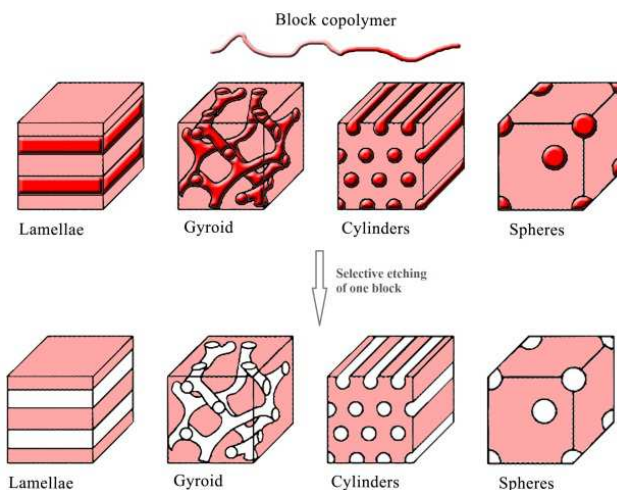


**Fig. 1.8** Nanoporous materials can be generated by selective removal of one component (etching) from a self-assembled block copolymer. The resulting porous material will exhibit the pore size and pore topology of their parent structures.

There are two key requirements for preparing nanoporous materials from ordered block copolymers: (i) the etchable polymeric block must be physically accessible to the solvent, reagent, process utilized for degradation; and (ii) the matrix material must be able to support the resultant nanoporous structure. There are many possible degradation techniques/etchable blocks (Table 1.1) and a variety of matrix materials that meet these necessities. As synthetic techniques keep expanding the range of available block copolymer structures, this list will expand, and new applications will parallel this growth.

**Table 1.1** Most used etchable polymeric blocks and degradation techniques to prepare nanoporous materials from block copolymers.

Etchable block	Degradation techniques	References
Poly(methyl methacrylate)	Photolysis Etch selectivity	38
Poly(butadiene)	Ozonolysis	39
Poly(isobutylene)	Reactive ion etching Ozonolysis	40
Poly( $\alpha$ -methylstyrene)	Heat / Vacuum	41
Poly(L-lactide)	Treatment in basic aqueous solutions	42
Poly(4-vinylpyridina)	Reactive ion etching	43
Poly(styrene)	Reactive ion etching	44
Poly(perfluoro octyl ethyl methacrylate)	Reactive ion etching	45

Given the range of block copolymer structures available, nanoporous materials with a wide range of tunable properties can be imagined. Two significant literature examples of BCP based nanoporous materials are reported in figures 1.9 and 1.10.

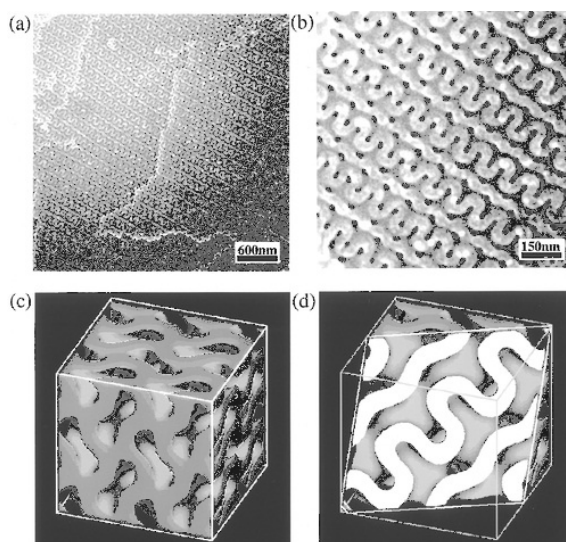


**Fig. 1.9** Nanoporous membrane from an etched BCP gyroid structure. SEM micrographs showing a bicontinuous nanochannel in the matrix of PS with two different magnifications (parts a and b) and computer graphics of the double gyroid network: (c) a three-dimensional view and (d) a two-dimensional intersection cut along the [211] direction. Reproduced from ref. 46.

Hashimoto *et al.* [46] employed a blend constituted by a poly(styrene-*b*-isoprene) (PS-*b*-PI) copolymer and an homopolymer (polystyrene). The role of the homopolymer was of tuning the volume fraction of polystyrene, thus obtaining the desired microstructure, that is the gyroid phase (Fig. 1.9). After the achievement of the desired nanostructure, the domains of polyisoprene were removed by ozonolysis to reach a structure formed from nanochannels (Fig. 1.9). The complete removal of the PI phase resulted in the formation of a three-dimensionally porous continuous material. The symmetry of the precursor material was nearly identical to the resultant porous material.

Another literature example [47], attesting that the control of the feature pores size is possible by varying BCP molecular weight, is reported in figure 1.10.

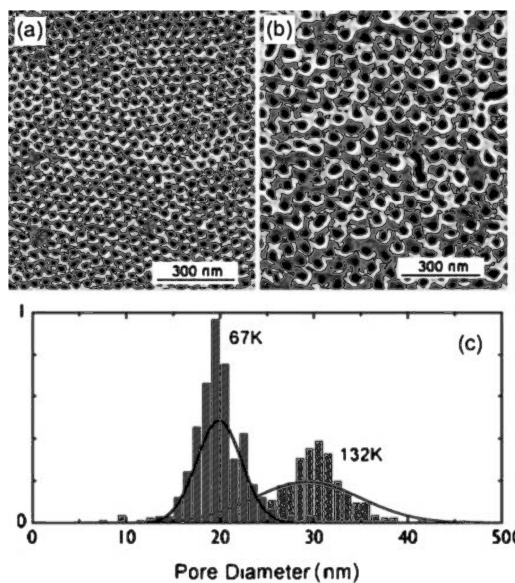


**Fig. 1.10** SEM image of nanoporous PS materials resulting after the selective removal of PMMA phase from a  $67 \text{ kg mol}^{-1}$  (a) and  $132 \text{ kg mol}^{-1}$  (b) PS-*b*-PMMA thin film. (c) pore diameter histograms. Reproduced from ref. 47.

The selective etching of a cylinder-forming phase in an ordered block copolymer, polystyrene-*block*-poly(methyl methacrylate) (PS-*b*-PMMA),

resulted in the formation of nanoscopic channels provided the matrix material can support such a structure. In particular, the authors examined the effect of block copolymer molecular weight on the porous structure resulting from degradation of the cylindrical PMMA domains. Using a block copolymer of higher molecular weight (from  $67 \text{ kg mol}^{-1}$  to  $132 \text{ kg mol}^{-1}$ ), they reported a variation in the pores dimension of about 10 nm (Fig. 1.10 c).

Given the numerous successful demonstrations of the block copolymer strategy in the design and synthesis of nanoporous materials, BCPs holds a great deal of promise for the “bottom-up” engineering of nanostructured materials in a wide range of applications. While nanolithographic applications predominate the application examples, the developments in chemistry, block copolymer processing, and degradation techniques may lead to a significant increase in the breadth of applications in membrane separations, nanotemplating, high-surface-area catalysis and in photonic research area [37]. An emerging application area of BCP based porous materials is their use as support to immobilize specific biomolecules for sensing applications. BCP based nanoporous materials, in fact, exhibit large surface areas, suitable pore sizes, and controllable wettability, ideal for biomolecular adsorption. This aspect will be discussed later in Chapter 3.

### **1.4.3 Block copolymers as additive to create nanostructured resins**

The curing process, that is the polymerization of liquid monomers or oligomers to produce solid densely crosslinked networks (resins), finds wide applications in different fields. Epoxy resins, for example, are used

as structural adhesives, in surface coatings, electrical potting and insulation, as matrix in fibers reinforced composites, amongst other applications [48]. Densely crosslinked networks resulting from polymerization of dimethacrylates find applications in dentistry such as dental composites, pit and fissure sealants, dentine bonding agents and cements [49], dental adhesives [50] and elastomeric impression materials [51].

Block copolymers modified resins have generated significant interest since it was demonstrated that the combination can lead, through self-assembly, to nanostructured systems with improved mechanical properties and advantageous thermal characteristics. The cured resins, in fact, tend to be rather brittle due to their high cross-link density and are therefore prone to fracture. Different studies have established that the incorporation of a second phase can improve both stiffness and toughness in polymer composites [52]. The inclusion of a second phase offers also the opportunity to modify the thermal characteristics of epoxy resins such as increasing thermal conductivity or reducing the coefficient of thermal expansion [48].

Two major classes can be derived from the broad range of additives used for resin modification, rigid inorganic particles and soft organic particles. We will focus our attention on the second class of additives, in particular on block copolymers, as the modifiers to produce nanostructured inclusions in thermoset resins. In particular, the majority of literature work is concerned with the characterization of nanostructured blends of epoxy resins and block copolymers [53].

The formation of nanostructured systems in cured blends of epoxy resin and diblock copolymer was first reported by Hillmyer *et al.* in 1997 [54]. They demonstrated the formation of hexagonally packed cylinders

with diameters on the order of tens of nanometres. The epoxy system was bisphenol-A diglycidyl ether (BADGE) + phthalic anhydride (PA) and the block copolymer was poly(ethylene oxide)-*b*-poly(ethyl ethylene) (PEO-*b*-PEE). Cylinders with a core-shell morphology consisting of a non-polar core surrounded by a corona of PEO were observed as shown in Fig. 1.11 A.

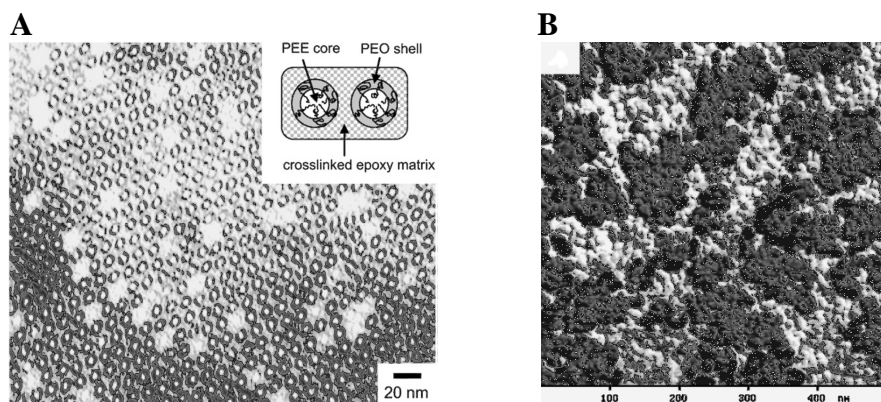


**Fig. 1.11** **A)** TEM image showing cylinders of PEO-*b*-PEE in an epoxy matrix. The core-shell morphology is clearly visible. Reproduced from [54]. **B)** AFM phase image of 20 wt% PEO-PPO-PEO (80% PEO) cured in epoxy resin. The lighter areas are harder (epoxy-rich) and the dark areas (copolymer-rich) were softer. Reproduced from [55].

Since that initial report, a number of research groups have carried out further investigations into a range of epoxy/block copolymer blend systems [53]. The results suggest significant potential for block copolymers in epoxy resins, both as toughening agents for epoxy resins and as templating agents for nanostructured materials. Depending on the matrices, curing agents and block copolymers, both *microphase* and *macrophase* separation can occur in resins/block copolymers blend systems. *Microphase separation* leads to nanostructured systems with dimensions determined by the size of the individual blocks. The phase boundaries will coincide (approximately) with the inter-block interfaces

in the block copolymer. In *macrophase separation*, separation occurs at larger length scales by nucleation and growth or spinodal decomposition.

The block copolymers reviewed can be divided into three categories. The first type are those that self-assemble in the uncured epoxy via a resinophilic part (epoxy-miscible block) and a resinophobic part (epoxy-immiscible block). The nanoscale structures are formed in the pre-cure stage and fixed during cure. The second class is formed by the diblocks where both blocks are miscible but one of them undergoes reaction induced microphase separation. In both these cases, the block copolymer is non-reactive in the resin. The case where the epoxy-miscible block is reactive towards the resin or the curing agent conforms to the third type. A literature example of the second class of systems, a reaction induced microphase separation, is reported in figure 1.11 B [55]. Blends of poly(ethylene oxide)-*block*-poly(propylene oxide)-*block*-poly(ethylene oxide) (PEO-PPO-PEO) triblock (80 wt% PEO) in methylene dianiline (MDA) cured Bisphenol-A diglycidyl ether (BADGE) were examined. At 20 wt% block copolymer the system shows hierarchical nanostructure; spherical micelles of diameter ~10 nm are dispersed throughout the resin phase which is composed of harder, epoxy-rich, and softer, copolymer-rich, regions on the 100 nm scale (figure 1.11 B).

Generally speaking, cross-linked products are formed by chemical reactions that can be initiated by heat (thermal curing, as in the case of the epoxy resins previously discussed), pressure, change in pH, or radiation. The latter case includes electron beam exposure (EB curing), gamma-radiation and UV light (UV curing). The radiation curing process shows different advantages compared to thermal curing methods. The primary advantage is the speed of which the final product can be obtained. In UV curing, for example, high intensity ultraviolet light is used to create a

photochemical reaction that instantly cures inks, adhesives and coatings. UV Curing is adaptable to printing, coating, decorating, stereolithography and assembling of a variety of products and materials. Originally introduced in the 1960s this technology has streamlined and increased automation in many industries in the manufacturing sector (medical, automotive, cosmetic, food, scientific, educational and art) [56]. In particular, *stereolithography* is one of the most interesting application of UV curing. It is an additive manufacturing process which employs a vat of liquid ultraviolet curable photopolymer (resin) and an ultraviolet laser to build, layer by layer, a complete solid 3-D part. This process is used in modern 3D printer and it will be described in paragraph 4.1.

The dominant chemistry for UV curing is the radical polymerization of unsaturated monomers and oligomers. Monomers and oligomers containing acrylate unsaturation are the most commonly utilized in UV initiated radical polymerization due to their higher reactivity. One of the most used (especially in current commercial dental composites) is the Bisphenol A bis(2-hydroxy-3-methacryloxypropyl)ether (Bis-GMA) (Fig. 1.12) [57]. It is an ester of an aromatic dimethacrylate, a long and rigid molecule with reactive carbon-to-carbon double bonds at both ends. Its high molecular weight, relatively high viscosity, and the presence of aromatic groups contribute to the rigidity of the molecular chain. Advantages of using Bis-GMA include less shrinkage and higher modulus. These desirable properties of Bis-GMA are partially negated by a relatively high viscosity. For this reason, it is common practice to decrease the high viscosity of Bis-GMA by dilution with a monomer of lower molecular, normally triethylene glycol dimethacrylate (TEGDMA), which is a relatively flexible linear molecule with carbon unsaturated bonds at both ends (Figure 1.12).

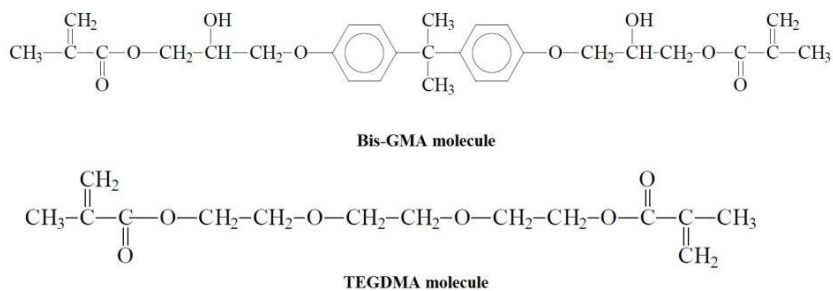


**Fig. 1.12** Structure of Bisphenol A bis(2-hydroxy-3-methacryloxypropyl)ether (Bis-GMA) and Triethyleneglycol dimethacrylate (TEGDMA).

Usually, an appropriate photoinitiator is added to the UV-curable systems. It absorb the UV light and undergoes a photoreaction that produces the reactive energetic radical species that are capable of initiating the polymerization of the unsaturated constituents in the formulation. Photoinitiator chemistry is fundamental for efficient polymerization to achieve satisfactory mechanical and physical properties of the final cross-linked copolymer [58].

To our knowledge, there are no literature works concerning the addition of block copolymers in UV photopolymerizable dimethacrylate systems to build nanostructured resins that could eventually improve the final properties of these materials.

## 1.5 Description of the thesis work

The aim of the present project is the study of new nanomaterials, based on block copolymers (BCPs), able to selectively recognize and/or detect chemical species, with the purpose to design, characterize and fabricate functional nanostructures to be used as active elements in selective sensing and/or biosensing devices with high sensitivity.

The research has been mainly focused on the creation of two classes of BCP based materials: nanocomposite materials characterized by selective inclusion of functional nanoparticles in specific domains, with potential advantageous properties useful in advanced sensing, and nanoporous materials with functionalized nanochannels able to immobilize biomolecules. The BCPs unparalleled versatility in the creations of these classes of nanostructured materials have been widely discussed in paragraph 1.4.1 and 1.4.2.

The fabrication of the first class of BCP based materials (nanocomposites) will be described in **Chapter II**. BCPs have been used as *hosts* for the selective inclusion of functional inorganic nanoparticles (NPs) in specific nanodomains according to well defined geometries ordered over large area, to build nanostructured hybrid nanocomposites on solid surfaces. In particular, two different methods have been used to design nanocomposites based on polystyrene-*block*-poly(ethylene oxide) copolymers (PS-*b*-PEO) matrix and Pd nanoparticles. We report a simple method to fabricate ordered arrays of palladium (Pd) nanoclusters and palladium oxide (PdO) nanoparticles with tunable dimensions and lateral spacing by using cylinder forming PS-*b*-PEO copolymers as both stabilizers for Pd nanoparticles and templates controlling the distribution

of them. We were able to modulate the dimensions of Pd nanoclusters and PdO NPs and their inter-distance by using as template two different PS-PEO copolymers having different molecular mass of both PS and PEO block.

The **Chapter III** is devoted to the design, fabrication and characterization of a nanoporous BCP based materials able to act as ideal support for the physical immobilization of specific biomolecules. In particular, we have designed a nanoporous thin film with well defined architecture containing functionalized pores delimited by hydrophilic walls, exploiting self-assembly of lamellar block copolymers and the concept of sacrificial block. We have employed a blend of polystyrene-*block*-poly(L-lactide) (PS-*b*-PLLA) and polystyrene-*block*-poly(ethylene oxide) (PS-*b*-PEO) diblock copolymers to generate thin films with a single-phase lamellar morphology in which the PEO and PLLA blocks form lamellae within a PS matrix. Then, by selective chemical etching of the PLLA block, the nanoporous thin film, patterned with nanometric channels containing pendant hydrophilic PEO chains, has been generated. We have studied the physical adsorption onto our BCP based porous surface of two hemoproteins, myoglobin (Mb) and peroxidase from horseradish (HRP), and of the enzyme esterase 2 from *Alicyclobacillus acidocaldarius*, able to act as active element in biosensors for the detection of specific organophosphate pesticides.

In **Chapter IV** an explorative study regarding dimethacrylate based photopolymeric systems modified with small amounts of a polystyrene-*block*-poly(ethylene oxide) copolymer (PS-*b*-PEO) is reported. The studied system is a mixture of Bisphenol A bis(2-hydroxy-3-methacryloxypropyl)ether (Bis-GMA) and Triethyleneglycol

dimethacrylate (TEGDMA), activated for UV light photopolymerization by the addition of the photoinitiator Phenylbis(2,4,6-trimethylbenzoyl)phosphine oxide (Irgacure819). The studied materials can be used in modern 3D printers.

## BIBLIOGRAPHY CHAPTER I

- [1] C. M. Niemeyer, C. A. Mirkin, *Nanobiotechnology: Concepts, Applications and Perspectives*, Part I, Chapter 2, Wiley-VCH. G. A. Urban, *Meas. Sci. Technol.* **2009**, 20, 012001.
- [2] F. S. Bates, G. H. Fredrickson, *Annu. Rev. Phys. Chem.* **1990**, 41, 525.
- [3] L. Leibler, *Macromolecules* **1980**, 13, 1602.
- [4] B. D. Olsen, X. Li, J. Wang, R. A. Segalman, *Macromolecules* **2007**, 40, 3287.
- [5] W. van Zoelen, G. ten Brinke, *Soft Matter* **2009**, 5, 1568.
- [6] a) E. L. Thomas, R. L. Lescanec, *Philos. Trans. R. Soc. London Ser. A* **1994**, 348, 149. b) S. B. Darling, *Prog. Polym. Sci.* **2007**, 32, 1152.
- [7] F. S. Bates, G.H. Fredrickson, *Phys. Today* **1999**, 52, 32.
- [8] M. J. Fasolka, A. M. Mayes, *Annu. Rev. Mater. Res.* **2001**, 31, 323.
- [9] K. E. Strawhecker, S. K. Kumar, J. F. Douglas, A. Karim, *Macromolecules* **2001**, 34, 4669.
- [10] S. H. Kim, M. J. Misner, T. Xu, M. Kimura, T. P. Russell, *Adv. Mater.* **2004**, 16, 226.
- [11] V. Kapaklis, S. Grammatikopoulos, R. Sordan, A. Miranda, F. Traversi, Hans von Känel, D. Trachylis, P. Pouloupoulos, C. Politis, *J. Nanosc. & nanotech.* **2010**, 10, 6056.
- [12] M. Lazzari, C. De Rosa, *Advanced nanomaterials* **2009**, Chapter 4, K. E. Geckeler and H. Nishide eds, Wiley-VCH.
- [13] a) T. Thurn Albrecht, J. De Rouchey, T. P. Russell, R. Kolb, *Macromolecules* **2002**, 35, 8106. b) T. Thurn Albrecht, R. Steiner, J. De Rouchey, C. M. Stafford, E. Huang, M. Bal, M. T. Tuominen, C. J. Hawker, T. P. Russell, *Adv. Mater.* **2000**, 12, 787.

- [14] J. Hahn, S. J. Sibener, *J. Chem. Phys.* **2001**, 114, 4730.
- [15] a) C. Daniel, I. W. Hamley, W. Mingvanish, C. Booth, *Macromolecules* **2000**, 33, 2163. b) I. W. Hamley, *Curr. Opin. Colloid Interface Sci.* **2000**, 5, 342.
- [16] a) A. Turturro, E. Gattiglia, P. Vacca, G. T. Viola, *Polymer* **1995**, 21, 3987. b) G. Kim, M. Libera, *Macromolecules* **1998**, 31, 2569. c) G. Kim, M. Libera, *Macromolecules* **1998**, 31, 2670.
- [17] a) E. Huang, S. Pruzinsky, T. P. Russell, J. Mays, C. J. Hawker C.J., *Macromolecules* **1999**, 32, 5299. b) E. Huang, T. P. Russell, C. Harrison, P. M. Chaikin, R. A. Register, C. J. Hawker, J. Mays, *Macromolecules* **1998**, 31, 7641.
- [18] a) R. D. Peters, X. M. Yang, Q. Wang, J. J. De Pablo, P. F. Nealey, *J. Vac. Sci. Tech. B* **2000**, 18, 3530. b) S. O. Kim, H. H. Solak, M. P. Stoykovich, N. J. Ferrier, J. J. De Pablo, P. F. Nealey, *Nature* **2003**, 424, 411.
- [19] a) M. Kimura, M. J. Mister, T. Xu, S. H. Kim, T. P. Russell, *Langmuir* **2003**, 19, 9910. b) Z. Lin, D. H. Kim, X. Wu, L. Boosahda, D. Stone, L. LaRose, T. P. Russell, *Adv. Mater.* **2002**, 14, 1373.
- [20] K. Temple, K. Kulbaba, K. N. Power-Billard, I. Manners, K. A. Leach, T. Xu, T. P. Russell, C. J. Hawcker, *Adv. Mater.* **2003**, 15, 297.
- [21] a) C. De Rosa, C. Park, E. L. Thomas, B. Lotz, *Nature* **2000**, 405, 433. b) C. De Rosa, C. Park, B. Lotz, J. C. Wittmann, L. J. Fetters, E. L. Thomas. *Macromolecules* **2000**, 33, 4871. c) C. Park, C. De Rosa, E. L. Thomas, *Macromolecules* **2001**, 34, 2602.
- [22] W. H. Tseng, P. Y. Hsieh, R. M. Ho, B. H. Huang, C.-C. Lin, B. Lotz. *Macromolecules* **2006**, 39, 7071.
- [23] a) L. Royer, *Bull. Soc. Fr. Mineral. Crystallogr.* **1928**, 51, 7. b) J. H. Van der Mere, *Discuss. Faraday Soc.* **1949**, 5, 206. c) G. S. Swei, J. B. Lando, S. E. Rickert, K. A. Mauritz, *Encyclopedia Polym. Sci. Eng.* **1986**, 6, 209.

- [24] a) J. Willems, *Naturwissenschaften* **1955**, 42, 176. b) A. J. Lovinger, *J. Polym. Sci. Polym. Phys. Ed.* **1983**, 21, 97.
- [25] a) J. C. Wittmann, B. Lotz, *Prog. Polym. Sci.* **1990**, 15, 909. b) S. Kopp, J. C. Wittmann, B. Lotz, *Makromol. Chem. Macromol. Symp.* **1995**, 98, 917.
- [26] C. Park, J. Yoon, E. L. Thomas, *Polymer* **2003**, 44, 6725.
- [27] A. N. Shipway, E. Katz, I. Willner, *Chemphyschem* **2000**, 1, 18.
- [28] a) V. Santhanam, R. P. Andres, *Nano Lett.* **2004**, 4, 41. b) E. Rabani, D. R. Reichman, P. L. Geissler, L. E. Brus, *Nature* **2003**, 426, 271.
- [29] M. R. Bockstaller, R. A. Mickiewicz, E. L. Thomas, *Adv. Mater.* **2005**, 17, 1331.
- [30] a) K. Hatada, T. Kitayama, O. Vogl, *Macromolecular Design of Polymeric Materials* **1997**, Marcel Dekker eds, New York. b) N. Hadjichristidis, M. Pitzikalis, S. Pispas, H. Iatrou, *Chem. Rev.* **2001**, 101, 3747.
- [31] a) Y. N. C. Chan, R. R. Schrock, R. E. Cohen, *Chem. Mater.* **1992**, 4, 24. b) Y. N. C. Chan, R. R. Schrock, R. E. Cohen, *J. Am. Chem. Soc.* **1992**, 114, 7295. c) B. H. Sohn, R. E. Cohen, *Acta Polym.* **1996**, 47, 340.
- [32] Y. N. C. Chan, R. R. Schrock, R. E. Cohen, *Chem. Mater.* **1992**, 4, 24.
- [33] J. Yue, V. Sankaran, R. E. Cohen, R. R. Schrock, *J. Am. Chem. Soc.* **1993**, 115, 4409.
- [34] A. Tavolaro, E. Drioli, *Adv. Mater.* **1999**, 11, 975.
- [35] a) M. J. Dunleavy, *Med. Device Technol.* **1996**, 5, 14. b) H. Odani, T. Masuda, *Design of Polymer Membranes for Gas Separation* **1992**, VCH, New York. c) G. Maier, *Angew. Chem.* **1998**, 110, 3128. d) J. D. R. Thomas, *Analyst* **1994**, 119, 203.
- [36] W. J. Koros, G. K. Fleming, S. M. Jordan, T. H. Kim, H. H. Hoehn, *Prog. Polym. Sci.* **1988**, 13, 339.

- [37] M. A. Hillmyer, *Adv. Polym. Sci.* **2005**, 190, 137.
- [38] a) E. Drockenmuller, L.Y.T. Li., D. Y. Ryu, E. Harth, T. P. Russell, H. C. Kim, C. J. Hawker, *J. Polym. Sci., Part A: Polym. Chem.* **2005**, 43, 1028. b) K. Shin, K. A. Leach, J. T. Goldbach, D. H. Kim, J. Y. Jho, M. Tuominen, C. J. Hawker, T. P. Russell, *Nano Lett.* **2002**, 2, 933. c) K. Naito, H. Hieda, M. Sakurai, Y. Kamata, K. Asakawa, *IEEE Trans. Magn.* **2002**, 38, 1949.
- [39] a) M. Park, C. Harrison, P. M. Chaikin, R. A. Register, D. H. Adamson, *Science* **1997**, 276, 1401. b) P. Mansky, C. K. Harrison, P. M. Chaikin, R. A. Register, N. Yao, *Appl. Phys. Lett.* **1996**, 68, 2586.
- [40] R. G. H. Lammertink, M. A. Hempenius, J. E. Van Den Enk, V. Z. H. Chan, E. L. Thomas, G. J. Vancso, *Adv. Mater.* **2000**, 12, 98. V. Z. H. Chan, J. Hoffman, V. J. Lee, H. Latrou, A. Avgeropoulos, N. Hadjichristidis, R. D. Miller, *Science* **1999**, 286, 1716.
- [41] P. Du, M. Li, K. Douki, X. Li, C. B. W. Garcia, A. Jain, D. M. Smilgies, L. J. Fetters, S. M. Gruner, U. Wiesner, C. K. Ober, *Adv. Mater.* **2004**, 16, 953.
- [42] a) A. S. Zalusky, R. Olayo - Valles, C. J. Taylor, M. A. Hillmyer, *J. Am. Chem. Soc.* **2001**, 123, 1519. b) J. Rzaev, M. A. Hillmyer, *Macromolecules* **2005**, 38, 3.
- [43] Z. Lin, D. H. Kim, X. Wu, L. Boosahda, D. Stone, L. LaRose, T. P. Russell, *Adv. Mater.* **2002**, 14, 1373.
- [44] J. Y. Cheng, C. A. Ross, E. L. Thomas, H. I. Smith, G. J. Vancso, *Appl. Phys. Lett.* **2002**, 81, 3657.
- [45] H. Yokoyama, L. Li, T. Nemoto, K. Sugiyama, *Adv. Mater.* **2004**, 16, 1542.
- [46] T. Hashimoto, K. Tsutsumi, Y. Funaki, *Langmuir* **1997**, 13, 6869.
- [47] K. W. Guarini, C. T. Black, S. H. I. Yeung, *Adv. Mater.* **2002**, 14, 1290.

- [48] B. Ellis, *Chemistry and technology of epoxy resins* **1993**, Blackie Academic & Professional.
- [49] a) R. G. Craig, ed. *Restorative dental materials* **1997**, 10th ed. St. Louis, Missouri, C.V. Mosby Company. b) L. A. Linden, *Radiation curing in polymer science and technology* **1993**, J. P. Fouassier and J. E. Rabek eds., vol. IV, Essex: Elsevier Ltd.
- [50] N. Silikas, D. C. Watts. *Dent. Mater.* **1999**, 15, 257.
- [51] W. D. Cook. *J. Appl. Polym. Sci.* **1991**, 42, 2209.
- [52] a) B. B. Johnsen, A. J. Kinloch, R. D. Mohammed, A. C. Taylor, S. Sprenger, *Polymer* **2007**, 48, 530. b) J. Jordan, K. I. Jacob, R. Tannenbaum, M. A. Sharaf, I. Jasiuk, *Mater. Sci. Eng. A* **2005**, 393, 1.
- [53] L. Ruiz-Pérez, G. J. Royston, J. P. A. Fairclough, A. J. Ryan, *Polymer* **2008**, 49, 4475.
- [54] M. A. Hillmyer, P. M. Lipic, D. A. Hajduk, K. Almdal, F. S. Bates. *J. Am. Chem. Soc.* **1997**, 119, 2749.
- [55] Q. Guo, R. Thomann, W. Gronski, T. Thurn-Albrecht, *Macromolecules* **2002**, 35, 3133.
- [56] S. P. Pappas, *UV Curing: Science and Technology* **1985**, Volume 2 Hardcover.
- [57] a) I. Sideridou, V. Tserki, G. Papanastasiou, *Biomaterials* **2002**, 23, 1819. b) P. Ekworapoj, R. Magaraphan, D. C. Martin, *Journal of Metals, Materials and Minerals* **2002**, 12, 39. c) K. L. Van Landuyta, J. Snauwaertb, J. De Muncka, M. Peumansa, Y. Yoshidac, A. Poitevina, E. Coutinhoa, K. Suzukic, P. Lambrechtsa, B. Van Meerbeeka, *Biomaterials* **2007**, 28, 3757.
- [58] a) J. W. Stansbury, *J. Esthetic. Dent.* **2000**, 12, 300. b) M. G. Neumann, W. G. Miranda, C. C. Schmitt, F. A. Rueggeberg, I. C. Correa, *J. Dent.* **2005**, 33, 525.

---

---

## CHAPTER II

---

---

### NANOCOMPOSITES BASED ON POLYSTYRENE-*block*- POLY(ETHYLENE OXIDE) COPOLYMERS (PS-*b*-PEO) AND PALLADIUM NANOPARTICLES

#### 2.1 Introduction to Chapter II

Palladium (Pd) and palladium oxide (PdO) nanoparticles (NPs) synthesis has gained considerable interest in the last few decades due to their numerous potential utilizations. Pd NPs show high activity and selectivity in numerous catalytic processes [1]. It is the metal of choice for the catalytic formation of C-C bonds, one of the most useful transformations in organic synthesis. PdO has been used as catalysts in catalytic combustion of natural gas (methane) or liquid-phase oxidation of alcohols with oxygen [2]. For these reasons, since the seventies, a huge variety of homogeneous catalytic systems based on Pd(II) or Pd(0) have been studied and have become a strategic tool for organic transformation and total synthesis. Because sustainable development involves the utilization of reusable catalysts, the search for new catalytic systems to replace existing homogeneous ones is one important issue. In this context, the immobilization of nanoparticles on a solid support is an interesting alternative since the catalyst can be recycled by simple filtration. Furthermore, immobilizing nanoparticles onto solid supports can minimize atom/ion leaching from the particles [1, 3]. Palladium has the potential to play a major role in virtually every aspect of the envisioned

hydrogen economy, including hydrogen purification, storage, detection, and fuel cells [4]. Also, palladium is used as a pre-coating material for electronless deposition of copper used for micro contacts and many electronic devices, such as resistors, use compositions containing palladium.

All these applications may be more suitable with nanoparticles in a patterned form and, since the majority of unique nanoparticles properties are highly microstructure-dependent, to form Pd and PdO arrays on solid supports with a precise control of nanoparticles dimensions and spacing is an important proposition.

As widely discussed in paragraph 1.4.1, the effective fabrication of two-dimensional arrays of nanoparticles on solid substrates is not simple and the utilization of block copolymers (BCPs) in a self-assembled arrangement represents a valid method to this aim [5]. In this Chapter, we report a simple method to fabricate ordered arrays of palladium (Pd) nanoclusters and palladium oxide (PdO) nanoparticles with tunable dimensions and lateral spacing by using polystyrene-*block*-poly(ethylene oxide) copolymers (PS-*b*-PEO) as both stabilizers for Pd nanoparticles and templates controlling the distribution of them. The volume fraction of PEO blocks in the copolymers has been selected in order to obtain a cylindrical microphase-separated morphology, in which the PEO blocks form a hexagonal array of cylinders in the PS matrix. Thin films characterized by a high degree of perpendicular orientation of PEO cylinders over large areas have been obtained. The cylindrical self-assembled nanostructure formed from PS-*b*-PEO block copolymers has been used as *host* for selectively sequestering a nanoparticles precursor (palladium(II) acetate) in PEO domains. Then, two different methods have been used to obtain Pd NPs from the precursor in presence of the

BCPs: electron irradiation of the thin films containing the BCPs and palladium precursor, and reduction in solution by thermal treatment before thin films preparation. In both cases, highly ordered nanocomposite thin films based on PS-*b*-PEO matrices and Pd nanoparticles have been obtained. Furthermore, PdO nanoparticles of improved stability against aggregation have been obtained on a solid and conductive support (silicon wafer) by treating the films in air at elevated temperatures. We were able to modulate the dimensions of Pd nanoclusters and PdO NPs and their inter-distance by using as template two different PS-*b*-PEO copolymers having different molecular weights of both PS and PEO blocks.

## 2.2 Materials and Methods

*Materials.* Two kinds of polystyrene-*block*-poly(ethylene oxide) copolymers (PS-*b*-PEO) with different molecular mass of both PS and PEO blocks have been purchased from Polymer Source, Inc. and used without further purification. The number-average molecular mass of the BCPs are 43.0 Kg mol<sup>-1</sup> ( $M_n^{\text{PS}} = 32.0 \text{ Kg mol}^{-1}$ ;  $M_n^{\text{PEO}} = 11.0 \text{ Kg mol}^{-1}$ , polydispersity 1.06) and 136.0 Kg mol<sup>-1</sup> ( $M_n^{\text{PS}} = 102.0 \text{ Kg mol}^{-1}$ ;  $M_n^{\text{PEO}} = 34.0 \text{ Kg mol}^{-1}$ , polydispersity 1.18). The first PS-*b*-PEO sample with lower molecular weight will be denoted as SEO; the second, with higher molecular weight, will be named HSEO. The characteristics of the samples are reported in table 2.1. Palladium(II) acetate (98 %) and toluene have been purchased from Sigma-Aldrich.

*Characterization of as received block copolymers.* Differential scanning calorimetry (DSC) experiments have been carried out using a calorimeter Mettler Toledo (DSC-822), calibrated with indium, in a

flowing N<sub>2</sub> atmosphere. A scanning rate of 10 °C/min has been used to record the first heating, cooling and second heating scans.

Small- and wide-angle X-ray scattering (SAXS and WAXS) experiments have been performed on station BM26B (DUBBLE) at the European synchrotron radiation facility (ESRF), Grenoble, France. A modified DSC Linkam hot stage has been employed that allows the transmission of X-rays through mica windows. The samples have been heated from -50 to 150 °C, then cooled from 150 to -50 °C and finally heated again to 150 °C. A total number of 240 frames have been acquired at a scanning rate of 5 °C/min. Time step/frame equal to 30 s, corresponding to change of 2.5 °C per step. A wavelength of 1.033 Å has been used to acquire the data. The sample holder scattering has been subtracted from each scan.

*Preparation of the nanomaterials.* Solutions of HSEO and SEO have been prepared dissolving the copolymers in toluene to yield a total concentration of 1.5% (w/w) with respect to the solvent. Pd(II) acetate has been added into BCP solutions to obtain a Pd acetate concentration of  $\approx$  26 or 53 wt% with respect to the BCP, corresponding to Pd : PEO monomeric units mole ratio equal to 0.20 and 0.40, respectively. The solutions have been stirred at room temperature for at least 3h. The Pd(II) reduction has been performed by heating the BCP/palladium acetate solutions in a water bath at 75 °C or 85 °C under vigorous, continuous stirring until the color of the solution becomes dark gray. Thin films of neat BCPs, BCPs/palladium precursor and BCPs/Pd NPs have been obtained by spin coating (RPM 4000 for 30 s) the corresponding toluene solutions. The oxidative treatments to remove the block copolymer matrix and produce the PdO NPs have been performed by heating the BCP/Pd NPs thin films in air at 600°C for 4 hours.

*Thin films characterization.* Transmission electron microscopy (TEM) images have been obtained in bright field mode using a Philips EM 208S TEM with an accelerating voltage of 100 kV. For TEM characterization, the thin films have been prepared by spin coating the solutions on carbon coated copper grids. Scanning electron microscopy (SEM) images have been collected using Zeiss Ultra Plus field emission SEM (Centro de Apoyo Científico-Tecnológico, Universidade de Santiago de Compostela), equipped with an Inlens detector and a SE Everhart - Thornley Secondary Electron Detector, using accelerating voltages of 1.0 or 1.5 kV. The samples for SEM observation have been prepared on silicon substrates. Grazing incident wide-angle X-ray scattering (GIWAXS) experiments have been performed at station BM26B (DUBBLE) of the European synchrotron radiation facility (ESRF), Grenoble, France. The samples for GIWAXS experiments have been prepared on rectangular (5 x 10 mm) silicon substrates. The employed wavelength and sample-detector distance have been 1.033 Å and 109.86 mm, respectively. The X-ray incident angle has been set to 0.15° and 0.12° in the case of the BCP nanocomposites containing Pd NPs and of the PdO nanoclusters sample, respectively. The thickness of films has been measured with an Alpha-Step IQ Surface Profiler (KLA TENCOR) by performing at least 5 independent measurements in different regions of the same sample and over different samples. The relative error is less than 10%.

*UV-Vis spectroscopy.* UV-Vis spectra of the solution containing the BCP and palladium precursor before and after different heating times have been recorded with a JASCO 550 UV-Vis spectrophotometer. The cell with 1.0 cm path length has been used to record UV-Vis spectra between 330 and 700 nm. The scan of toluene has been subtracted from

the scan of the sample. 2 mL of toluene have been added to 1 mL of the initial solution before recording the UV-Vis spectra.

*Suzuki cross-coupling reaction.* The Pd NPs/block copolymer thin film (prepared on glass substrates) has been placed into a glass container. A solution of potassium carbonate (414 mg) in water (2 mL) has been added to a solution of phenylboronic acid (133 mg) and 4-bromanisole (100  $\mu$ L) in absolute ethanol (2 mL). The so obtained mixture (total volume 4 mL) has been added to the glass container with the NPs/block copolymer thin film. The system has been heated to reflux by setting the hotplate temperature to 120 °C. After 1 h, the product has been extracted with dichloromethane (3 x 10 mL), dried with anhydrous sodium sulfate and concentrated under vacuum. The obtained solid product has been dissolved in chloroform and analyzed by  $^1\text{H}$  NMR using  $\text{CHCl}_3$  ( $\delta = 7.26$  ppm respect to TMS) as internal standard.

*Thermogravimetric analysis (TGA).* The TGA of the HSEO block copolymer has been performed using a TGA Q5000 IR Thermogravimetric Analyzer of TA Instruments, in a 100 ml  $\text{min}^{-1}$   $\text{N}_2$  flow atmosphere and 10 °C  $\text{min}^{-1}$  heating rate.

## 2.3 Results and discussion

### 2.3.1 Characterization of as received block copolymers (BCPs)

We have used two polystyrene-*block*-poly(ethylene oxide) copolymers (PS-*b*-PEO) block copolymers (BCPs) with different molecular mass of both PS and PEO blocks (Table 2.1). The number-average molecular mass of the BCPs are 43.0 Kg mol<sup>-1</sup> ( $M_n^{\text{PS}} = 32.0$  Kg mol<sup>-1</sup>;  $M_n^{\text{PEO}} = 11.0$  Kg mol<sup>-1</sup>, polydispersity 1.06) and 136.0 Kg mol<sup>-1</sup> ( $M_n^{\text{PS}} = 102.0$  Kg mol<sup>-1</sup>;  $M_n^{\text{PEO}} = 34.0$  Kg mol<sup>-1</sup>, polydispersity 1.18). We will denote the first sample with lower molecular weight as SEO and the other one, with higher molecular weight, as HSEO. Samples with volume fraction of PEO blocks around 20% have been purposely selected in order to obtain a cylindrical phase-separated morphology. The PS-*b*-PEO copolymers are semicrystalline, with PEO and PS being the crystalline and amorphous block, respectively.

**Table 2.1** Number average molecular mass ( $M_n$ ), polydispersity index of the molecular masses ( $PDI = M_w/M_n$ ), volume fraction of the PEO block ( $f_{PEO}$ ) of the two block copolymers polystyrene-*block*-poly(ethylene oxide) used in the present work. The melting ( $T_m^I$ ,  $T_m^{II}$ ) and crystallization ( $T_c$ ) temperatures of the PEO blocks are also indicated.

Sample	$M_n \times 10^3$ <sup>(a)</sup> (g/mol)	$M_w/M_n$ <sup>(a)</sup>	$f_{PEO}$ (%) <sup>(b)</sup>	$T_m^I$ (°C) <sup>(c)</sup>	$T_m^{II}$ (°C) <sup>(c)</sup>	$T_c$ (°C) <sup>(c)</sup>
PS- <i>b</i> -PEO (SEO)	32- <i>b</i> -11	1.06	23	57	51	-26
PS- <i>b</i> -PEO (HSEO)	102- <i>b</i> -34	1.18	23	61	65	-25

(a) Obtained by size exclusion chromatography (SEC) analysis.

(b) Calculated by considering that the density of PEO and PS are 1.064 g/cm<sup>3</sup> and 0.969 g/cm<sup>3</sup>, respectively [6].

(c) Determined by DSC analysis at scanning rate of 10 °C/min and N<sub>2</sub> (g) atmosphere.  $T_m^I$  and  $T_m^{II}$  are the melting temperatures measured in the first and second heating scans.

The as received block copolymers (table 2.1) have been characterized by differential scanning calorimetry (DSC) and X-ray scattering measurements, both at wide and small angle (WAXS and SAXS). SAXS is a powerful technique for examining nanostructures formed by the self-assembly of block copolymers, in the melt, solution and crystalline state. The main use of SAXS is to determine morphology. When semicrystalline block copolymers are studied, as in our case, wide-angle X-ray scattering (WAXS) is a common complementary technique to monitor crystallization at the unit cell level [7].

*Characterization of SEO block copolymer.* The differential scanning calorimetry (DSC) thermogram of the as received SEO block copolymer is shown in Fig. 2.1. The first heating, cooling and second heating scans, acquired using a scanning rate of 10 °C/min, are reported.

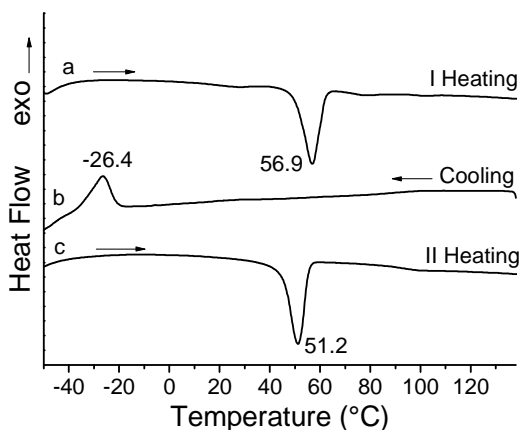


**Fig. 2.1** DSC thermogram of the as received SEO block copolymer recorded at 10 °C/min. The melting ( $T_m^I$ ,  $T_m^{II}$ ) temperatures, recorded during the first and second heating scans, and the crystallization ( $T_c$ ) temperature of PEO are indicated.

In the first heating scan of the DSC thermogram the endothermic peak, due to the melting of the crystalline PEO, is visible at 56.9 °C ( $T_m^I$ ). The exothermic peak, due to the crystallization of the same block, appears in the cooling scan at -26.4 °C ( $T_c$ ). It is worth noting that the crystallization temperature of PEO homopolymer is around 40 °C [8]. On the other hand,

it is known that in PS-*b*-PEO copolymers the crystallization temperature can be lower than that of the homopolymer [9]. Therefore our result is in agreement with literature data. Moreover similar behaviour was found also for a symmetric diblock copolymer, poly(ethylene oxide)-*block*-poly(1,4-butadiene) (PEO-*b*-PB) with PEO and PB being the crystalline and amorphous blocks, respectively, blended with various amount of a low molecular weight PB homopolymer [10]. Finally, the second PEO melting peak at a temperature of 51.2 °C ( $T_m^{II}$ ) is visible in the second heating DSC scan (Fig. 2.1). The PEO first melting, crystallization and second melting temperatures ( $T_m^I$ ,  $T_c$  and  $T_m^{II}$ ) obtained from the DSC analysis are reported in Table 2.1.

For wide and small angle X-ray scattering experiments (WAXS and SAXS), a total number of 240 frames have been acquired while the sample has been heated from -50 to 150 °C, then cooled from 150 to -50 °C and finally heated again to 150 °C, at a scanning rate of 5 °C/min. WAXS and SAXS profiles of the SEO sample at some selected temperatures acquired during the first heating scan are reported in Fig. 2.2.

The initial WAXS profile at 1.2 °C (curve a of Fig. 2.2 A) shows two distinct peaks centred at  $2\theta \approx 19$  and  $23^\circ$ , characteristic of crystalline polyethylene oxide (PEO) [11], superposed to an amorphous halo due to the contribution of amorphous phases of PEO and PS blocks. Increasing the temperature, the intensity of Bragg peaks decreases due to gradual melting of PEO crystals. The Bragg peaks completely disappear at  $\sim 57$  °C, indicating the complete PEO melting, in agreement with DSC data (curve a of Fig. 2.1).

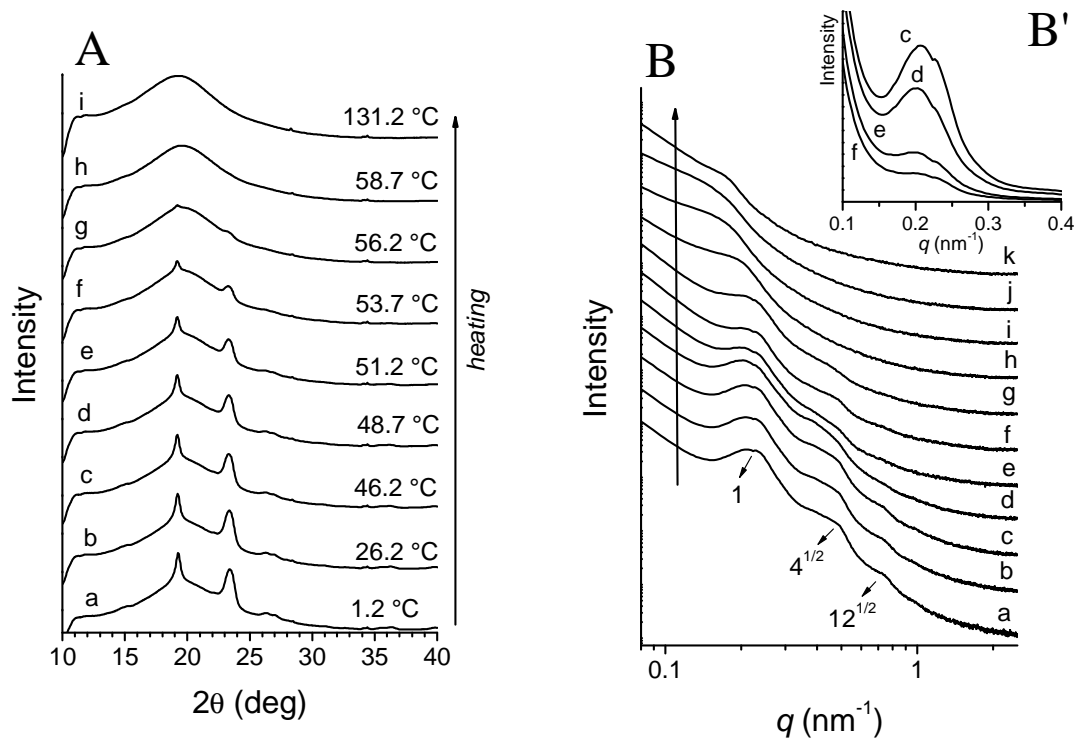


**Fig. 2.2** WAXS profiles (A) and SAXS data in logarithmic (B) and linear (B') scale of the as received SEO sample acquired during the first heating scan at the indicated temperatures in the case of WAXS profiles and at -48.7 (a), 1.2 (b), 26.2 (c), 51.2 (d), 56.2 (e), 78.7 (f), 98.7 (g), 118.7 (h), 131.2 (i), 138.7 (j) and 148.7 (k) °C in the case of SAXS profiles. The scanning rate was 5 °C/min. The arrows in B' indicate the peaks at  $q/q^* \sim 1$ ,  $4^{1/2}$ ,  $12^{1/2}$  typical of the pseudo-hexagonal morphology.

Small angle X-ray scattering (SAXS) profiles of the SEO sample acquired simultaneously to the WAXS data are reported in Fig. 2.2 B. As discussed in paragraph 1.2, for the simplest class of block copolymers, AB diblocks, the following morphologies are known to be stable: lamellar, hexagonal-packed cylinders, body-centred cubic spheres, and bicontinuous cubic gyroid structures [12]. SAXS is extensively used to identify morphologies in block copolymers from the sequence of Bragg reflections because there are a number of theoretical approaches that can be used to calculate structure factors and so to predict the observed SAXS peaks positions [7, 13]. Self-consistent mean-field theory (SCMFT), in particular, can provide structure factors for any block copolymer microstructure and good agreement with experiments was noted [14]. Table 2.2 lists the positions of peaks for the equilibrium structures observed in diblock copolymer melts [7]. Multiple orders of Bragg reflection are observed for strongly segregated samples. Weakly segregated samples may only exhibit the lower order peaks, which can lead to ambiguities in phase identification. This can be circumvented by supplementary information from a complementary technique, for example, transmission electron microscopy.

**Table 2.2** Peak positions (expressed as  $q/q^*$ ) of Bragg reflections for various equilibrium structures of BCPs; lamellar (Lam), hexagonal-packed cylinders (Hex), body-centred cubic spheres (BCC) and bicontinuous cubic gyroid (Gyr).

Structure	Ratio $q/q^*$
Lam	1, 2, 3, 4, 5, 6, ...
Hex	1, $3^{1/2}$ , $4^{1/2}$ , $7^{1/2}$ , $9^{1/2}$ , $12^{1/2}$ , ...
BCC	1, $2^{1/2}$ , $3^{1/2}$ , $4^{1/2}$ , $5^{1/2}$ , $6^{1/2}$ , ...
Gyr	1, $(4/3)^{1/2}$ , $(7/3)^{1/2}$ , $(8/3)^{1/2}$ , $(10/3)^{1/2}$ , $(11/3)^{1/2}$ , ...

In the SAXS profile recorded at 48.7 °C of our SEO sample (curve a of Fig. 2.2 B), the presence of Bragg reflections at  $q/q^* = 1, 4^{1/2}$  and  $12^{1/2}$

suggests a pseudo-hexagonal arrangements of PEO cylinders in the PS matrix, in agreement with predictions valid in the strong segregation limit for BCPs with PEO volume fraction of 20%. The exact peak positions and the corresponding domains spacings are reported in Table 2.3. Bragg peaks are visible also after the PEO melting at temperatures higher than 56 °C (curves f and g of Fig. 2.2 B) indicating a phase separated morphology also in the amorphous. At higher temperatures (curves h-k of Fig. 2.2 B) the peaks disappear indicating a disordered morphology, probably because the order-disorder transition temperature ( $T_{ODT}$ ) of the samples is reached. It is worth noting that the SAXS profiles recorded at temperature higher than 56 °C and lower than  $T_{ODT}$  (curves f, g of Fig. 2.2 B) show only the second order peak at  $q/q^* = 4^{1/2}$  of the main reflection at  $q^* \sim 0.22 \text{ nm}^{-1}$  probably due to the increase of packing disorder in the arrangements of PEO cylinders. The relative intensity of the Bragg peak at  $q^* \sim 0.20 \text{ nm}^{-1}$  decreases with increase of temperature especially upon melting of PEO crystals due to decrease of contrast (Fig. 2.2 B').

WAXS and SAXS profiles of the SEO sample at some selected temperatures acquired during cooling scan are reported in Fig. 2.3. From the WAXS profiles (Fig. 2.3 A) it is possible to determinate the PEO crystallization ( $T_c$ ) temperature, that results of around -35 °C. This temperature is  $\sim 9 \text{ °C}$  lower than the temperature determined from DSC experiments (Fig. 2.1). This discrepancy can be due to the different to the intrinsic different sensibility of the two techniques. In the SAXS profiles acquired during the cooling scan (Fig. 2.3 B) only one peak at  $q = 0.18 \text{ nm}^{-1}$  is observed, indicating that, after the melting, a not well defined morphology possibly pseudo hexagonal is obtained.

The WAXS and SAXS profiles acquired during the second heating scan are reported in Appendix (Fig. A2.1).

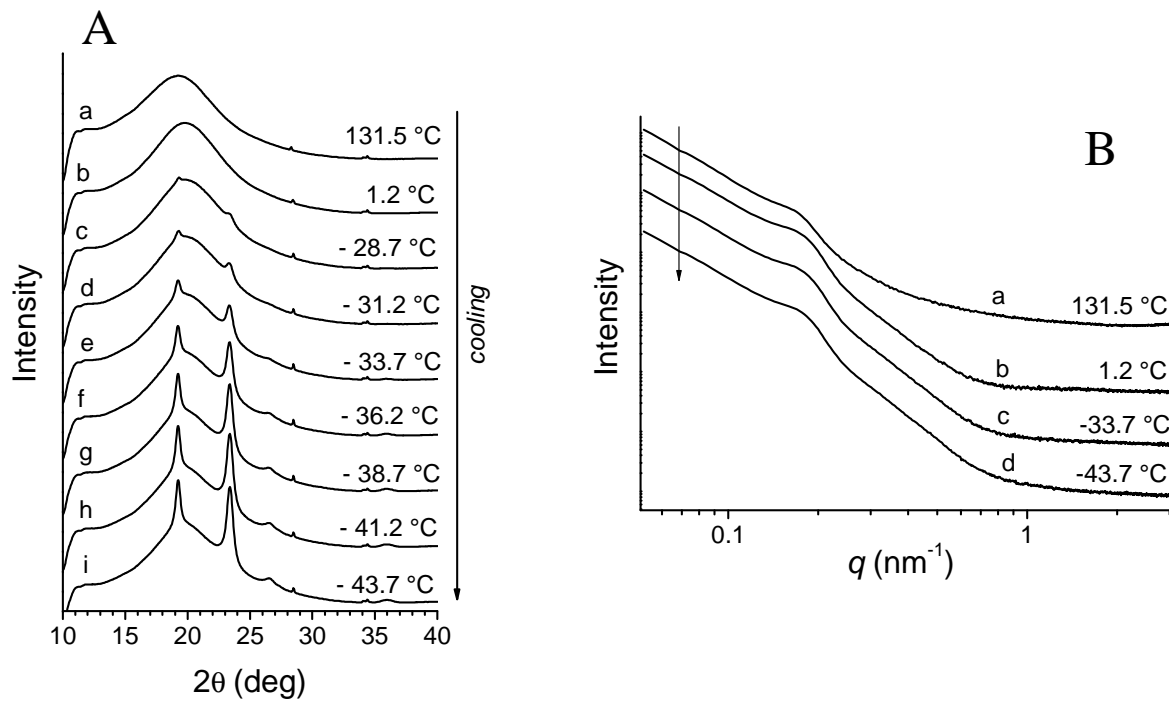


**Fig. 2.3** WAXS profiles (**A**) and SAXS data in logarithmic scale (**B**) of the as received SEO sample acquired during the cooling scan from the melt at the indicated temperatures. The scanning rate was 5 °C/min.

*Characterization of HSEO block copolymer.* The differential scanning calorimetry (DSC) thermogram of the as received HSEO block copolymer is shown in Fig. 2.4. The PEO melting temperatures ( $T_m^I$ ,  $T_m^{II}$ ) recorded during the first and second heating scans and the crystallization temperature ( $T_c$ ) are reported in Table 2.1. The values of  $T_m^I$  and  $T_c$  are similar to those of the PEO block in the two different BCPs, while a difference of  $\sim 15$  °C is observed for the PEO melting temperature in the second heating scan ( $T_m^{II}$ ).

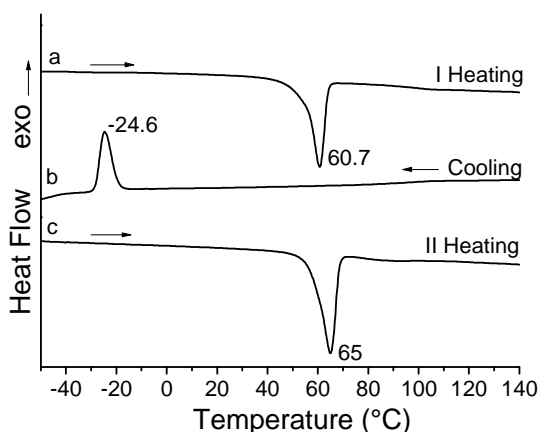


**Fig. 2.4** DSC thermogram of the as received HSEO block copolymer recorded at 10 °C/min. The melting ( $T_m^I$ ,  $T_m^{II}$ ) temperatures, recorded during the first and second heating scans, and the crystallization ( $T_c$ ) temperature of PEO are indicated.

WAXS and SAXS profiles of the HSEO sample at some selected temperatures during the first heating, cooling and second heating scans are reported in Fig. 2.5, 2.6 and A2.2, respectively. The peak positions and the corresponding domains spacings are reported in Table 2.3.

From the WAXS data acquired during the first heating scan (Fig. 2.5 A), the melting of PEO is observed at  $\sim 62$  °C was obtained, in agreement with the DSC results (Fig. 2.4 and Table 2.1).

In the SAXS profiles recorded at lower temperatures of our HSEO sample (curves a, b and c of Fig. 2.5 B), peaks at  $q/q^* = 1$  and  $7^{1/2}$  are present in agreement with the pseudo hexagonal packing of PEO cylinders in the PS matrix. The peaks of the hexagonal morphology are

visible also after the PEO melting at  $\sim 62$  °C (curves d-f of Fig. 2.5 B), indicating that this morphology is stable also for the fully amorphous BCP. It is worth to note that more defined SAXS peaks are observed at temperatures near to the glass transition temperature of PS blocks (curves h and i of Fig. 2.5 B), suggesting an improvement of the hexagonal morphology in the melt. Moreover also in this case the intensity of the main Bragg peak (Fig. 2.5 B') decreases when the temperature increases, due to decrease of contrast because of the PEO melting.

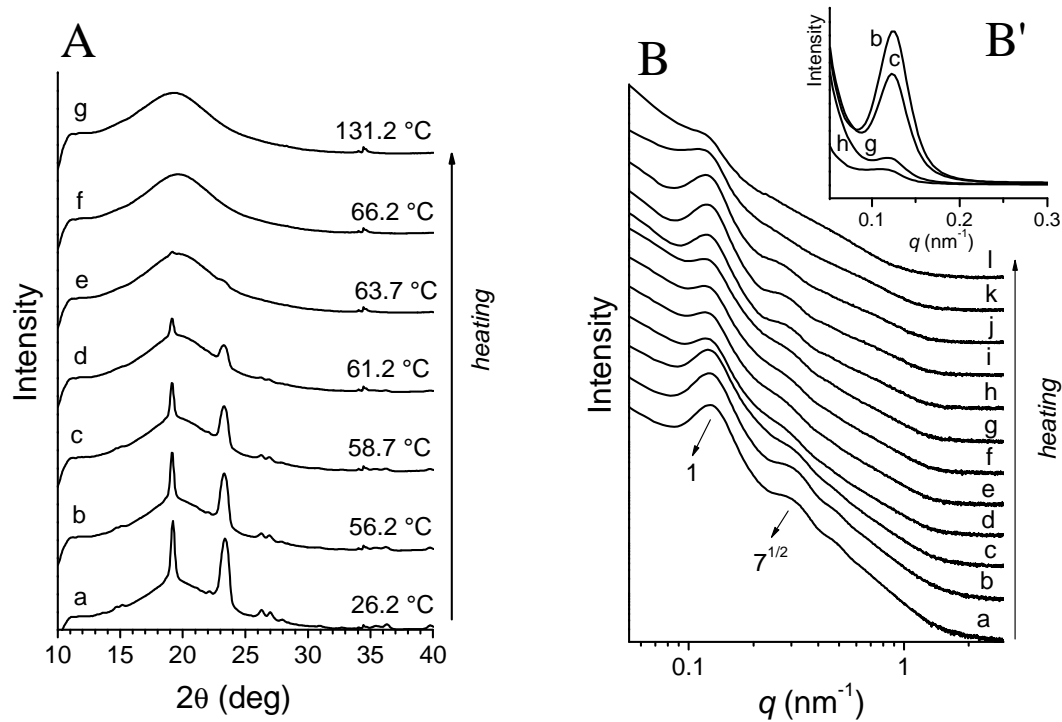


**Fig. 2.5** WAXS profiles (A) and SAXS data in logarithmic (B) and linear (B') scale of the as received HSEO sample acquired during the first heating scan at the indicated temperatures in the case of WAXS profiles and at -48.7 (a), 26.2 (b), 58.7 (c), 63.7 (d), 66.2 (e), 73.7 (f), 81.2 (g), 98.7 (h), 108.7 (i), 118.7 (j), 131.2 (k) and 148.7 (l) °C in the case of SAXS profiles. The scanning rate was 5 °C/min. The arrows in B' indicate the peaks at  $q/q^* \sim 1$  and  $7^{1/2}$  typical of the pseudo-hexagonal morphology.

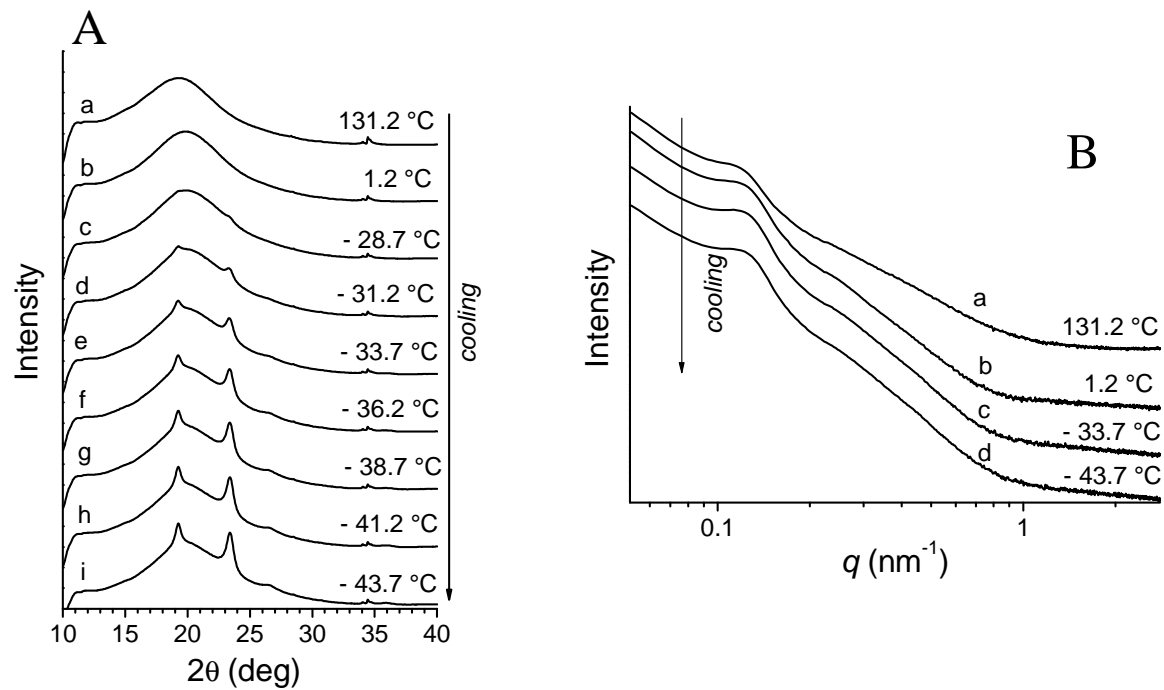


**Fig. 2.6** WAXS profiles (A) and SAXS data in logarithmic scale (B) of the as received HSEO sample acquired during the cooling scan from the melt at the indicated temperatures. The scanning rate was 5 °C/min

The SAXS profiles of the HSEO sample acquired during the cooling scan (Fig. 2.5 B) only show the first order reflection peak at  $0.12 \text{ nm}^{-1}$ , indicating, as in the case of the SEO sample (Fig. 2.3 B), that a not well defined morphology is reached for the sample directly cooled from the isotropic melt at a cooling rate of  $5 \text{ }^\circ\text{C}/\text{min}$ .

**Table 2.3** SAXS peak positions ( $q$ ) and  $d$ -spacings ( $d_1$ ) at the indicated temperatures ( $T$ ). The reported values are obtained from the SAXS profiles acquired during the first heating of the SEO (Fig. 2.2 B) and HSEO (Fig. 2.5 B) samples.

SEO <sup>(a)</sup>				
$T$ ( $^\circ\text{C}$ )	$q_1$ ( $\text{nm}^{-1}$ )	$q_2$ ( $\text{nm}^{-1}$ )	$q_3$ ( $\text{nm}^{-1}$ )	$d_1$ (nm) <sup>(c)</sup>
1.2	0.22	0.45	0.75	28
26.2	0.21	0.44	0.73	30
51.2	0.20	0.43	0.70	31
56.2	0.20	0.43	/	31
78.7	0.22	0.48	/	28
98.7	0.22	0.45	/	28
HSEO <sup>(b)</sup>				
$T$ ( $^\circ\text{C}$ )	$q_1$ ( $\text{nm}^{-1}$ )	$q_2$ ( $\text{nm}^{-1}$ )	$q_3$ ( $\text{nm}^{-1}$ )	$d_1$ (nm) <sup>(c)</sup>
26.2	0.12	0.32	/	52
58.7	0.12	0.30	/	52
66.2	0.12	0.30	/	52
81.2	0.12	0.31	/	52
98.7	0.12	0.30	/	52
108.7	0.12	0.29	/	52
118.7	0.12	0.27	/	52

(a)  $q_2 = 4^{1/2}q_1$  and  $q_3 = 12^{1/2}q_1$  (b)  $q_2 = 7^{1/2}q_1$

(c) Evaluated from the first order reflection peak.

From the  $d$ -spacings values obtained from SAXS data acquired during the first heating scan (Table 2.3) it is possible to determine the center-to-center distance between the PEO cylinders ( $d_1/\cos 30^\circ$ ), that results of  $\approx 35 \text{ nm}$  in the case of SEO copolymer and  $60 \text{ nm}$  in the case of HSEO sample in the hypothesis of hexagonal morphology. As expected, an

higher value is obtained in the case of the HSEO sample, according to the higher copolymer molecular mass.

From the SAXS data of Fig. 2.2, 2.3, A2.1, 2.5, 2.6 and A2.2 we have evaluated the reduced scattering invariant  $Q$  defined as:

$$Q = \frac{1}{2\pi^2} \int_{q_{min}}^{q_{max}} I(q) q^2 dq \quad (\text{Eq. 2.1})$$

with  $I(q)$  the scattered intensity,  $q = \frac{4\pi \sin \theta}{\lambda}$  the scattering vector and  $q_{min}$  and  $q_{max}$  the minimum and maximum values scanned at low angle. For a biphasic system this parameter is proportional to the contrast and to the product of the volume fraction of the two phases. The so obtained  $Q$  values as a function of the temperature and corresponding first derivative are reported in Fig. 2.7 A, B and A' and B', respectively. A drop of  $Q$  during the first heating (curves a and d of Fig. 2.7) is observed at  $\sim 60$  °C both for SEO and HSEO confirming that the decrease of intensity in SAXS profiles is due to the PEO melting. Similarly, a steep increase of  $Q$  occurs during cooling at  $T \sim -30$  °C (curves b and e of Fig. 2.7) due to PEO crystallization, followed by a new step decrease during second heating at  $T \sim 40$  °C (curves c and f of Fig. 2.7) due to PEO second melting.

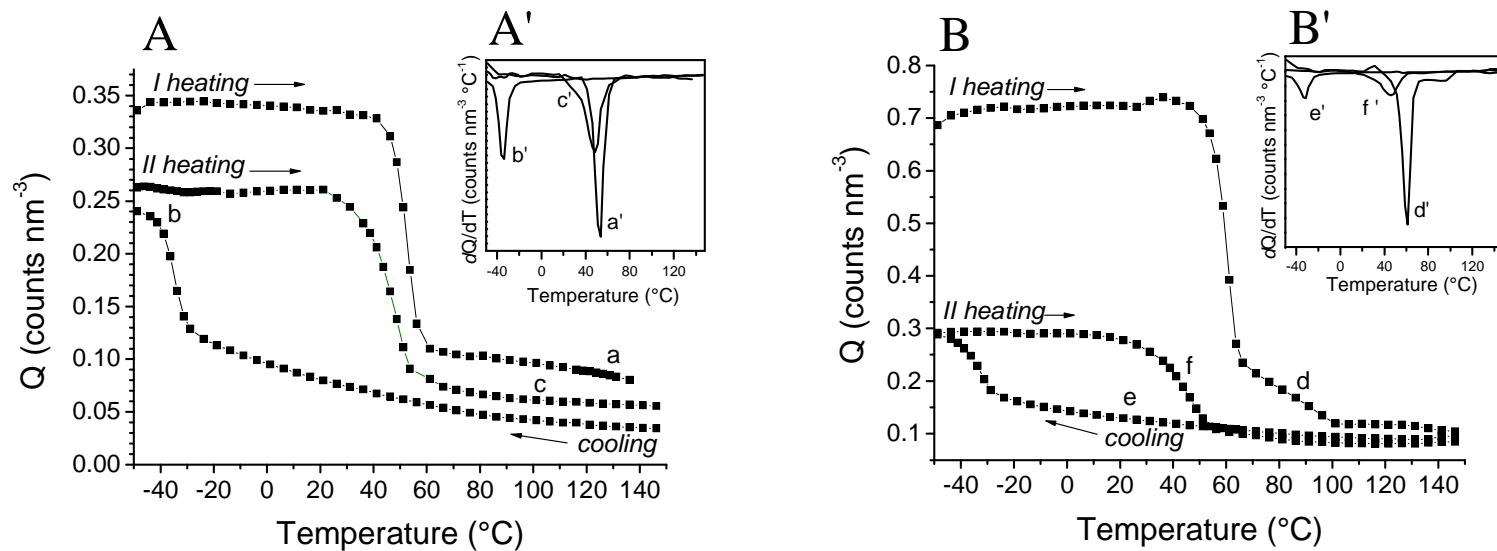


**Fig. 2.7** Reduced scattering invariant ( $Q$ ) as a function of temperature (**A, B**) and corresponding first derivative (**A', B'**) for the SEO ( $a, b, c, a', b', c'$ ) and HSEO ( $d, e, f, d', e', f'$ ) block copolymers calculated according to the Eq. 2.1 from the SAXS profiles at different temperatures acquired during the first heating ( $a, d$ ), the cooling ( $b, e$ ) and the second heating ( $c, f$ ) scans. Values of  $q_{min}$  and  $q_{max}$  equal to  $0.052 \text{ nm}^{-1}$  and  $1 \text{ nm}^{-1}$  have been used, respectively. In the case of curve  $b$   $q_{max} = 0.5 \text{ nm}^{-1}$ .

### 2.3.2 Preparation and characterization of thin films of neat BCPs and BCP nanocomposites containing Pd precursor

Thin films of SEO and HSEO have been prepared by spin-coating dilute solutions of block copolymers (BCPs) in toluene. The spin-coating process to prepare BCPs thin films has been described at the end of paragraph 1.2. Drops of diluted copolymers solutions (1.5 wt%) in the volatile organic solvent (toluene) have been deposited on a solid substrate (silicon). Then, by using an high rotational speed (RPM 4000), the polymer films spread by centrifugal forces and at the same time the volatile solvent rapidly drives off.

Representative SEM images of the so obtained neat SEO and HSEO thin films are reported in figure 2.8 A and B, respectively. In the SEM images, the dark regions correspond to PEO nanodomains and the bright regions to the PS phase. The images exhibit a film structure corresponding to the presence of a well-defined phase separation in which the PEO blocks form a hexagonal array of perpendicular cylinders in the PS matrix.

The distributions of diameters ( $D$ ) and centre-to-centre distances ( $d_{c-c}$ ) of PEO cylinders in neat BCPs thin films are reported in the figure 2.8 C and D, respectively. We notice that the SEO block copolymer shows narrower distributions for the size of both PEO cylinders and centre-to-centre distances than HSEO copolymer (Fig. 2.8). The average cylinders diameter  $D$  is  $\sim 16 \pm 5$  nm and  $\sim 36 \pm 9$  nm for SEO and HSEO, respectively (Fig. 2.8 C). The average cylinder spacing  $d_{c-c}$  is  $\approx 37 \pm 4$  nm for SEO and  $\approx 74 \pm 10$  nm for HSEO (Fig. 2.8 D), in good agreement with the  $d$  values estimated for bulk samples from SAXS data. Therefore the use of the two different block copolymers with different molecular

mass allows controlling the size of the cylindrical domains and domain spacing.

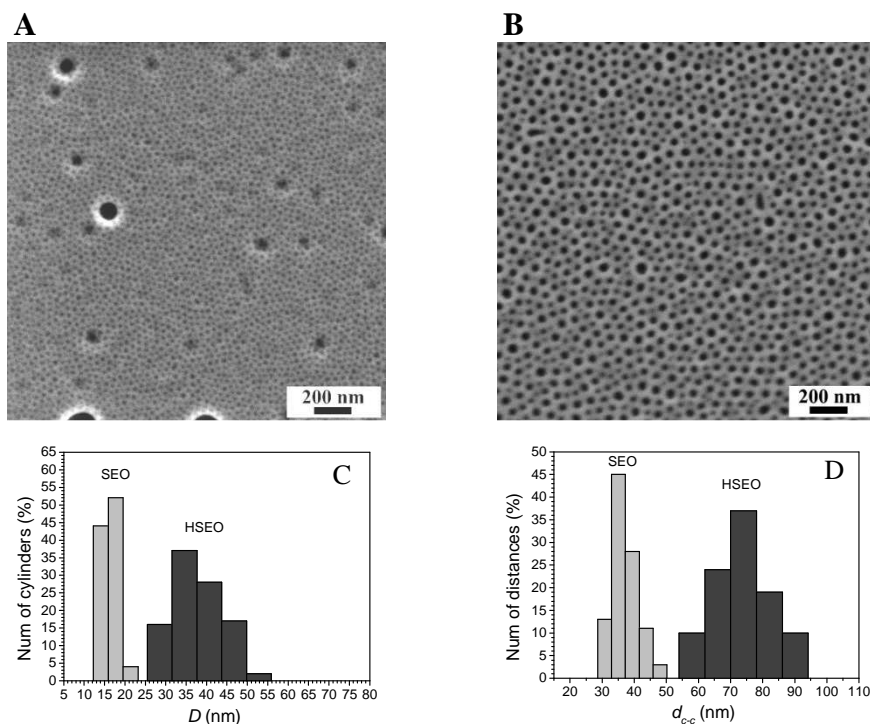


**Fig. 2.8** SEM images of a SEO (A) and HSEO (B) thin films. The films have been prepared by spin coating toluene solutions of block copolymers (1.5wt%) on silicon wafers. The film thickness is  $\sim 47$  nm in both cases. Distribution of (C) diameters ( $D$ ) and (D) centre-to-centre distances ( $d_{c-c}$ ) of PEO cylinders in the thin films of neat SEO and HSEO.

The perpendicular orientation of PEO cylinders in the HSEO and SEO thin films (Fig. 2.8) is due both to the high solvent evaporation rate used during the spin-coating process (the mechanism has been described in paragraph 1.3.1) and to the comparable thickness of the thin films ( $\sim 47$  nm) with the domain spacing of both SEO ( $d_{c-c} \sim 37 \pm 4$  nm) and HSEO ( $d_{c-c} \sim 74 \pm 10$  nm) copolymers (Fig. 2.8 D) [5 b].

BCPs based nanocomposites containing palladium nanoparticles (Pd NPs) have been prepared by using a suitable Pd NPs precursor, the salt Pd(II) acetate. In order to evaluate the precursor dispersion in the

phase separated BCPs, we have studied the morphology of the thin films obtained by spin-coating solutions containing the BCPs and the palladium precursor. The salt Pd(Ac)<sub>2</sub> has been added into BCPs solutions at room temperature and, after vigorous stirring, thin films have been prepared by spin-coating. We have used two different Pd(II) acetate concentrations (26 and 53 wt% with respect to the block copolymers), in order to evaluate the effect of increasing the loading ratio Pd : BCPs. In Fig. 2.9 representative TEM images of the thin films obtained from toluene solutions containing the SEO (A) and HSEO (B) block copolymer (1.5 wt%) including Pd(Ac)<sub>2</sub> in concentration with 26 wt% respect to the BCPs are reported. TEM grids have been observed without any staining procedure. Therefore the high contrast between the dark PEO cylinders and the light PS matrix indicates that the palladium precursor is not uniformly dispersed in the whole BCP, but it is selectively included in the PEO domains. Furthermore whereas PEO cylinders loaded with Pd derivatives are oriented vertically to the substrate in HSEO (Fig. 2.9 B), they are oriented both vertically and parallel to the substrate in SEO (Fig. 2.9A).

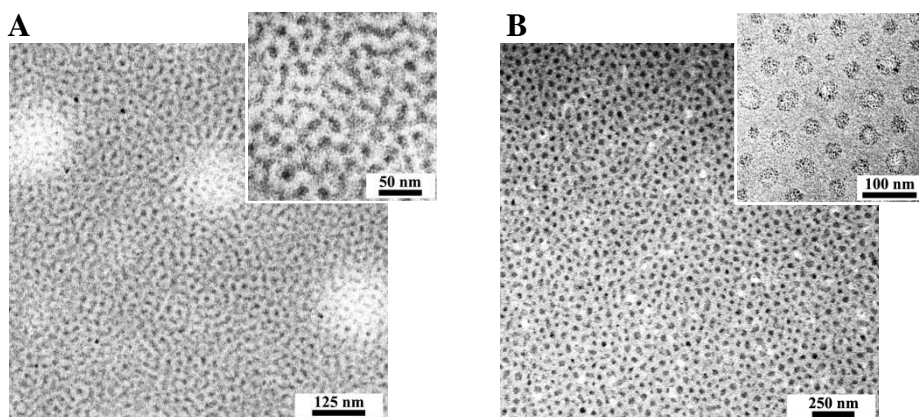


**Fig. 2.9** Bright-field TEM images of thin films prepared by spin-coating toluene solutions containing the block copolymers and the Pd precursor at a concentration of 26wt% with respect to the BCPs in the case of SEO (A) and HSEO (B). No staining procedure was employed on the films before of the TEM observation.

In Fig 2.10 representative TEM and SEM images of the films obtained from toluene solutions containing the SEO (A, A') and HSEO (B, B') block copolymer and Pd(Ac)<sub>2</sub> in a concentration 53 wt% with respect to the BCPs are reported. The phase separated morphology is observed for both block copolymers. Also in this case, TEM images without any staining (Fig. 2.10 A, B) show a high contrast of dark PEO cylinders with respect to PS matrix, indicating that the palladium precursor is selectively included in the PEO cylinders. Moreover, as in the Fig. 2.8, whereas in SEO the PEO cylinders are randomly oriented, in HSEO they keep the vertical orientation. This is confirmed by SEM images (Fig. 2.9 A',B') where the palladium precursor, selectively included in PEO domains, appears bright. The palladium precursor, indeed, due to its hydrophilic nature, preferentially interacts with hydrophilic PEO blocks of the BCPs. The diameter  $D$  and the centre-to-centre distances  $d_{c-c}$  of PEO cylinders loaded with Pd species of Fig. 2.9 and 2.10 are  $D = 17 \pm 5$  and  $d_{c-c} = 35 \pm 9$  nm for SEO (Fig. 2.9A, 2.10 A, A'), and  $D = 37 \pm 4$  and  $d_{c-c} = 75 \pm 10$  nm for HSEO (Fig. 2.9 B, 2.10 B, B').

The thickness of the films containing the palladium precursor (~ 50 nm) (Fig. 2.10) is comparable with the domain spacing of both HSEO and SEO copolymer ( $d_{c-c} = 35 \pm 9$  and  $75 \pm 10$  nm, respectively). In this case a perpendicular orientation of PEO cylinders is expected [5 a]. Anyway, it is worth to note that the filling of PEO cylinders with the palladium precursor can lead to a break-out of the morphology in the case of the SEO copolymer because of the presence of cylinders with a smaller diameter compared to HSEO copolymer ( $D \sim 16 \pm 5$  nm and  $\sim 36 \pm 9$  nm for SEO and HSEO, respectively) (Fig. 2.8 C).

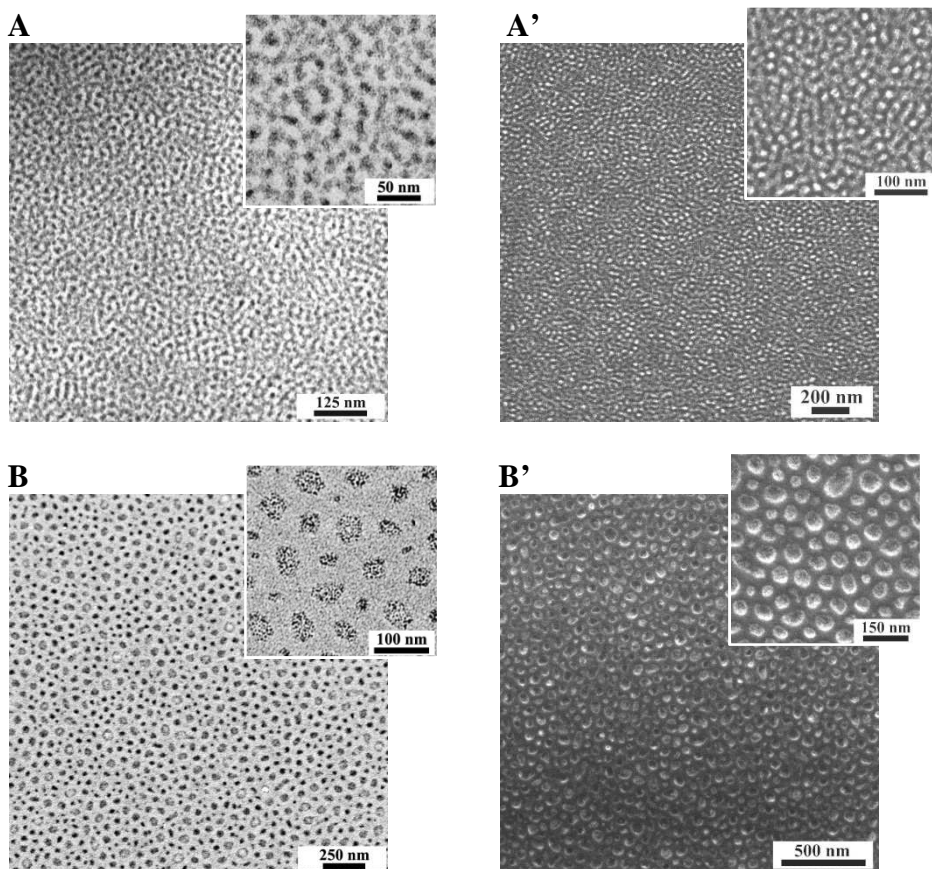


**Fig. 2.10** Bright-field TEM (A) and SEM (A') images of thin films prepared by spin-coating toluene solutions of SEO (1.5 wt%) and Pd precursor (52 wt% with respect to the BCP). Bright-field TEM (B) and SEM (B') images of thin films prepared by spin-coating toluene solutions of HSEO (1.5 wt%) and Pd precursor (54 wt% with respect to the BCP). No staining procedure was employed before of the TEM observation. The film thickness is  $\sim 50$  nm in both cases.

We further investigated the orientation of PEO cylinders by preparing an HSEO thin films by *casting* process, that is the deposition of solutions drops on a solid substrate and the successive *slow* solvent evaporation at room temperature. With this method, films with an higher thickness are obtained. A TEM image of the thin film (thickness  $\sim 0.95$   $\mu\text{m}$ ) is reported in Fig. 2.11. PEO cylinders oriented both perpendicular and parallel to the substrate are observed. Also, it can be noted from the TEM image in Fig. 2.11 that the PEO cylinders perpendicular to the

surface (prevalently present at the right part of the image) appear bright, that is not filled with the Pd precursor. Therefore, using the *casting* procedure, only some PEO cylinders result filled with the palladium precursor.

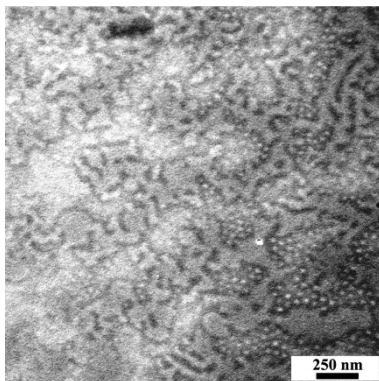


**Fig. 2.11** Bright-field TEM images of thin film prepared by *casting* (slow solvent evaporation) toluene solutions containing the block copolymers HSEO and the Pd precursor at a concentration of 26wt% with respect to the BCP. No staining procedure has been employed on the film before of the TEM observation. The film thickness is ~ 0.95  $\mu\text{m}$ .

It is worth noting that the electron-irradiation during TEM and SEM observations can induce the reduction of Pd(II) salt into Pd(0) and possibly consequent formation of Pd nanoparticles. In this way, Pd NPs are obtained in the films but only in a very small area (the observed region). Therefore a facile route to synthesize BCP based nanocomposites characterized by selective inclusion of Pd NPs in specific domains has been identified, consisting in the dispersion of a Pd salt in a solution in presence of BCPs, preparation of the thin films and successive electron irradiation.

### 2.3.3 BCP-based nanocomposites with Pd nanoparticles prepared in solution

An alternative route for preparation of BCP based nanocomposites containing Pd NPs has been also used. After addition of Pd(II) acetate into BCPs solutions, the mixtures have been heated in a water bath under vigorous, continuous stirring. During this stage, the yellow color of the solution turns brown and finally to gray dark, indicating the formation of Pd NPs (Fig. 2.12). The required reduction time depends on the temperature, as demonstrated in Fig. 2.12, showing photographs of the initial solutions, containing the HSEO block copolymer and the palladium precursor, and of the same solutions after heating at 75 °C (A) and 85 (B) for the indicated times. Higher reduction times are required when a lower temperature is used, to reduce the Pd(II) species.

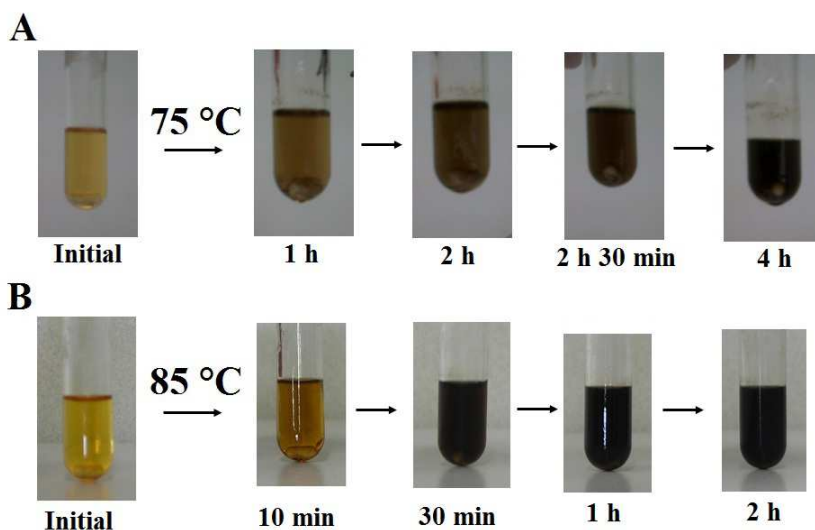


**Fig. 2.12** Photographs of the initial toluene solution containing HSEO (1.5 wt%) and Pd(Ac)<sub>2</sub> (26wt% with respect to the BCP) and of the same solution after heating at 75 °C (A) and 85 °C (B) for the indicated times.

To check the reduction of Pd(II) ions to Pd(0), UV-visible spectra of the solution before and after heating at different times have been measured

(Fig. 2.13). To this aim, the initial toluene solution containing the BCP (1.5 wt%) and the palladium precursor (26 wt% with respect to BCP) (total volume 1 mL) has been diluted by adding 2 mL of toluene and then UV-Vis spectra of Fig. 2.13 have been recorded. Before thermal treatment the solution shows absorption maximum at around 400 nm, which is characteristic of Pd(II) ions (curve a of Fig. 2.13). The peak starts to disappear heating the solution until, after ~ 5 – 6 h (curve d of Fig 2.13), the peak completely disappears, indicating the complete conversion of Pd(II) to Pd(0) species. Therefore the heating of the solution containing the BCP and the palladium precursor results in the direct formation of Pd(0) species in presence of BCP before thin film preparation. According to the literature [15], the reduction of Pd(II) species to Pd(0) in presence of PEO leads to formation of nanoparticles and this process is assisted by PEO chains, which, in absence of other chemical agents, may act both as reducing agent and stabilizer, preventing aggregation.

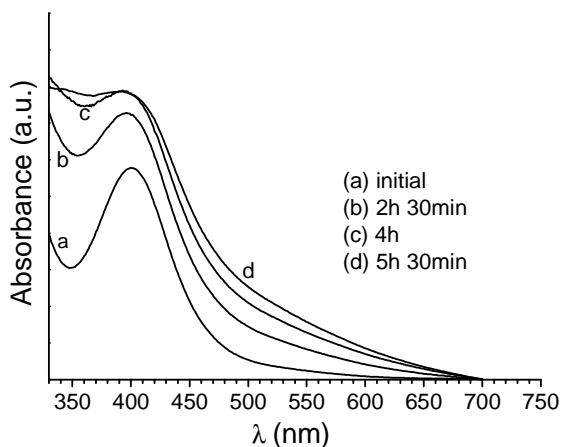


**Fig. 2.13** UV-visible spectrum of a toluene solution containing HSEO (1.5 wt%) and the palladium precursor (26 wt% with respect to the BCP) (a) and of the same solution after heating at 75°C for 2h 30 min (b), 4h (c) and 5h 30 min (d). 2 mL of toluene have been added to 1 mL of the initial solution before recording the UV-Vis spectra.

Thin films have been prepared by spin coating solutions containing the BCPs and the Pd NPs produced by heat treatment at 85 °C for at least 3 h in order to achieve full reduction of Pd(II) species and the morphology

has been studied by TEM (Fig. 2.14 A, B) and SEM (Fig. 2.14 A', B'). Although some palladium aggregates are present, as indicated by black spots in the TEM images (Fig. 2.14 A, B) and white spots in the SEM images (Fig. 2.14 A', B'), due to the formation of Pd aggregates too large to be included in PEO domains, part of Pd NPs result confined in PEO cylinders. The microphase separation of the PS-*b*-PEO directs the spatial distribution of nanoparticles, which result confined in narrow regions and periodically distributed within the microstructure.

To confirm the BCPs role in directing the distribution of NPs, we also have repeated the same procedure for preparation of BCP nanocomposites of Fig. 2.14 using as polymeric matrix, instead of the block copolymers, a simple PEO homopolymer (molecular mass 20000). In this case, only large Pd aggregates are formed, as indicated by TEM image of Fig. 2.15.

The distribution of diameters ( $D$ ) and centre-to-centre distances ( $d_{c-c}$ ) of PEO domains, evaluated from SEM images of Fig. 2.14 A' and B', are reported in Fig. 2.14 C and D, respectively. The average PEO cylinder diameter  $D$  is  $\approx 17 \pm 4$  and  $\approx 40 \pm 10$  nm in the case of SEO and HSEO composites, respectively (Fig. 2.14 C). These values are similar to those obtained in the case of neat BCPs (Fig. 2.8 C). The average values of the centre-to-centre distance ( $d_{c-c}$ ) of PEO domains in the nanocomposites,  $35 \pm 5$  nm and  $\approx 75 \pm 10$  nm in the case of SEO and HSEO, respectively (Fig. 2.8 D), are also very similar to the corresponding average values obtained in the case of neat BCPs (Fig. 2.8 D). In the case of HSEO BCP, larger distributions are obtained for both the diameters ( $D$ ) and centre-to-centre distances ( $d_{c-c}$ ) (Fig. 2.14 C, D).

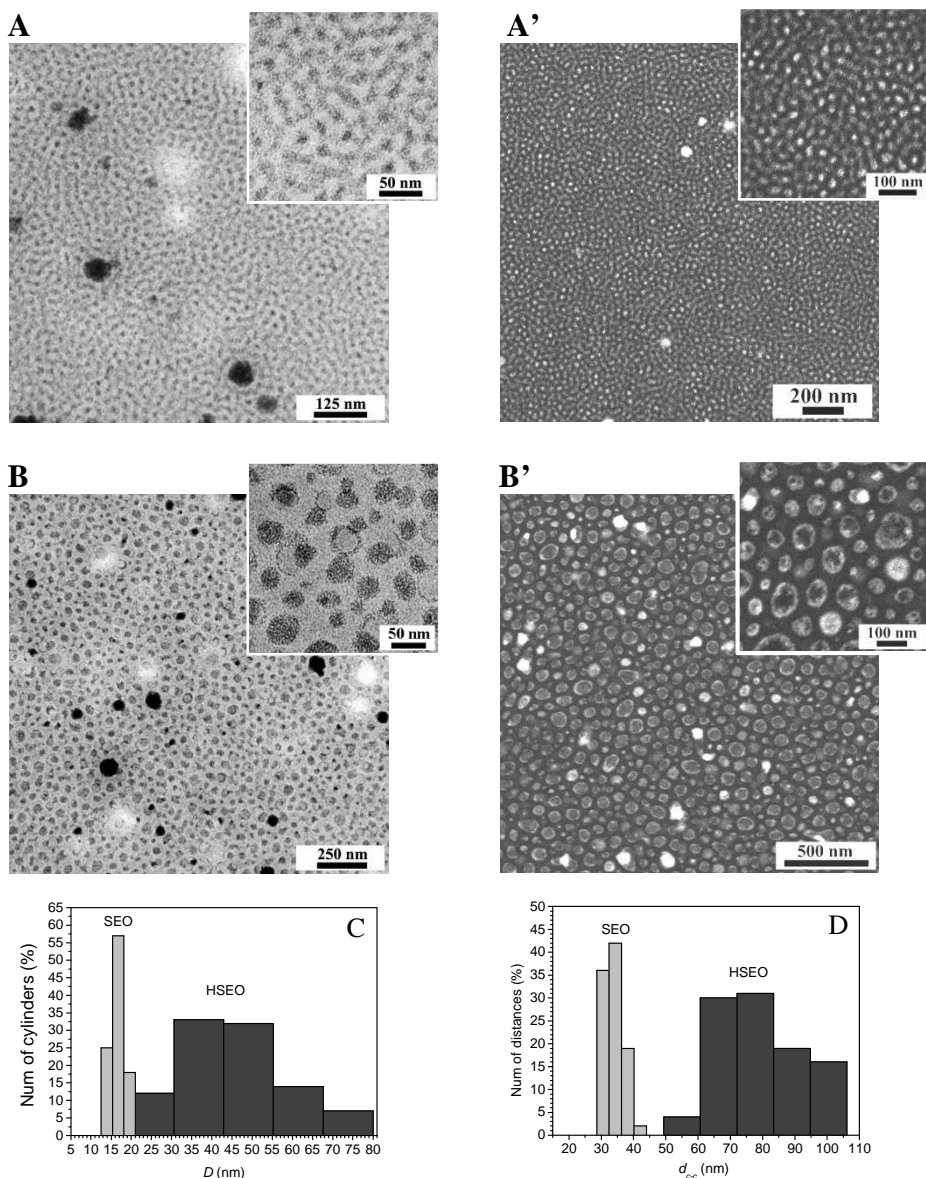


**Fig. 2.14** TEM (A, B) and SEM (A', B') images of thin films prepared by spin-coating a solution of Pd NPs and the block copolymer SEO (A, A') and HSEO (B, B'). The NPs have been prepared by heating at 85°C a 1.5 wt% toluene solution of SEO (A, A') and HSEO (B, B') containing Pd(Ac)<sub>2</sub> (~ 50 wt% with respect to the BCP). No staining procedure has been employed on the films before of the TEM observation. The film thickness is ~ 60 nm in all cases. Distribution of (C) diameters (*D*) and (D) centre-to-centre distances (*d<sub>c-c</sub>*) of PEO cylinders in the BCPs based nanocomposites containing Pd NPs prepared by reduction in solution.

The use of the BCPs with different chain lengths has allowed us to control the dimensions and the distances between PEO cylinders and, consequently, to obtain nanocomposites characterized by Pd nanoclusters placed in domains of average size and at gap distances similar to those of parent BCP nanostructures.

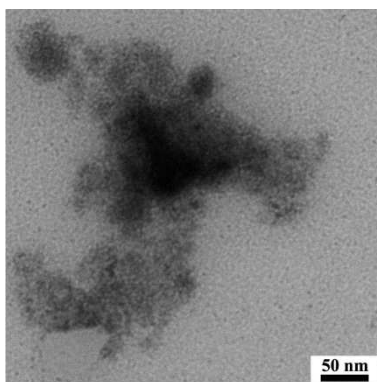


**Fig. 2.15** TEM image of thin films prepared by spin-coating a solution of Pd NPs and the homopolymer PEO. The NPs were prepared by heating at 85°C a 1.5wt% toluene solution of PEO and Pd(Ac)<sub>2</sub> (~ 26 wt% with respect to BCP). No staining procedure was employed on the films before of the TEM observation.

We have tested the ability of our BCPs based nanocomposites containing solution reduced Pd NPs (substrates shown in figure 2.14) to act as catalyst for a palladium-catalyzed Suzuki cross-coupling reaction of an aryl halide (4-bromoanisole) with phenylboronic acid (Fig. 2.16 A). Palladium-catalyzed Suzuki cross-coupling reaction of aryl halides with aryl boronic derivatives is a very suitable and extensively studied approach to C-C bond formation. This reaction is important because biaryl moiety is present in natural products, pharmaceuticals, and herbicides [16] and metallic palladium and palladium complexes are widely used as catalysts for coupling reactions because of high activity and selectivity [17]. We have performed the reaction schematized in Fig. 2.15 A placing the Pd NPs/block copolymers thin film (prepared on a

glass substrate) into a container containing the solvent ethanol/water and the others reagents (4-bromoanisole, phenylboronic acid and the base potassium carbonate). The  $^1\text{H}$  NMR spectrum of the solid product obtained after 1 h reaction is reported in Fig. 2.16 B. The NMR signal at 6.9 ppm confirms the presence of the Suzuki reaction product. Therefore our nanocomposites show catalytic activity for palladium-catalyzed Suzuki cross-coupling reaction of the 4-bromoanisole with phenylboronic acid, confirming the presence of Pd NPs in our thin films.

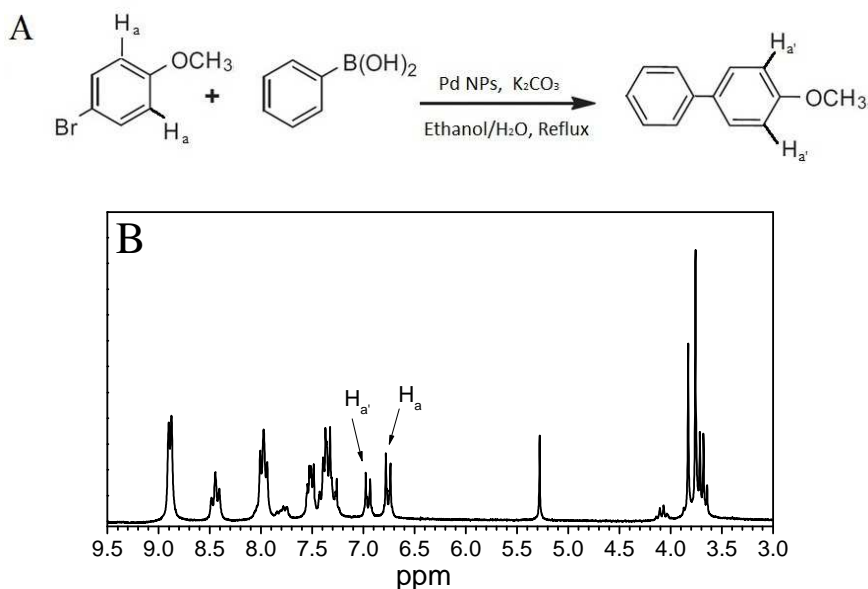


**Fig. 2.16** **A)** Scheme of the reaction between the 4-bromoanisole and the phenylboronic acid, catalyzed by Pd NPs in the presence of a base (potassium carbonate). **B)**  $^1\text{H}$  NMR spectrum of the mixture obtained after 1 h reaction in refluxing conditions. The signal at 6.9 ppm ( $\text{H}_{a'}$ ) confirms the presence of the Suzuki reaction product.  $\text{CHCl}_3$  ( $\delta = 7.26$  ppm respect to TMS) has been used as internal standard.

The presence of metallic Pd in our nanocomposites has also confirmed by grazing incidence wide angle scattering (GIWAXS) experiments. With GIWAXS technique, the limitations of the conventional X-ray scattering with respect to extremely small sample

volumes in the thin-film geometry are overcome [18]. The Fig. 2.17 gives a schematic drawing of the basic set-up used in the GIWAXS experiments. The transmission geometry is replaced by a reflection one. This yields a surface sensitivity, which enables the investigation of surfaces and thin films. With a two dimensional detector, the scattering intensity is recorded at one fixed angle of incidence ( $\alpha_i$ ) of the X-ray beam onto the sample surface.

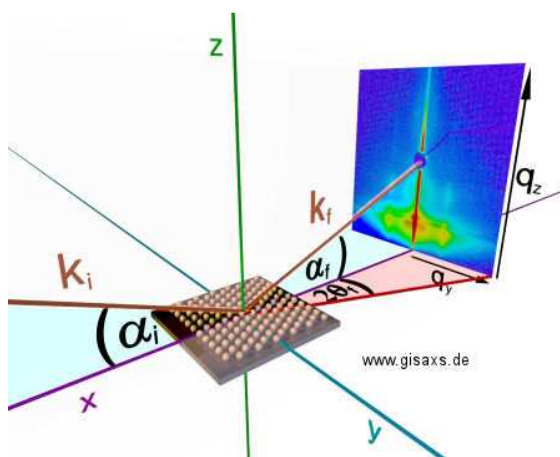


**Fig. 2.17** Schematic drawing of the experimental GIWAXS set-up. The incident angle is denoted  $\alpha_i$  and the exit angle  $\alpha_f$ .  $q_z$  and  $q_y$  are the wavevector components perpendicular and parallel to the sample surface, respectively. From <http://www.gisaxs.de/theory.html>.

Instead of handling the complete two-dimensional intensity distribution, the analysis of the scattering data can be reduced to two distinct cuts: a horizontal cut at constant  $q_z$  value and a vertical cut at constant  $q_y$ , intersecting at  $q_z = q_y = 0$  corresponding to the direction of direct beam.

In Fig. 2.18 A the GIWAXS two dimensional data of our HSEO based nanocomposite (shown in Fig. 2.14 B and B') is reported. The corresponding intensity along a vertical cut is reported in Fig. 2.18 B. The 200 reflection peak of metallic Pd is visible at  $3.1 \text{ \AA}^{-1}$  [19]. It appears as a Debye Scherrer ring in the 2D image (Fig. 2.18 A) indicating that Pd nanocrystals are randomly oriented in the PEO nanodomains.

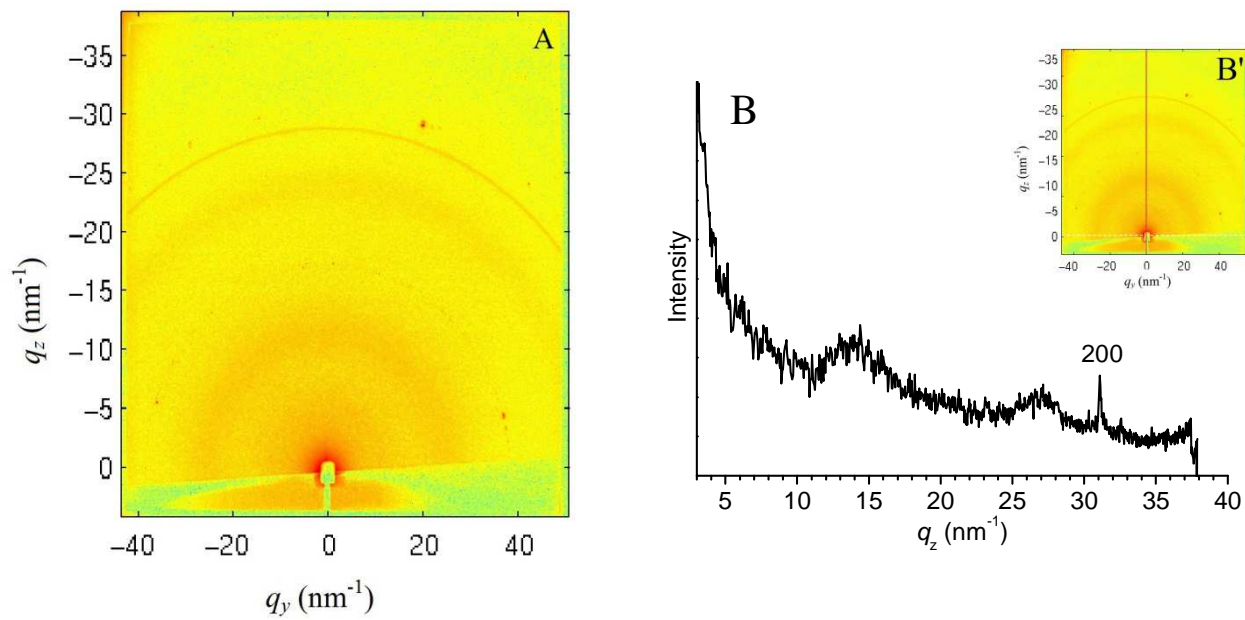


**Fig. 2.18** A) Two dimensional GIWAXS pattern of our HSEO based nanocomposites filled with Pd NPs. B) Intensity profile read along the vertical cut indicated in red in the inset B'.

### 2.3.4 Preparation of PdO nanoparticles on silicon substrates

The thin films containing the block copolymers (SEO or HSEO) and the Pd nanoparticles (shown in Fig. 2.14), prepared on silicon substrates, have been heated at 600 °C in air for 4 h.

In figure 2.19, the thermogravimetric analysis (TGA) of the HSEO block copolymer is reported. It is apparent that at  $\approx 460$  °C the weight loss of the BCP is almost complete. This indicates that the 600°C heat treatment performed on thin film our nanocomposites produces complete removal of the polymeric matrix. At this temperature, the formation of PdO nanoparticles is expected [20].

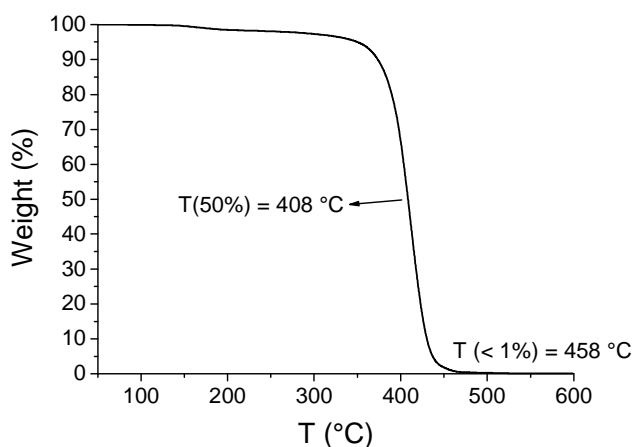


**Fig 2.19** TGA curve of the HSEO block copolymer recorded in  $N_2$  (g) atmosphere. The temperatures corresponding to 50% and  $\approx 99$  % weight loss are indicated.

Therefore the treatment of our BCP/Pd NPs composites at elevated temperatures in air leads to the simultaneous removal of the polymeric matrix and the formation of PdO nanoparticles on the solid and conductive support. SEM images of the obtained PdO NPs on silicon supports are reported in Fig. 2.20.

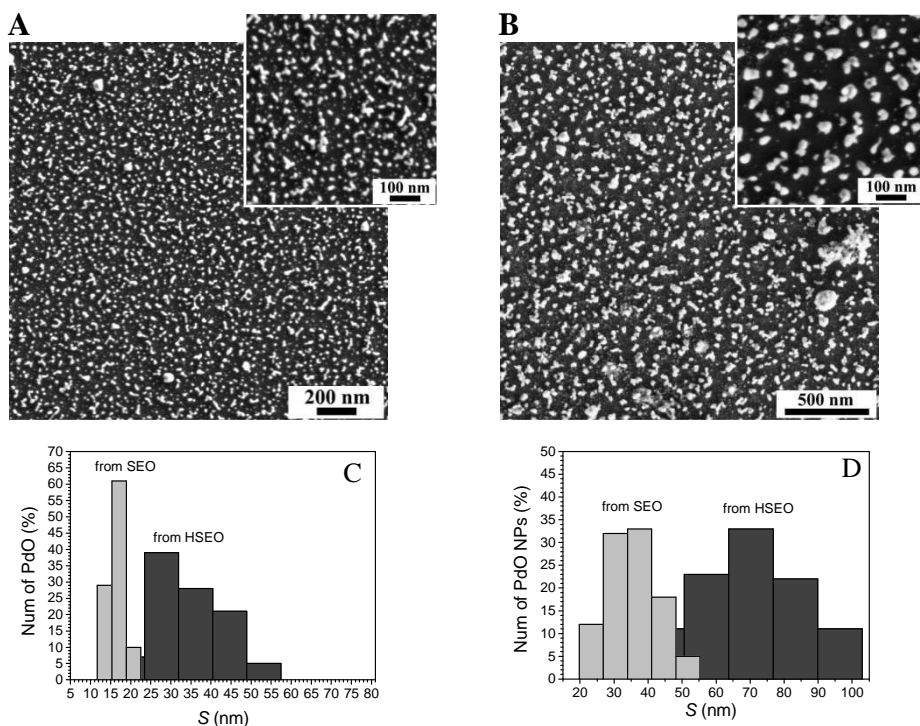


**Fig. 2.20** SEM images of PdO nanoparticles on silicon wafers obtained after the oxidative treatment of the films containing Pd NPs and SEO (**A**) and HSEO (**B**). Distribution of the (**C**) size ( $S$ ) and (**D**) centre-to-centre distance ( $d_{c-c}$ ) of the obtained PdO NPs using SEO and HSEO as template.

The presence of PdO nanoparticles has been also confirmed by GIWAXS experiments (Fig. 2.21). In the GIWAXS profile (Fig. 2.21 B), the 101, 002, 110 and 112 reflection peaks of PdO are clearly apparent [21].

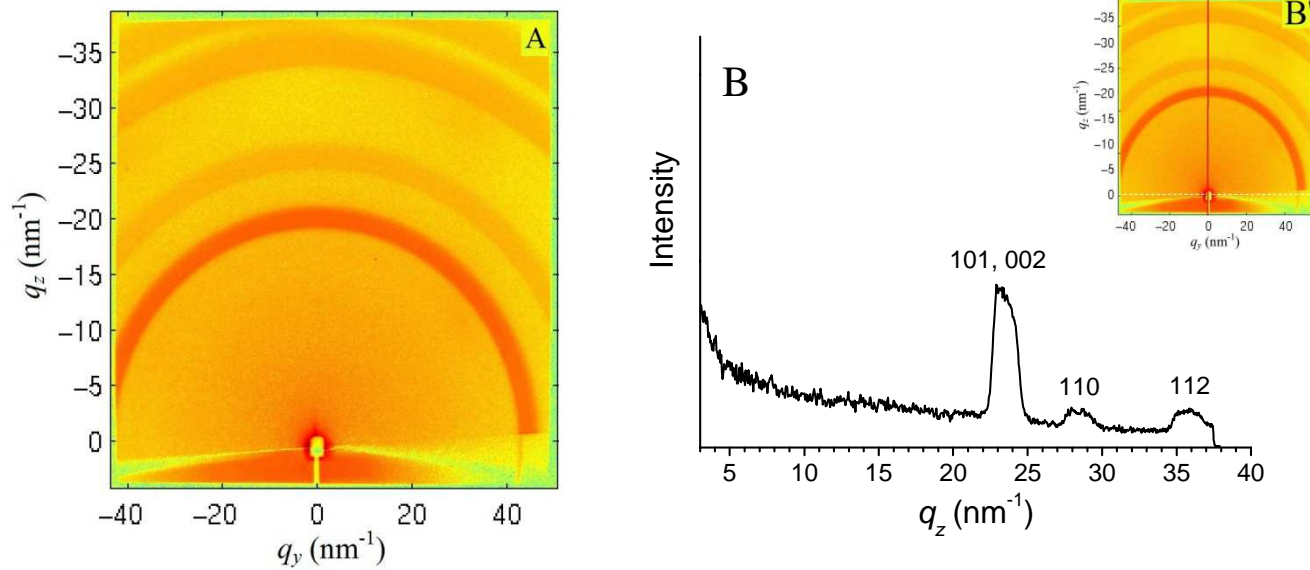


**Fig. 2.21** A) Two dimensional GIWAXS pattern of the PdO NPs on a silicon substrate. B) Intensity profile read along the vertical cut indicated in red in the inset B'.

The distribution of the size ( $S$ ) and centre-to-centre distance ( $d_{c-c}$ ) of the so obtained PdO NPs are reported in Fig. 2.20 C and D, respectively. The PdO NPs average size  $S$  (Fig. 2.20 C) is  $\approx 17 \pm 5$  nm for the PdO nanoparticles obtained after the removal of the polymeric matrix SEO and  $\approx 34 \pm 9$  nm for the PdO nanoparticles obtained using the HSEO block copolymer as template. The obtained values well match the average diameters of the corresponding PEO cylinders in the BCPs used as template (Fig. 2.8 C). The PdO NPs average centre-to-centre distance is  $\approx 37 \pm 9$  for the PdO nanoparticles obtained after the removal of the polymeric matrix SEO and  $\approx 74 \pm 12$  nm for the PdO nanoparticles obtained using the HSEO block copolymer as template (Fig. 2.20 D), in good agreement with the values of the center-to-center distance of PEO domains in the corresponding nanocomposites (Fig. 2.14 D). This indicates that after the polymer removal the resulting PdO NPs maintain the same size and spacing of the PEO cylinders in the parent block copolymers.

The use of the two BCPs with different chain lengths allowed us to control the dimensions and the distances between microdomains and, consequently, to obtain arrays of PdO NPs on the solid support characterized by different diameter and gap distance, mirroring the pattern and the characteristic nanodimensions of the parent block copolymer template.

## 2.4 Conclusions to Chapter II

In this Chapter we have reported a simple and cost effective process for tuning the characteristic size (diameter and lateral spacing) of palladium (Pd) nanoclusters and palladium oxide (PdO) nanoparticles on solid supports, by using two polystyrene-*block*-poly(ethylene oxide) copolymers (PS-*b*-PEO) having different molecular mass as templates. We have selected PS-*b*-PEO as block copolymers because of the favorable interaction of PEO blocks with the used metal nanoparticles precursor (palladium(II) acetate) and we have generated Pd nanoparticles by reduction of Pd(II) ion in the presence of BCPs, without disturbing the regular microdomain structure of block copolymers. The resulting nanocomposite thin films show the metal Pd nanoparticles selectively included in cylindrical PEO nanodomains, with a nanoclusters average diameter and gap distance mirroring the parent BCP used as template. The treatment of the nanocomposites at elevated temperatures in air leads to the formation of PdO NPs on the solid support. The average diameter and the centre-to-centre spacing are still maintained. This part of the thesis work is an example confirming that the ability to control the length and the spatial and orientational organization of block-copolymer morphologies makes these materials particularly attractive as scaffolds for engineering of ordered nanocomposites in which the distribution of the guest particles is guided by the ordering of the host matrix. The ability to create morphologically and dimensionally controlled Pd and PdO nanoparticles would be the key point in the process of transforming these systems from promising materials into integrated devices and the compatibility of these systems with the existing silicon-based technology makes them even more attractive. Also, due to the Pd and PdO high

capability to absorb large amounts of hydrogen, interesting recent examples of hydrogen sensing devices based on palladium have been reported [4 *a-c*, 22]. This could be expand the possible scientific and technological applications of our materials as innovative materials for the construction of new hydrogen sensing devices.

## BIBLIOGRAPHY CHAPTER II

- [1] a) A. Balanta, C. Godard, C. Claver, *Chem. Soc. Rev.* **2011**, 40, 4973. b) D. Astruc, F. Lu, J. R. Aranzaes, *Angew. Chem. Int. Ed.* **2005**, 44, 7852. c) K. C. Nicolaou, P. G. Bulger, D. Sarlah, *Angew. Chem. Int. Ed.* **2005**, 44, 4442. d) J. P. Corbet, G. Mignani, *Chem. Rev.* **2006**, 106, 2651.
- [2] a) Y. Ozawa, Y. Tochihara, M. Nagai, S. Omi, *Chem. Eng. Sci.* **2003**, 58, 671. b) J. G. McCarty, *Catal. Today* **1995**, 26, 283. c) T. L. Stuchinskaya, I. V. Kozhevnikov, *Catal. Commun.* **2003**, 4, 417. d) P. Euzen, J. H. L. Gal, B. R. Rebours, G. Martin, *Catal. Today* **1999**, 47, 19.
- [3] S. S. Shendage, U. B. Patil, J. M. Nagarkar, *Tetrahedron Letters* **2013**, 54, 3457.
- [4] a) B. D. Adams, A. Chen, *Materials Today* **2011**, 14, 282. b) E. Lee, J. M. Lee, J. H. Koo, W. Lee, T. Lee. *International journal of hydrogen energy* **2010**, 35, 6984. c) X. Q. Zeng, M. L. Latimer, Z. L. Xiao, S. Panuganti, U. Welp, W. K. Kwok, T. Xu, *Nano Lett.* **2011**, 11, 262. d) E. Sennik, N. Kilinc, Z. Z. Oeztuerk, *J. Appl. Phys.* **2010**, 108, 054317/1.
- [5] a) M. R. Bockstaller, R. A. Mickiewicz, E. L. Thomas, *Adv. Mater.* **2005**, 17, 1331. b) M. J. Fasolka, A. M. Mayes, *Annu. Rev. Mater. Res.* **2001**, 31, 323.
- [6] a) L. J. Fetters, D. J. Lohse, D. Richter, T. A. Witten, A. Zirkel, *Macromolecules* **1994**, 27, 4639. b) J. Brandrup, E. H. Immergut, eds. *Polymer handbook* **1989**, New York: John Wiley & Sons.
- [7] I. W. Hamley, V. Castelletto, *Prog. Polym. Sci.* **2004**, 29, 909.
- [8] E. A. Grulke, J. Brandup, E. H. Immergut. *Polymer Handbook* **1999**, Wiley, New York.
- [9] A. J. Muller, V. Balsamo, M. L. Arnal, T. Jakob, H. Schmalz, V. Abetz. *Macromolecules* **2002**, 35, 3048.

- [10] a) H. Chen, S. Hsiao, T. Lin, K. Yamauchi, H. Hasegawa, T. Hashimoto, *Macromolecules* **2001**, 34, 671. b) H. Chen, J. Wu, J. Lin, *Macromolecules* **2001**, 34, 6936.
- [11] J. Lheritier, A. Chauvet, J. Masse, *Thermochim. Acta* **1994**, 241, 157.
- [12] a) I. W. Hamley, *The physics of block copolymers* **1998**, Oxford, Oxford University Press. b) I. W. Hamley, *J. Phys. Condens. Mat.* **2001**, 13, R643.
- [13] S. M. Mai, J. P. A. Fairclough, N. J. Terrill, S. C. Turner, I. W. Hamley, M. W. Matsen, A. J. Ryan, C. Booth, *Macromolecules* **1998**, 31, 8110.
- [14] a) M. W. Matsen, F. S. Bates, *Macromolecules* **1996**, 29, 1091. b) J. P. A. Fairclough, S. M. Mai, M. W. Matsen, W. Bras, L. Messe, S. Turner, A. J. Gleeson, C. Booth, I. W. Hamley, A. J. Ryan, *J. Chem. Phys.* **2001**, 114, 5425.
- [15] a) C. Luo, Y. Zhang, Y. Wang, *Journal of Molecular Catalysis A: Chemical* **2005**, 229, 7. b) F. A. Harraz, S. E. El-Hout, H. M. Killa, I. A. Ibrahim, *Journal of Catalysis* **2012**, 286, 184.
- [16] a) A. Fihri, M. Bouhrara, B. Nekoueishahraki, J. M. Basset, V. Polshettiwar, *Chem. Soc. Rev.* **2011**, 40, 5181. b) Z. Z. Zhou, F. S. Liu, D. S. Shen, C. Tan, L. Y. Luo, *Inorg. Chem. Commun.* **2011**, 14, 659. c) P. J. Hajduk, M. Bures, J. Prastgaard, S. W. Fesik, *J. Med. Chem.* **2000**, 43, 3443.
- [17] a) J. Mondal, A. Modak, A. Bhaumik, *J. Mol. Catal. A: Chem.* **2011**, 350, 40. b) K. Sarkar, M. Nandi, M. Islam, M. Mubark, A. Bhaumik, *Appl. Catal. A* **2009**, 352, 81. c) A. F. Littke, G. C. Fu, *Angew. Chem. Int. Ed.* **2002**, 41, 4176. d) A. N. Marziale, D. Jantke, S. H. Faul, T. Reiner, E. Herdtweck, J. Eppinger, *Green Chem.* **2011**, 13, 169.
- [18] P. Müller-Buschbaum, *Anal. Bioanal. Chem.* **2003**, 376, 3.
- [19] H. E. Swanson, E. Tatge. *Natl. Bur. Stand.* **1953**, Circ. 539 I, 21.
- [20] a) S. Jodeh, *Jordan Journal of Chemistry* **2008**, 3, 189. b) R. J. Farrauto, J. K. Lampert, M. C. Hobson, E. M. Waterman, *Applied*

*Catalysis B: Environmental* **1995**, 6, 263. c) A. K. Datye, J. Bravo, T. R. Nelson, P. Atanasova, M. Lyubovsky, L. Pfefferle, *Applied Catalysis A: General* **2000**, 198, 179.

[21] J. Welton-Holzer, G. McCarthy, North Dakota State University, Fargo, North Dakota, USA. ICDD Grant-in-Aid **1989**.

[22] a) I. N. Nikolaev, V. V. Krashevskaya, *Measurement Techniques* **2004**, 47, 304. b) Y. T. Lee, J. M. Lee, Y. J. Kim, J. H. Joe, W. Lee, *Nanotechnology* **2010**, 21, 165503.

**BLOCK COPOLYMERS BASED NANOPOROUS MATERIALS FOR  
BIOMOLECULES IMMOBILIZATION****3.1 Introduction to Chapter III****3.1.1 Biosensors: general principles**

In the last decades sensor-related research has experienced explosive growth, due to the necessity to detect in selective way and at low cost an increasing number of analytes in different areas such as health care, food safety, environmental monitoring and security controls [1]. According to the common nomenclature proposal (IUPAC) [2], a chemical sensor is a device that transforms a chemical information, ranging from the concentration of a specific sample component to total composition analysis, into an analytically useful and measurable signal. It is formed by two integrated parts: a receptor element (molecular recognition material), that selectively binds and recognises the compound to be detected (target molecule), and a transducer, that converts the chemical information into a physically measurable signal. Biosensors are a subgroup of chemical sensors in which the receptor element is an immobilized biological sensing element (enzymes, antibodies, nucleic acids, receptors), able to bind the target molecule [2 c, 3] (Fig. 3.1). The biological recognition system, usually a receptor protein, antibody or

enzyme, translates the information from the biochemical domain into a chemical or physical output signal.

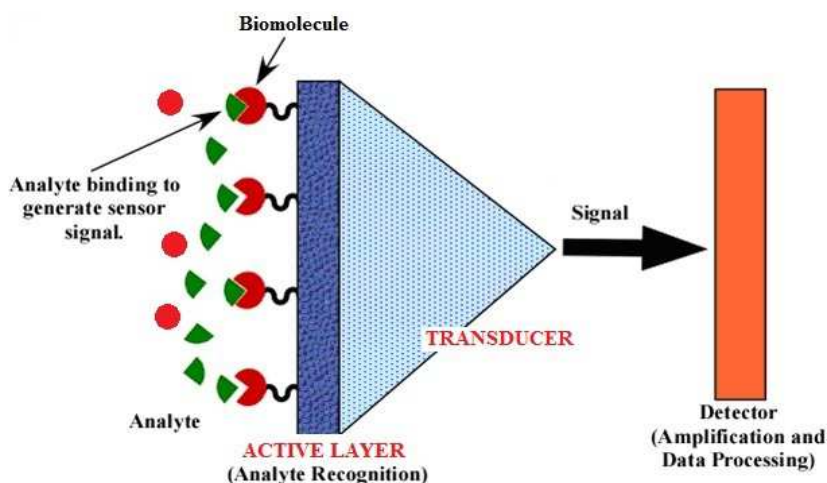


**Fig. 3.1** Scheme of a biosensor. It consists of three different but strictly connected elements: **1**) the selector (biomolecules), immobilized on the active layer, binds and recognizes the compound to be detected (analyte); **2**) the transducer transforms the signal from the output domain of the recognition system to a physically measurable signal and **3**) the detector permits to amplify, process and display the chemical-physical signal into a suitable form.

Due to the intrinsic, highly selective properties of the biomolecular species in comparison to the inorganic catalysts, biosensors can measure compounds in a very selective way if compared with traditional analytical techniques [4]. Furthermore, biosensors possess many unique features such as compact size, simplicity of use, one-step reagentless analysis, absence of radioactivity, etc., that make them very attractive alternatives to conventional analytic techniques.

The development of new biomaterials and fabrication techniques has given rise to biosensors that can sensitively characterize and quantify biological reactions [5]. Nowadays some interesting commercial biosensors are available for detecting different substrates like glucose, lactate, urea and penicillin [6], but their number is still relatively very

small in comparison to the large theoretical efforts in their design and development. Several drawbacks have impeded biosensors large-scale application and performance as reliable analytical instruments [7]. They normally suffer from one severe drawback, namely instability of the biological receptor molecules, that are subject to denaturation. Increasing the stability of the biomolecule is one of the major issues in biosensor research. Biological activity can be preserved by storing the biosensor under the right conditions, e.g., buffer, pH, low temperature. This may give long off-line lifetimes, improving the so-called *shelf-stability*. The stability of the biological element can be also enhanced by immobilizing the biomolecules on appropriate solid supports. For this reason, one key factor in biosensor construction is the development of immobilization technologies for stabilizing biomolecules and tethering them to surfaces. This aspect will be discussed in the next paragraph. The usual aim is to produce a thin film of immobilized biologically active material on or near the transducer surface which responds only to the presence of one or a group of materials or substances requiring detection.

Also, the immobilization of biomolecules on surfaces is becoming a significant part of biochemistry and molecular biology [8] due to multiple applications in DNA microarray construction [9] and detection of proteins involved in signaling networks in cell [10].

### **3.1.2 Immobilization of the biological element**

Biosensors require proteins and enzymes, which need to be stabilized in their natural conformation. The operational and storage stabilities of the biosensor is the most critical issue, since controlling the stability of the biological recognition element is very difficult. The

biological recognizing systems are from their nature not very stable in a biosensor membrane environment, since they are sensitive to denaturation or inactivation by either fluctuations in the pH, the temperature, as well in the presence of organic solvents and detergents usually employed for the construction of a biosensor [11].

Different approaches have been utilized to improve enzyme stability, including genetic engineering [12], chemical modification [13], inclusion of additives [14] and immobilization to various matrices. In particular, the immobilization of enzymes on inorganic, organic or polymeric matrices have shown to be an efficient stabilization method that increases the enzyme rigidity preventing the possibility to unfold and deactivate [15].

There are a number of requirements that an efficient immobilization technique must satisfy: (i) the biological component must retain substantial biological activity when attached to the sensor surface; (ii) the biological film must remain tightly associated with the sensor surface whilst retaining its structure and function; (iii) the immobilized biological film needs to have long-term stability and durability; and (iv) the biological material needs to have a high degree of specificity to a particular compound.

A number of methods have been described for the immobilization of enzymes and proteins on surfaces and within various matrices (Fig. 3.2):

- (1) adsorption at a solid surface;
- (2) covalent binding to a surface;
- (3) entrapment within a membrane, surfactant matrix, polymer or microcapsule;
- (4) cross-linking between molecules.

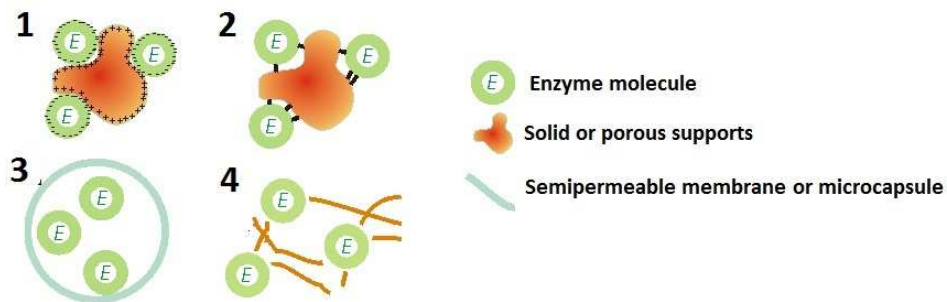


**Fig. 3.2** Principal methods of biomolecules immobilization: adsorption at a solid support (1), covalent binding to a surface (2), entrapment within a membrane or microcapsule (3) and cross-linking between molecules (4).

1) Adsorption of biomolecules from solution onto solid surfaces can proceed via physical interactions (van der Waals forces, ionic binding or hydrophobic forces). Protein adsorption at solid/liquid interfaces has been widely studied using a variety of experimental techniques such as ellipsometry, Surface Plasmon Resonance (SPR), Quartz Crystal Microbalance (QCM), radiolabeling, fluorescence microscopy, neutron reflection, circular dichroism and infrared spectroscopy [16]. Although SPR, QCM and radiolabeling allow determining the protein adsorbed amount, they cannot establish the structure of the adsorbed layer. On the reverse, circular dichroism and infrared spectroscopy allow probing the change of secondary and tertiary structure of the protein upon adsorption but they do not give information on the adsorbed amount [17]. Neutron reflectivity is a powerful technique, which allows simultaneously to determine the thickness and the volume fraction of the adsorbed protein layers leading to the adsorbed amount and also to identify if the adsorbed proteins retain their native structure or are denatured at interfaces [18].

The main advantage associated with direct adsorption onto solid surfaces is that it is a simple method which can be performed under mild conditions. The direct adsorption of proteins on polystyrene microtiter

wells for use in enzyme linked immunosorbent assays (ELISA) has over the years become a common immobilization method due to its simplicity and low cost. Several research groups have shown that direct adsorption to polystyrene surfaces can lead to conformational changes within the protein molecule and hence a loss in functionality of such molecules [19 *a*]. Despite such problems, the simple adsorption assay remains a major clinical assay system in use today. There have recently been a number of investigations into the effects of different preparation methods on the functionality of proteins adsorbed onto polystyrene surfaces [19 *b*].

2) An alternative approach to the attachment of biomolecules to sensor surfaces is through covalent binding, where biomolecules are immobilized on solid surfaces through the formation of defined linkages (Fig. 3.2). Procedures resulting in minimal loss of biomolecule activity have been employed [20]. Biomolecules have many functional groups present for covalent immobilization onto surfaces; these include amino-acid side chains (e.g. amino groups of lysine), carboxyl groups (aspartate and glutamate), sulfhydryl groups (cysteine), phenolic, thiol and imidazole groups. Covalent coupling between the enzyme or protein and the solid support is best achieved through functional groups on the biomolecule which are not required for its biological activity. Covalent binding has the advantage that the biomolecule is generally strongly immobilized on the surface and therefore unlikely to detach from the surface during use. Suitable functional groups which are available for covalent attachment are also present on some transducer materials (hydroxyl groups on silica). Most surfaces, however, have to be modified in order to introduce a functionality which may be coupled with the enzyme or protein.

3) The procedure of entrapping biological components in polymer gels, membranes or surfactant matrices has been used with success in the past (Fig. 3.2) [21]. It is a relatively straightforward process. A number of polymers have been used for the inclusion of enzymes, cells and organelles. These include polyvinyl alcohol, polyvinyl chloride, polycarbonate, polyacrylamide and cellulose acetate. Methods used for the entrapment of biological components, however, suffer from the drawback of leakage of the biological species during use, resulting in a loss of activity.

4) Cross-linking entrapped enzymes or proteins can often alleviate the problem of biomolecule leakage. Cross-linking of biological components by means of a multifunctional reagent affords enhanced stability of the adsorbed enzymes or proteins that are covalently bound onto the support. Glutaraldehyde, which couples with the lysine amino groups of enzymes, is by far the most common cross-linking agent in biosensor applications [22]. There are a number of disadvantages associated with this method: (i) it is difficult to control the reaction; (ii) the protein/enzyme layer formed is usually gelatinous and not rigid; (iii) large amounts of biological material are required; (iv) cross-linking can result in the formation of multilayers of protein/enzyme, resulting in low activity of the immobilized layers; (v) large diffusional barriers to the transport of the biological species may result, leading to retarded interactions.

Although stabilization of enzymes has been of interest for many years, new opportunities for stabilizing enzymes with improved intrinsic and operational stabilities have arisen with the development of

nanomaterials and nanostructured materials. In particular, nanoporous materials are exciting candidates for enzyme immobilization compared with conventional materials due to their large surface area and opened pore structure that allows high enzyme loadings [23 *a*]. It has been found that porous materials can act as stabilization matrices to protect the biomolecule from irreversible unfolding, enhancing sensor performance, and this concept has been applied to the design of biosensors. Experimental studies point to the stability of enzymes immobilized in various porous matrices, such as carbon, silica, and aluminosilicates [23 *a, b*]. On the other hand, if biomolecules are deposited on a relatively flat surface, they are likely to undergo a conformational change or denaturation [23 *c - e*].

The final performance of a biosensor is inextricably bound with the immobilization technique employed. Most of the immobilization techniques used to date are far from giving reproducible results, and many of the procedures still in use have evolved from trial and error experimentation. Although current immobilization methods allow preparation of thin biological films which have a highly specific attraction to certain species of molecule, these techniques often result in a loss in the native conformation and hence in the activity of the biological material. If a breakthrough could be achieved in immobilization technologies, in which the loss of activity of the attached biological film is limited, many of the present disadvantages of biosensors would be overcome. Since the immobilization technique used to attach the biological material to the sensor surface is crucial to the operational behavior of the biosensor, realistic strategies for the development of new supports able to efficiently immobilize biomolecules are essential for practically useful biosensors.

### 3.1.3 Description of the chapter work

As widely discussed in paragraph 1.4.2, block copolymers (BCPs) represent a class of materials that exhibit unparalleled versatility in the creation of nanoporous materials, that can be generated by selective removal of one component from a self-assembled BCP (Fig. 1.8). The obtained materials will exhibit the pore size and pore topology of their parent structures and can be used as nanolithographic masks, separation membranes, nanomaterial template [24]. To our knowledge, very few examples are reported in literature about the possibility to use BCP based nanoporous thin films as supports to physically absorb proteins and enzymes [25]. The nano porosity could enhance the amount of absorbed molecules and could facilitate the retention of the native structure of an enzyme and its activity; thus making these materials suitable as a novel biosensing platform. The controlled introduction of a specific chemical functionality within the pore space is another critical issue to design a porous material useful for biosensing applications. In particular, the presence of a specific pore wall functionality in BCP based porous materials is important to regulate the hydrophilicity of the resulting material and to design protocols to covalently link biomolecules at the obtained porous materials.

In this chapter, we report the fabrication of porous block copolymer thin films able to act as ideal supports for the physical immobilization of specific biomolecules. In particular, we have designed a nanoporous thin film with well-defined architecture containing functionalized pores delimited by hydrophilic walls, exploiting self-assembly of lamellar block copolymers and the concept of sacrificial block. The strategy is reported in Fig. 3.3. Exploiting the partial

miscibility of polyethylene oxide (PEO) and poly(L-lactide) (PLLA) [26], we have employed a blend of polystyrene-*block*-poly(L-lactide) (PS-*b*-PLLA) and polystyrene-*block*-poly(ethylene oxide) (PS-*b*-PEO) diblock copolymers to generate thin films with a single-phase lamellar morphology in which the PEO and PLLA blocks form lamellae within a PS matrix (Fig. 3.3 a). Then, by selective chemical etching of the PLLA blocks, the nanoporous thin film, patterned with nanometric channels containing pendant hydrophilic PEO chains, has been generated (Fig. 3.3 b). This strategy has allowed us to control the hydrophilicity of the final material by controlling the PS-*b*-PEO amount in the blend and, also, permits to obtain a porous material with suitable functional groups (terminal hydroxyl group on PEO) which could be eventually used to design protocols for the covalent attachment of biomolecules. We have used the obtained porous materials to physically adsorb specific biomolecules (Fig. 3.3 c) that can eventually recognize an analyte of interest for applications in biosensors field (Fig. 3.3 d).

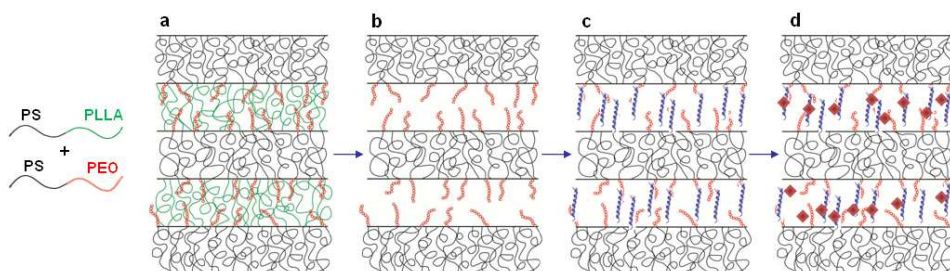


**Fig. 3.3** Strategy to obtain the functionalized nanoporous material; *a*) the starting material is a lamellar self-organised, multi-component composite (blend) containing two block copolymers: polystyrene-*block*-poly(L-lactide) (PS-*b*-PLLA) and polystyrene-*block*-poly(ethylene oxide) (PS-*b*-PEO); *b*) the selective removal of PLLA results in the formation of a nanoporous material that is patterned with nanometric channels containing pendant hydrophilic PEO chains; *c*) the porous material can be used to immobilize biomolecules; *d*) biomolecules are able to bind and recognize the analyte of interest.

The preparation and characterization of the nanoporous thin films are reported in paragraph 3.3. We have studied the physical absorption of different biomolecules on the designed nanoporous materials and we have compared the results with that obtained in the case of immobilization on flat and no porous supports. We have tested the myoglobin (Mb) protein (paragraph 3.4) and two enzymes, peroxidase from horseradish (HRP) (paragraph 3.5) and the esterase 2 (EST2) from *Alicyclobacillus acidocaldarius* (paragraph 3.6).

Immobilized hemoproteins (like Mb and HRP) are largely used in electrochemical [27] and optical sensing devices [28]. For electrochemical applications, direct electron transfer between hemoproteins and electrodes is accomplished by the incorporation of proteins into films (surfactant films, polyion-surfactant or clay-surfactant composite films, and amphiphilic polymers) [27 *b*], SP Sephadex [27 *c*] and gold nanoparticles [27 *d*]. Moreover, hemoproteins are also well known for their optical properties, which change during the binding of the corresponding ligands [28 *a*]. These optical characteristics can be exploited for the development of optical biosensors to detect dissolved oxygen (DO), nitric oxide (NO), and carbon monoxide (CO) [28 *b, c*].

The EST2 enzyme can act as active element in biosensors for the detection of specific organophosphate pesticides (OPs) [29]. In particular, EST2 have raised interest as part of biosensors in environmental monitoring because it is irreversibly inhibited by different OPs, like paraoxon, that is one of the most used pesticides in agriculture and also widely studied for its neurotoxic, cancerous, and teratogenic effects [30]. The inhibition mechanism will be described in paragraph 3.6. In the same paragraph, the optimization of the experimental conditions to physically absorb the enzyme EST2 on our nanoporous thin films is reported

together with some experiments for the determination of paraoxon by immobilized EST2.

The block copolymers based approach described in the present chapter for building nanoporous patterned surfaces is a robust and versatile tool useful not only in applicative research for fabrication of lab-on-chip biosensors, but also in basic research to study the adsorption mechanism of proteins in constrained environment with controlled geometry at fundamental level.

## 3.2 Materials and Methods

### 3.2.1 Materials

Polystyrene (PS), Polystyrene-*block*-poly(L-lactide) (PS-*b*-PLLA) and polystyrene-*block*-poly(ethylene oxide) (PS-*b*-PEO) with number average molecular mass ( $M_n$  in  $\text{Kg mol}^{-1}$ ) of 83.5, 21.0-24.3 and 22.0-21.5 and polydispersities of 1.05, 1.14 and 1.09, respectively, have been purchased from Polymer Source Inc. and used as received. Methanol (99.8%), sodium acetate (99.0%), sodium hydroxide (98%), hydrogen peroxide solution (Fluka,  $\geq 30\%$  RT), 2,2'-Azino-bis(3-ethylbenzothiazoline-6-sulfonic acid) diammonium salt (ABTS) (98.0%) and *p*-nitrophenyl butyrate (p-NPC4) ( $\geq 98\%$ ) have been purchased from Sigma-Aldrich. The proteins myoglobin from equine skeletal muscle (molecular weight  $17600 \text{ g mol}^{-1}$ , 95-100%, essentially salt-free, lyophilized powder) and peroxidase from horseradish (HRP) (total molecular mass  $44000 \text{ g mol}^{-1}$ , Type VI-A, essentially salt-free, lyophilized powder) have been also purchased from Sigma-Aldrich. All these products have been used without further purification. The enzyme esterase from *Alicyclobacillus acidocaldarius* (EST2) has been kindly provided by Dr. Manco's research group, Institute of Protein Biochemistry, National Research Council of Italy. The enzyme has been overexpressed in the mesophilic host *E. coli* strain BL21 (DE3) and purified as described in ref. 31. Silicon (100) supports (thickness  $525 \mu\text{m}$ ) have been purchased from Spi Supplies/Structure Probe Inc. The solvent 1,2-dichloroethane (99.8%) (DCE) and glass supports (size  $24 \times 24 \text{ mm}$  or  $10 \times 10 \text{ mm}$ , thickness  $0.13 \div 0.16 \text{ mm}$ ) have been purchased from Carlo

Erba Reagents. Silicon and glass supports have been cleaned with optical tissue and ethanol before use.

### 3.2.2 Preparation and characterization of the nanomaterials

*Preparation of thin films and PLLA hydrolysis.* Solutions of PS, PS-*b*-PLLA and mixtures of PS-*b*-PLLA and PS-*b*-PEO have been prepared dissolving the polymers in 1,2-dichloroethane to yield a total concentration of 0.5% and 1% (w/w) with respect to the solvent. In particular, the PS-*b*-PLLA/PS-*b*-PEO blend has been prepared through co-dissolution of the two block copolymers in the ratio 90/10 or 80/20 (w/w). Thin films have been obtained by drop casting or spin coating (RPM 3000 for 30 s) the polymers and blend solutions on silicon or glass supports. To improve the solid-state morphology, the films containing poly(L-lactide) (PLLA) have been recrystallized from melt on a hot bench at the maximum temperature of 200°C. The PLLA removal has been performed placing the thin films into a 0.5 M sodium hydroxide water/methanol (60:40 by volume) solution at 65°C for one minute (*etching* procedure). After removing from the solution, the films have been washed twice with a water/methanol (60:40 by volume) solution, and then dried at room temperature overnight.

*Directional eutectic solidification.* PS-*b*-PLLA and PS-*b*-PLLA/PS-*b*-PEO thin films have been prepared on glass slides by casting from a DCE solution (0.5 wt % of PS-*b*-PLLA or PS-*b*-PLLA+PS-*b*-PEO) at a temperature of around 40 °C. Hexamethylbenzene (HMB) in powder form has been then spread onto the polymer films and a nude glass coverslip has been placed on the so prepared samples to form a sandwich. The assembly has been heated at 180-200 °C; at this

temperature the molten HMB dissolves the block copolymer ( $T_m$  HMB = 168 °C;  $T_m$  PLLA = 170°C). The assembly has been then slowly cooled to room temperature on a hot plate. Crystallization of the HMB produces large, elongated crystals with the  $b$  axis parallel to the growth-front, and the concomitant crystallization of the PLLA. After cooling to room temperature, the glass slide and coverslip have been separated, and the crystalline HMB substrate have been removed by sublimation.

*Transmission and scanning electron microscopy.* Transmission electron microscopy (TEM) images have been obtained in bright field mode using a Philips EM 208S TEM with an accelerating voltage of 100 kV. For TEM characterization, the thin films have been backed with a carbon film, floated on water with the help of a poly(acrylic acid) backing, and mounted on copper grids. In order to achieve a good contrast between the different BCP domains, some films have been stained with RuO<sub>4</sub> by exposition of the TEM grids to RuO<sub>4</sub> vapors for 7 minutes at room temperature. Scanning electron microscopy (SEM) images of the blend PS- $b$ -PLLA/PS- $b$ -PEO 90/10 (w/w) have been performed on a Zeiss Ultra Plus field emission SEM (Centro de Apoyo Científico-Tecnológico, Universidade de Santiago de Compostela), equipped with a Inlens detector and a SE Everhart-Thornley Secondary Electron Detector, using accelerating voltages of 1.0 or 1.5 kV. The SEM image of the PS- $b$ -PLLA thin films and of the blend PS- $b$ -PLLA/PS- $b$ -PEO 80/20 (w/w) have been acquired with a FEI Nova NanoSEM 650.

*Thickness measurements.* The thickness of films has been measured with an Alpha-Step IQ Surface Profiler (KLA TENCOR) by performing at least 5 independent measurements in different regions of the same sample and over different samples. The relative error is less than 10%.

*Raman microspectroscopy.* Raman spectra have been acquired with a micro-Raman system Witec Alpha 300, endowed with a spectrometer equipped with two diffraction gratings (600 and 1800 g/mm). Backscattering collection and detection have been recorded, respectively, through a 60× dry objective and a CCD camera (1024 pixels) operating at -60 °C. The 532 nm line has been used as an excitation source for the Raman spectra. The exposure time is 5 s. Laser power at a sample surface is ca. 27 mW. The samples have been scanned at least in three different locations of the film.

*Contact angle measurements.* The optical contact angle (CA) measuring instrument to characterize the sample surfaces has been the OCA 20 from Data-Physics Instruments GmbH with SCA 20 software. The sessile drop method has been utilized, and the measurements have been taken at room temperature. The volume of the applied droplets of distilled water is 1.0  $\mu\text{L}$  (rate drop 0.5  $\mu\text{L s}^{-1}$ ). Contact angles have been measured on at least five independent locations of the samples surface and three different independent specimens. The contact angles have been computed using Laplace-Young fitting and the values measured on different locations of the sample surface and on different samples have been averaged.

### **3.2.3 Experiments of myoglobin adsorption**

All the samples for protein adsorption experiments have been prepared on a glass support.

For the adsorption isotherms, solutions of myoglobin in water at different concentrations (8.62, 5.35, 3.44 and 2.22 mg/L) have been prepared. A 500  $\mu\text{L}$  aliquot of the protein solutions has been deposited on

our nanoporous film surface and incubated for a fixed time (30 minutes). During the incubation time the samples have been placed on an oscillating stirrer at the temperature of 10 °C, to avoid the protein solution evaporation. After 30 minutes, the protein solution used for incubation has been removed from films and the myoglobin concentration of recovered solution has been determined by UV-Vis spectrometer. In particular, the concentration of myoglobin have been determined by UV-Vis adsorption measurements a 408 nm using a molar extinction coefficient value of  $188000 \text{ M}^{-1} \text{ cm}^{-1}$  [32]. The amount of adsorbed myoglobin on our nanoporous films has been estimated from the difference in the myoglobin concentration in the recovered solutions and in the solutions initially deposited on the films. The samples have been rinsed one time with distilled water to remove protein molecules that are eventually weakly adsorbed on the surface. The absence of protein in the rinsing water has been confirmed by UV-Vis spectroscopy and HPLC. The same experiments have been also performed on PS films and bare glass supports to compare the protein adsorption capacity of the different supports.

For myoglobin adsorption kinetics experiments, 750  $\mu\text{L}$  aliquot of solutions of myoglobin with a fixed concentration (7.95, 6.39, 4.03 or 3,75 mg/L) have been placed on the etched blend films and recovered after different incubation times (from 5 to 75 minutes). The amount of the absorbed myoglobin at each incubation time has been determined by UV-visible spectrometer with the same procedure described above. All the myoglobin adsorption kinetics experiments have been performed at 5 °C. The adsorption kinetics experiments using myoglobin solutions of 7.95 and 4.03 mg/L have been performed also on a PS thin films.

All UV-Vis spectra have been recorded with a Cary 60 UV-Vis spectrophotometer equipped with a Cary single cell Peltier accessory (Agilent Technologies). The concentration of myoglobin has been determined by UV-Vis adsorption measurements at 25 °C using molar extinction coefficient values of  $188000 \text{ M}^{-1} \text{ cm}^{-1}$  ( $\epsilon_{408\text{nm}}$ ) [32]. The cell with 1.0 cm path length has been used to record UV-Vis spectra between 250 and 800 nm. The scan of distilled water has been subtracted from the scan of each sample.

### **3.2.4 Experiments of peroxidase activity**

*Step 1. Enzyme immobilization.* The enzyme peroxidase from horseradish (HRP) has been physically adsorbed on our nanostructured films with a procedure similar to that described above for the myoglobin. In particular, HRP has been dissolved in distilled water at a concentration of 18 mg/L. A 500  $\mu\text{L}$  aliquot of the enzyme solution has been deposited to the our nanoporous film surface and incubated. During the incubation time, the samples have been placed on an oscillating stirrer at 10 °C. Then, the enzyme solution has been removed from films and the samples have been rinsed with distilled water to remove enzyme molecules that are weakly adsorbed on the surface. Experiments have been performed varying the time of contact between the enzyme solutions and our surfaces. In particular, we have used three different incubation times (30, 90 and 150 min).

*Step 2. Test activity of immobilized HRP.* The ability of adsorbed HRP to catalyze one-electron oxidation by  $\text{H}_2\text{O}_2$  of the dye 2,2'-Azino-bis(3-ethylbenzothiazoline-6-sulfonic acid) diammonium salt (ABTS)

into the corresponding radical cation  $\text{ABTS}^{\cdot+}$  has been tested. For this purpose, a solution of ABTS (2.45 mM) has been prepared in a 50mM phosphate buffer at pH 4.6. Few microliters of aqueous hydrogen peroxide has been added to the solution at a concentration of 9.75 mM. A 500  $\mu\text{L}$  aliquot of the so prepared solution containing ABTS and  $\text{H}_2\text{O}_2$  has been deposited on our nanostructured films with absorbed HRP. We have determined the amount of the formed radical cation  $\text{ABTS}^{\cdot+}$  ( $\lambda_{\text{max}} = 420 \text{ nm}$ ) recording the UV-Vis spectra of these solutions after 5 minutes of contact with the immobilized enzyme.

To evaluate the stability of the immobilized enzyme over the time, we have also performed enzymatic activity tests after 7 and 18 days from immobilization. During this time the samples have been dry stored at  $4^\circ\text{C}$  without particular precautions.

The same experiments have been conducted also on PS films and bare glass supports to compare the catalytic performance of HRP absorbed on the different supports.

All UV-Vis spectra have been recorded with a Cary 60 UV-Vis spectrophotometer equipped with a Cary single cell Peltier accessory (Agilent Technologies). The concentration of HRP has been determined by UV-Vis adsorption measurements at  $25^\circ\text{C}$  using molar extinction coefficient values of  $1 \times 10^5 \text{ M}^{-1} \text{ cm}^{-1}$  ( $\epsilon_{403\text{nm}}$ ) [33]. The cell with 1.0 cm path length has been used to record UV-Vis spectra between 250 and 800 nm. The scan of distilled water has been subtracted from the scan of each sample. Also, the formation of radical cation  $\text{ABTS}^{\cdot+}$  has been monitored by UV-Vis measurements ( $\epsilon_{420 \text{ nm}} = 3.6 \times 10^5 \text{ M}^{-1} \text{ cm}^{-1}$ ) [34]. In this case, a cell with 0.1 cm path length has been used to record UV-Vis spectra in the range 400-800 nm. A scan speed of 600 nm/min has been used to acquire the data.

### 3.2.5 Experiments of esterase 2 activity

#### a) Activity of immobilized esterase 2 (EST2)

*Step 1. Enzyme immobilization.* The EST2 enzyme has been dissolved in 25 mM HEPES buffer, pH 7.1, at a concentration of 0.3  $\mu$ M. The enzyme has been physically absorbed on our porous nanostructured films (etched blend) and on glass slides by placing 110  $\mu$ L of the EST2 solution on the surfaces (size 10 mm x 10 mm) for fixed incubation times. In particular, incubation times of 90 min and 2, 3 and 6 days have been used. During the incubation times, the samples have been placed, at room temperature, under atmosphere with a controlled humidity (80%). The humidity has been controlled by placing the samples in a close container containing a KCl saturated solution. The controlled humidity avoids the complete drying of the enzyme solutions in the case of long incubation times, favoring the enzyme diffusion in the nanopores of the etched blend. After the incubation time, the samples have been rinsed with 25 mM HEPES buffer (pH 7.1) to remove enzyme molecules that are weakly adsorbed on the surface.

*Step 2. Test activity of immobilized EST2.* The ability of absorbed EST2 to catalyze the hydrolysis of the substrate *p*-nitrophenyl butyrate (*p*-NP-C4) has been tested by monitoring, using a plate reader, the increase of absorbance at 405 nm due to the released *p*-nitrophenol (*p*-NP) (Fig. 3.23). For this purpose, the samples containing the immobilized EST2 (dimensions 10 x 10 mm) have been placed in the wells (diameter ~ 15 mm) of a 24-well plate. A solution of *p*-NP-C4 (20  $\mu$ M) has been prepared in 25 mM HEPES buffer, pH 7.1, 4% (v/v) acetonitrile and a 1 mL aliquot of the so prepared solution has been deposited in each well

containing the surfaces with immobilized EST2. The absorbance at 405 nm has been recorded every 110 s. During the experiments the plate reader has been kept under stirring between consecutive absorbance measurements.

*b) EST2 residual activity after contact with paraoxon*

*Step 1.* The EST2 enzyme has been physically absorbed on our porous nanostructured films (etched blend), on PS thin films and on glass slides, by using the same procedure described in the step 1 of the paragraph 3.2.5. For this set of experiments, the EST2 enzyme has been dissolved in 20 mM phosphate buffer, pH 7.1, at concentration of 0.5  $\mu$ . An incubation time of 6 days has been used during the immobilization step.

*Step 2.* Paraoxon solutions at different concentrations (range 0.02 - 0.5  $\mu$ M) have been prepared in 20 mM phosphate buffer (pH 7.1). 110  $\mu$ L of the so prepared paraoxon solutions have been placed on the different surfaces containing the immobilized EST2. The samples have been placed on an oscillating stirrer for 20 h. During this step the paraoxon covalently links to the active site of the immobilized enzyme. After that, the samples have been rinsed with water in order to ensure the removal of paraoxon molecules that are not covalently linked to the enzyme.

*Step 3.* The EST2 activity has been tested using *p*-NP-C4 as substrate, adopting the same procedure described in step 2 of the paragraph 3.2.5. In this case the kinetic of the reaction has been followed by measuring the absorbance at 405 nm every 130 s.

### 3.3 Preparation and characterization of the nanoporous material

*a) Preparation of PS-*b*-PLLA and PS-*b*-PLLA/PS-*b*-PEO thin films (step a of Fig. 3.3)*

We have used a polystyrene-*block*-poly(L-lactide) (PS-*b*-PLLA) block copolymer with molecular masses  $M_n$  of PS and PLLA equal to 21.0 and 24.3 Kg mol<sup>-1</sup>, respectively, and polydispersity index  $M_w/M_n = 1.05$ . The volume fraction of the PS block of 0.53 has been selected to 0.53 in order to obtain a lamellar phase-separated morphology. Thin films of PS-*b*-PLLA have been prepared by drop casting or spin coating dilute solutions of PS-*b*-PLLA in 1,2-dichloroethane (concentration of 0.5% and 1% w/w with respect to the solvent). Representative bright-field TEM and SEM images of the so obtained thin films are reported in figure 3.4A and A', respectively.

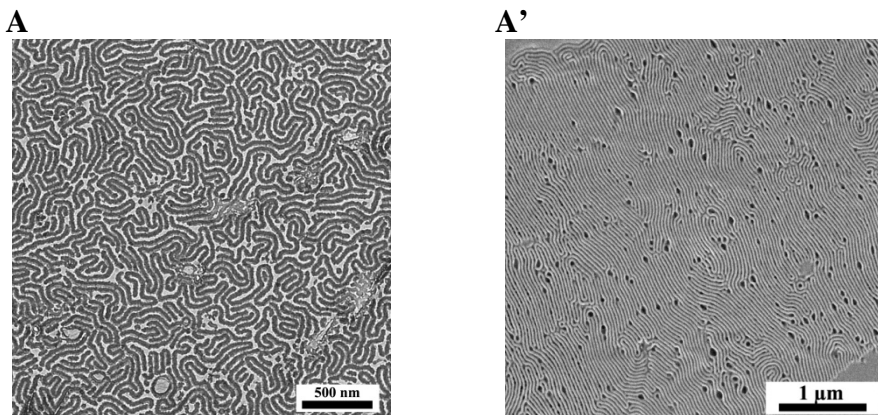


**Fig. 3.4** Bright-field TEM (A) and SEM (A') image of a PS-*b*-PLLA thin film. The film in (A) has been prepared by drop casting a solution (0.5 wt% in DCE) of PS-*b*-PLLA on a glass slide, then the film has been transferred on a TEM grid and stained with RuO<sub>4</sub> before observation. The film in (A') has been prepared by spin coating a solution (1wt% in DCE) of PS-*b*-PLLA (A') on a silicon wafer. The typical thickness of these films is 80-110 nm.

The images correspond to a well-defined disordered lamellar morphology. In the TEM image (Fig. 3.4 A) contrast is provided by staining with  $\text{RuO}_4$ , which selectively marks the aromatic rings in the polystyrene blocks. For this reason, the dark regions correspond to stained PS lamellar nanodomains and the bright regions to the PLLA phase. In contrast, the PS domains appear bright in the SEM image (Fig. 3.4 A'). The average lamellar spacing is estimated to be  $\approx 28 \pm 3$  and  $\approx 20 \pm 3$  nm for PS and PLLA, respectively.

In order to obtain a functionalized and more hydrophilic nanomaterial, PS-*b*-PLLA has been blended with a polystyrene-*block*-poly(ethylene oxide) (PS-*b*-PEO) copolymer ( $M_n$  22.0-21.5 Kg mol<sup>-1</sup>,  $M_w/M_n = 1.14$ ). PS-*b*-PEO has been selected due to the presence of the protein-compatible poly(ethylene oxide) block; the PEO microdomains may provide hydrophilic microenvironment able to facilitate proteins adsorption and to maintain their functions. Moreover, the -OH terminals of PEO blocks can provide suitable sites to covalently link biomolecules in the final material. The PS-*b*-PLLA/PS-*b*-PEO blend has been prepared by dissolving in 1,2-dichloroethane the two block copolymers to yield a total concentration of 0.5% or 1% (w/w) with respect to the solvent. Thin films have been obtained by drop casting or spin coating the blend solutions (step a in Fig. 3.1). Representative bright-field TEM and SEM images of thin films of the blend are reported in figure 3.5. In order to control the final hydrophilicity of the material, we have employed two different PS-*b*-PLLA/PS-*b*-PEO ratios, 90/10 w/w (A, A') and 80/20 w/w (B, B').

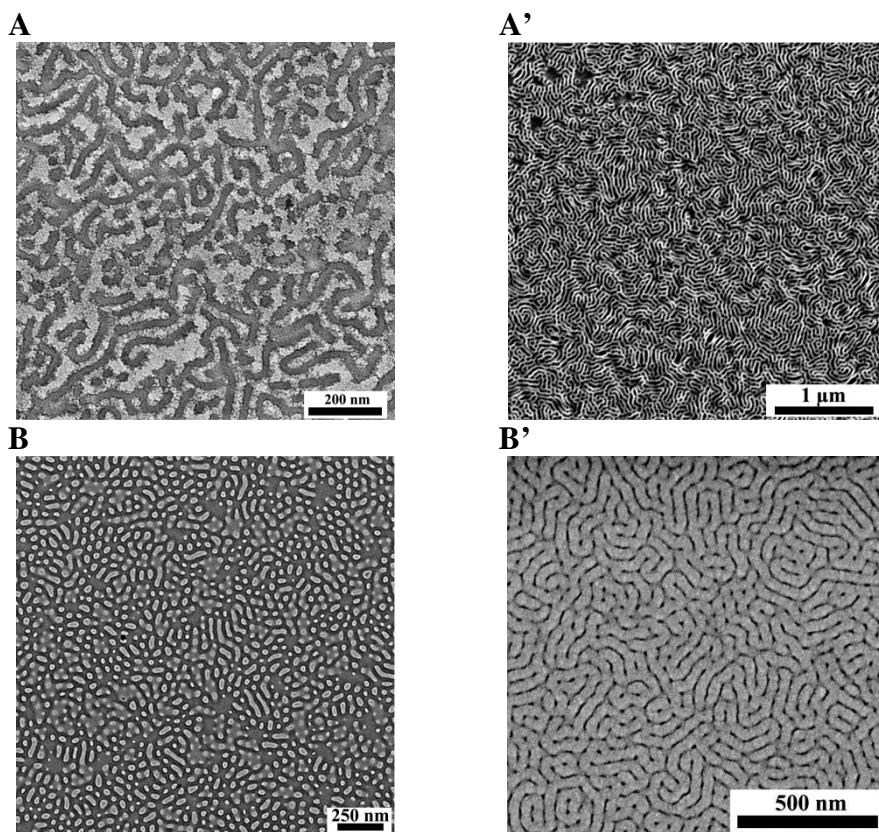


**Fig. 3.5** Bright-field TEM (**A**, **B**) and SEM (**A'**, **B'**) images of thin films of the blend PS-*b*-PLLA/PS-*b*-PEO with 10 (**A**, **A'**) and 20 (**B**, **B'**) wt% PS-*b*-PEO at different magnifications. The films have been prepared from a DCE solution of PS-*b*-PLLA/PS-*b*-PEO 90/10 w/w (**A**, **A'**) or 80/20 w/w (**B**, **B'**). The TEM grids have been stained with RuO<sub>4</sub> before observation.

There are no significant differences in morphology compared to the thin films of neat PS-*b*-PLLA (Fig. 3.4). The addition of the PS-*b*-PEO block copolymer does not alter the lamellar morphology. A well-defined phase separation with a disordered lamellar morphology is observed also in the case of the blend PS-*b*-PLLA/PS-*b*-PEO. Moreover, also in this case, in the TEM image (Fig. 3.5 **A** and **B**) the contrast is provided by staining with RuO<sub>4</sub> in order to mark selectively the PS lamellar nanodomains. In the TEM images (Fig. 3.5 **A**, **B**), due to the partial miscibility of PEO and PLLA [26], it is reasonable to suppose that the bright lamellar domains

correspond to mixed PEO and PLLA component. The average lamellar spacing of PS and PEO/PLLA domains is estimated to be similar to that observed in neat PS-*b*-PLLA thin films. No significant differences in morphology and lamellar spacing are observed in thin films obtained by solutions of the blend containing lower (Fig. 3.5 A, A') or higher (Fig. 3.5 B, B') amount of PS-*b*-PEO. In the case of the TEM image of the blend with higher amount of PS-*b*-PEO (Fig. 3.5 B), the lamellar morphology is less defined, presenting dot-like entities, probably due to the complex protocol in TEM grids preparation. In particular, since the thin films are floated on water in order to facilitate the fishing with a grid, in the case of the sample with 20 wt% PS-*b*-PEO the higher hydrophilicity alters in somehow the lamellar morphology that is instead kept in the sample used for SEM observation.

*b) Obtainment of ordered nanostructures by directional eutectic solidification*

As discussed in paragraph 1.3, the spatial and orientational control of BCP nanodomains is necessary for specific potential applications of BCPs. Our PS-*b*-PLLA and PS-*b*-PLLA/PS-*b*-PEO thin films (Fig. 3.4 and 3.5) are very interesting due to the possibility to induce long-range alignment of the lamellar nanostructures by directional eutectic solidification. This technique has been described in paragraph 1.3.2.

In figure 3.6 TEM images of PS-*b*-PLLA (A) and of the blend PS-*b*-PLLA/PS-*b*-PEO (B) thin films after directional eutectic solidification with hexamethylbenzene (HMB) are reported.

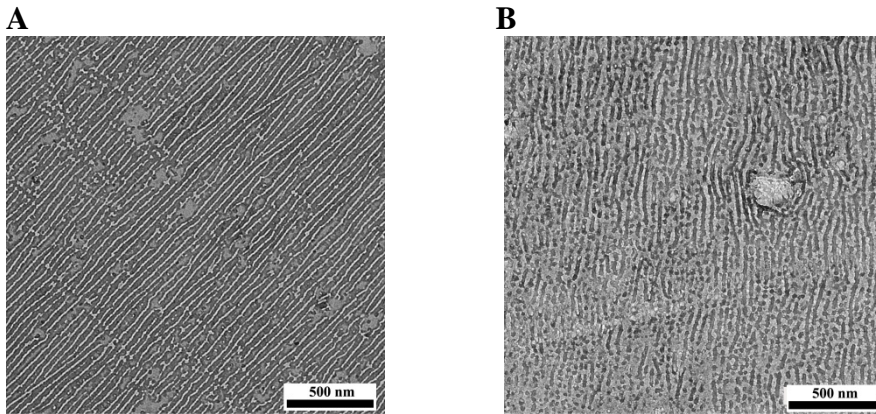


**Fig. 3.6** Bright-field TEM images of PS-*b*-PLLA (**A**) and of the blend PS-*b*-PLLA/PS-*b*-PEO (**B**) thin films obtained by directional solidification with HMB. 7 min RuO<sub>4</sub> staining has been applied before TEM observation. The TEM images of the same samples with no directional solidification with HMB are reported in figures 3.4 A and 3.5A.

Large-sized, well-oriented lamellar microstructures can be observed for both samples. In particular ordered lamellar nanodomains of PS (dark in the images) alternate to ordered lamellar nanodomains of PLLA (A) or PLLA/PEO (B) blocks. The procedure employed to prepare the samples has been described in paragraph 3.2.2. Briefly, when the molten assembly of block copolymers and HMB is cooled to room temperature, crystallization of HMB produced large, elongated crystals with the *b* axis parallel to the growth-front, with concomitant crystallization of the PLLA. The PLLA solidification in contact with the pre-existing oriented HMB crystals produces the microstructure orientation over the whole contact area with HMB. The average lamellar spacing is  $\approx 29 \pm 3$  and  $\approx 18 \pm 2$  nm for PS and PLLA, respectively. The same values were found in the case of the disordered thin film (with no directional solidification with HMB) (Fig. 3.4 A).

*c) Obtainment of the nanoporous material by selective removal of PLLA blocks (step of Fig. 3.3)*

Thin films of the blend (Fig. 3.5) have been immersed into a 0.5 M sodium hydroxide water/methanol solution at 65°C for one minute to remove the poly(L-lactide) blocks. We name the above treatment *etching* and the so treated films are indicated as *etched*. During the basic hydrolysis treatment the temperature has been deliberately held just above the  $T_g$  of PLLA. SEM images of the etched blends are reported in figure 3.7. The images are tilted in order to better visualize the pores. The samples have been obtained after the PLLA removal from the blend thin films containing 10 (A) and 20 (B) wt% PS-*b*-PEO copolymer. The etching treatment does not alter the initial lamellar morphology, as we can see by the comparison with the SEM images of the same samples before the etching treatment (Fig. 3.5 A' and B'). The etching treatment results in porous thin films with nanochannels of width 20 nm delimited by PS lamellar domains containing functional hydrophilic PEO walls (Fig. 3.7).

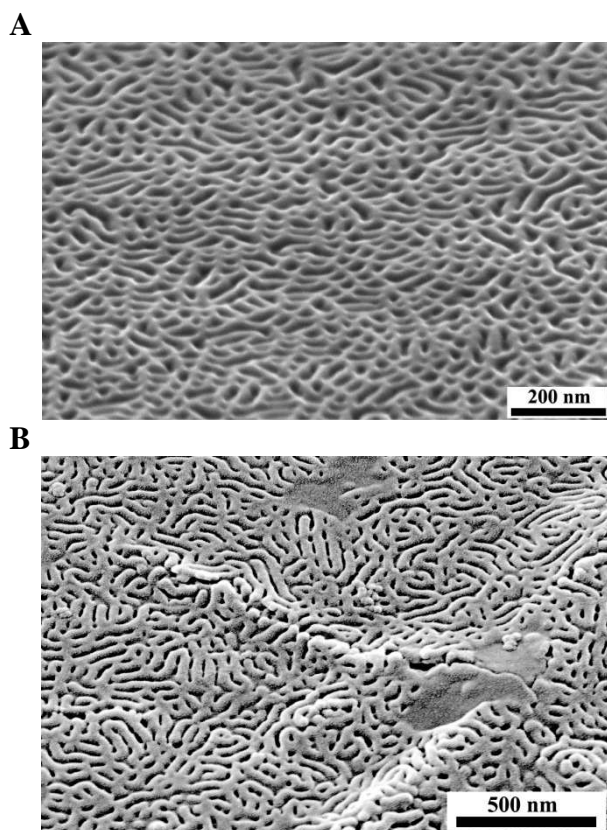


**Fig. 3.7** Tilted SEM images of etched blends thin films containing 10 (**A**) and 20 (**B**) wt% PS-*b*-PEO. The porous thin films have been obtained by immersion of the blends thin films, prepared from DCE solutions of PS-*b*-PLLA/PS-*b*-PEO 90/10 (**A**) and 80/20 w/w (**B**), into a basic solution to selectively remove PLLA blocks. Tilt angles: 66° (**A**) and 40° (**B**).

The thin film of the etched blend has been also examined by TEM *without any staining procedure* with RuO<sub>4</sub> (Fig. 3.8A). A remarkable contrast is present in the TEM micrographs of the etched film without any chemical staining demonstrating the effective removal of the PLLA blocks and consequent formation of nanopores. The contrast in the image of the Fig. 3.8A is pronounced as in the case of the stained film (Fig. 3.5 A, B), demonstrating that the PLLA blocks have been removed, making the channels where the electron beam is freely transmitted regions with minimal scattering and/or adsorption. No contrast, in fact, is obtained

when we analyze a blend film before the removal of PLLA without resorting to a staining procedure (Fig. 3.8 B).

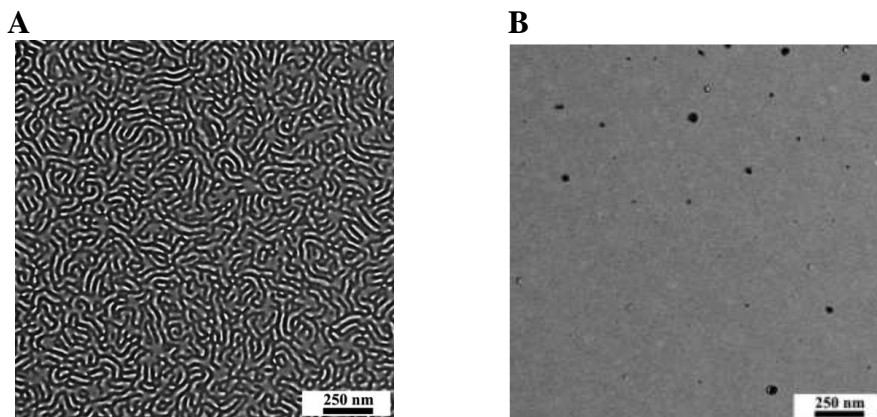


**Fig. 3.8** Bright-field TEM image of a thin film of the etched blend (A). The thin films have been prepared by spin coating a solution (0.5wt% in DCE) of PS-*b*-PLLA and PS-*b*-PEO (90/10 w/w) and then immersed into a basic solution to selectively remove PLLA blocks. No staining procedure has been employed on the film before of the TEM observation. TEM image of the blend thin film before etching procedure, without staining.

It is worth noting that the etching treatment performed on the neat PS-*b*-PLLA thin films results in a remarkable breaking of the initial lamellar morphology (Figure A3.1 in appendix).

The removal of PLLA blocks after etching has been also confirmed by Raman measurements. In figure 3.9 A the Raman spectra, acquired in the range  $750\text{-}1800\text{ cm}^{-1}$ , of a blend thin film before (curve a of Fig. 3.9 A) and after (curve b of Fig. 3.9 B) the etching procedure are reported. The main bands of polystyrene are located at  $1000\text{ cm}^{-1}$  (C-C ring breathing mode),  $1034\text{ cm}^{-1}$  and  $1602\text{ cm}^{-1}$  (tangential ring stretching mode). These bands are the most intense signals appearing in the Raman spectra. As expected, the PS signals are present in both the spectra of the etched and non etched blend.

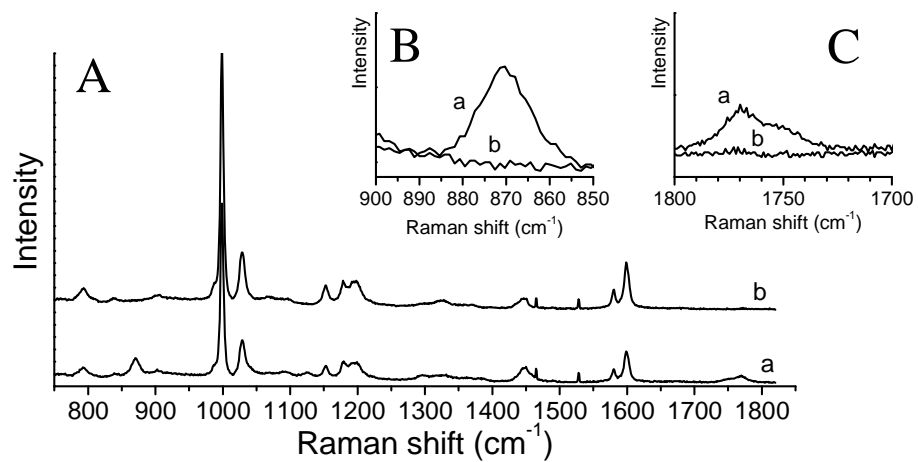


**Fig. 3.9** Raman spectra of a thin film of the blend PS-*b*-PLLA/PS-*b*-PEO before (*a*) and after (*b*) etching procedure in the range 750-1800 cm<sup>-1</sup> (A). Zooms of the region 900-850 cm<sup>-1</sup> and 1800-1700 cm<sup>-1</sup> are reported in B and C, respectively.

The relevant PLLA bands appear at 870 and 1770  $\text{cm}^{-1}$  and are attributed to the C-COO and C=O stretching mode, respectively. In Fig. 3.9 B and C, zooms of the regions 900-850  $\text{cm}^{-1}$  and 1800-1700  $\text{cm}^{-1}$  are reported. The PLLA signals are present in the spectrum of the blend before etching (curves a of Fig. 3.9) and disappear after the etching procedure (curves b of Fig. 3.9), confirming the removal of PLLA blocks.

Quartz microbalance measurements (QCM) indicate that  $\sim 70\%$  of the initially present PLLA is removed by etching treatment.

The wettability is an important factor for the adsorption of biomolecules on the surfaces from aqueous solutions. Hydrophobic surfaces have scarce affinity with water making the process of protein adsorption difficult for biomolecules dissolved in water. We have investigated the wettability of the thin films through the measurement of the contact angle (CA) of a water droplet placed on the surfaces (Figure 3.10). Representative images of the profile of 1 $\mu\text{L}$  water droplets placed on films of PEO (Fig. 3.10 A), PS-*b*-PLLA before (Fig. 3.10 B) and after etching (Fig. 3.10 D - D''), and blends before (Fig. 3.10 C) and after etching (Fig. 3.10 E - E'') are reported. It is apparent that the water droplets have different shapes on the different surfaces due to the different degree of hydrophilicity of the thin films. We notice that water droplets are almost flat on PEO (Fig. 3.10 A) and rather rounded in the case of films before etching (Fig. 3.10 B, C). Moreover the water droplets appear to have a shape in between in the case of the etched films (Fig. 3.10 D - D'' and E - E''). The average values of the contact angle (CA) measured on at least 5 independent locations of the sample surface and three different independent specimens are reported in Table 3.1.

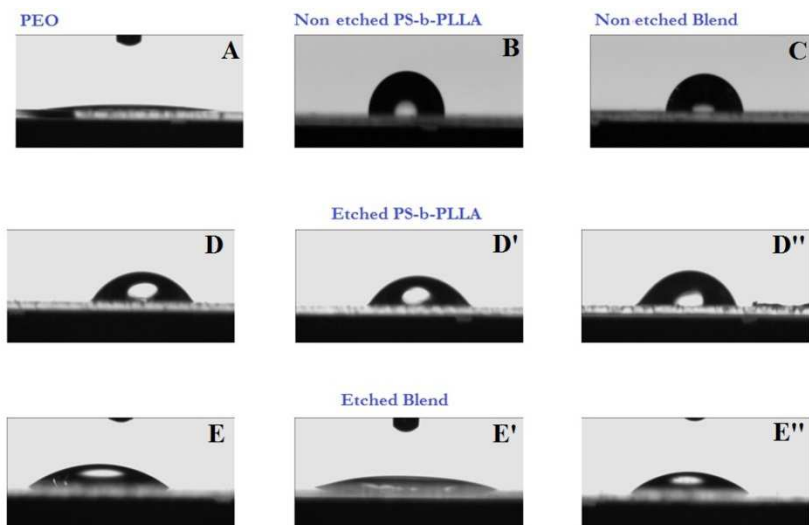


**Fig. 3.10** Images of the profile of 1µL water droplets on a thin film of PEO (A), non etched PS-*b*-PLLA (B), non etched blend (C), etched PS-*b*-PLLA (D - D'') and etched blend (E - E''). The images D - D'' and E - E'' are acquired in different locations of the films. The films have been prepared by spin coating on a glass slide 1 wt% solutions of PEO, PS-*b*-PLLA and blend PS-*b*-PLLA/PS-*b*-PEO (90/10 w/w) in DCE. The PLLA has been removed by basic hydrolysis as previously described.

**Table 3.1** Contact angle (CA) values determined on the various thin films using Laplace-Young approach.

Sample	<CA>
No etched PS- <i>b</i> -PLLA	93° ± 0.1
No etched Blend	84° ± 0.1
Etched PS- <i>b</i> -PLLA	62° ± 0.3
Etched Blend	28° ± 0.2
PEO	6°

As expectable, non etched PS-*b*-PLLA film (Fig. 3.10 B) shows an hydrophobic surface with a CA value of 93° ± 0.1. Introducing the PS-*b*-PEO copolymer in the film, the CA value slightly decreases to 84° ± 0.1, due to the hydrophilicity of PEO blocks (Fig. 3.10 C). The etched PS-*b*-PLLA film (Fig. 3.10 D – D'') exhibits a CA of 62° ± 0.3, confirming the selective removal of PLLA. Notably, the CA value in the case of our nanoporous material (Fig. 3.10 E - E'') of 28° ± 0.2 is lower than those of

both the non etched samples and the etched PS-*b*-PLLA. This indicates that upon PLLA removal our porous materials become hydrophilic due to the presence of PEO blocks pendants in the pore volume. The incorporation of PEO polyether into the pore space dramatically influences the wettability of the resulting nanoporous material. It is expected that this characteristic of our material strongly affects the adsorption of biomolecules from aqueous solutions, as shown in the next paragraphs. Furthermore, as previously shown (Fig. 3.5 B, B' and Fig. 3.7 B), we have been also able to prepare thin films of the blend containing different amount of the hydrophilic PEO blocks, demonstrating the possibility to control the hydrophilicity of our porous materials by simply changing the initial composition of the blends. Therefore, using our protocol, porous materials of tailored pore size and hydrophilicity can be easily prepared with high level of reproducibility.

### 3.4 Experiments of myoglobin adsorption

This paragraph is focused on the study of our porous material as support for the physical immobilization of myoglobin (Mb). Mb is a small heme protein with a molecular weight of 17600 Da and molecular dimensions of 4.5 nm × 3.5 nm × 2.5 nm [35 *a, b*]. It contains a single polypeptide chain of 153 amino acid residues of known sequence and a single iron protoporphrin IX as prosthetic group in a hydrophobic pocket [35 *c, d*]. Myoglobin belongs to the globin superfamily of proteins, and as with other globins, consists of eight alpha helices connected by loops (Fig. 3.11). As discussed in paragraph 3.1.3, immobilized hemoproteins, like Mb and horseradish peroxidase (HRP), are largely used in electrochemical [27] and optical sensing devices [28].

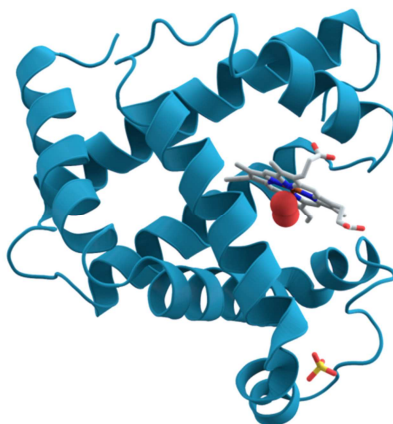


**Fig. 3.11** Overall fold of myoglobin. The prosthetic group is also reported [35 *d*].

The experiments of myoglobin adsorption on the different surfaces have been conducted by placing water Mb solutions on the top of the surfaces for a certain incubation time. Then, the protein solutions have been removed from surfaces and the amount of myoglobin adsorbed has been estimated from the differences in protein concentration in the

solutions before and after adsorption, measured by UV-vis spectroscopy at 408 nm, according to the equation 3.1.

$$\Gamma = \frac{V_0(C_0 - C)}{A} \quad (\text{Eq. 3.1})$$

where  $\Gamma$  is the adsorbed amount of protein per unit surface area (surface density coverage),  $C_0$  is the myoglobin concentration in the initial solution,  $C$  is the myoglobin concentration in the solution after any selected incubation time,  $V_0$  is the volume of the initial protein solution and  $A$  is the area of the solid surface equal to  $576 \text{ mm}^2 (= 24^2 \text{ mm}^2)$  and corresponding to the area of the glass support. Indeed we have checked that the glass support is uniformly covered by the polymer (PS) and BCP thin films, taking SEM images of different quadrants of the glass specimens in regions both close to the boundaries and in the center.

Experiments have been carried out on our porous support (etched blend), on non porous thin films (PS) and on flat surfaces (glass slides).

We have performed different experiments by changing both the concentration of the initial Mb solutions and the incubation time (time of contact between the myoglobin solutions and the different surfaces).

Figure 3.12 shows the isotherms of myoglobin adsorption on the etched blend (curves a, a' of Fig. 3.12), a PS thin film (curve b of Fig. 3.12) and a glass slide (curve c of Fig. 3.12), obtained fixing the incubation time to 30 minutes at the temperature of  $10 \text{ }^\circ\text{C}$ , using myoglobin solutions of different initial concentration ( $C_{in}$ ). The corresponding values of surface density coverage ( $\Gamma$ ) are reported in Table 3.2. It is worth noting that the adsorption isotherm of Fig. 3.12 determined by fixing the incubation time to 30 min is well representative

of adsorption behavior of our blend, as demonstrated by adsorption kinetics experiments of Fig.3.13 (*vide infra*).

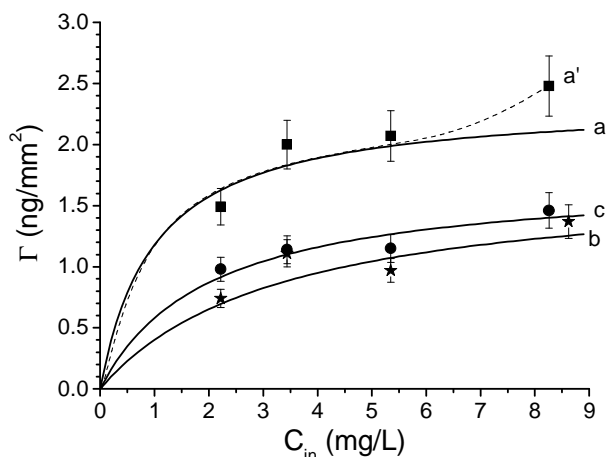


**Fig. 3.12** Myoglobin adsorption isotherms on a thin film of the etched blend (*a*, *a'*, ■), a PS thin film (*b*, ★) and a glass slide (*c*, ●). The initial concentrations of the myoglobin solutions are 2.22, 3.44, 5.35 and 8.62 mg/L.  $\Gamma$  is the surface density coverage calculated with Eq. 3.1. Incubation is performed for 30 min, at 10°C. The solid lines *a*, *b* and *c* are the fit to the data with the Langmuir equation (Eq. 3.2). The solid line *a'* shows the deviation from the Langmuir fit in the case of the etched blend.

It is worth noting that the surface density coverage of myoglobin ( $\Gamma$ ) in the case of our nanoporous surface (curves *a*, *a'* of Fig. 3.12) is higher than both the PS thin film (curve *b* of Fig. 3.12) and the glass slide (curve *c* of Fig. 3.12), for all the examined Mb initial concentrations ( $C_{in}$ ). The myoglobin amounts adsorbed on the PS thin film and the glass slide are similar each other (curves *b* and *c* of Fig. 3.12).

We have found that the amount of adsorbed protein increases with increasing the protein concentration in the initial solutions. This can be explained by the existence of the concentration dependent process named “spreading”. The area which a protein occupies on the adsorbent surface is called the footprint of the protein. Usually, the footprint increases with the residence time of the protein on the sorbent. This process is called spreading. The spreading process is influenced by the protein and surface

properties as by the presence of neighboring molecules. At high concentrations of the initial solution, the surface will be occupied in a shorter time and so the time for spreading will be shorter. This results in a smaller average footprint of protein molecules. As a consequence, the adsorbed concentration will be larger. In other words, when the supply rate is high (higher protein concentration in the initial solution) the time for spreading is small. As a consequence, more protein can be adsorbed. This explains why the protein density on the surface increases with the initial concentration of the protein in the solution.

**Table 3.2** Surface density coverage of myoglobin ( $\Gamma$ ) on the etched blend, the PS thin film and a glass slide for different initial concentrations of the protein in the solutions ( $C_{in}$ ) at 30 min. Monolayer adsorption density ( $\Gamma_m$ ) and Langmuir binding constant ( $K$ ) calculated by fitting the adsorption isotherms with Eq. 3.2.

	$\Gamma$ (ng/mm <sup>2</sup> ) <sup>(a)</sup>				$\Gamma_m$ (ng/mm <sup>2</sup> ) <sup>(b)</sup>	$n_{Mb}$ (units/nm <sup>2</sup> ) <sup>(c)</sup>	$K$ <sup>(b)</sup>
	$C_{in}$ 2.22 (mg/L)	$C_{in}$ 3.44 (mg/L)	$C_{in}$ 5.35 (mg/L)	$C_{in}$ 8.62 (mg/L)			
<b>Etched Blend</b>	1.5 ± 0.1	2.0 ± 0.2	2.1 ± 0.2	2.5 ± 0.2	2.7 ± 0.2	(9.2 ± 0.7) 10 <sup>-2</sup>	1.0 ± 0.5
<b>PS</b>	0.7 ± 0.1	1.1 ± 0.1	1.0 ± 0.1	1.4 ± 0.1	1.7 ± 0.5	(5.8 ± 0.2) 10 <sup>-2</sup>	0.3 ± 0.2
<b>Glass slide</b>	1.0 ± 0.1	1.1 ± 0.1	1.1 ± 0.1	1.4 ± 0.1	1.7 ± 0.2	(5.8 ± 0.1) 10 <sup>-2</sup>	0.5 ± 0.2

(a) Maximum relative errors calculated considering an error of 10% in the volumes of the retrieved Mb solutions.

(b) Absolute errors calculated by propagation of the maximum error. Results are averaged over at least three independent experiments.

(c) Number of protein molecules per nm<sup>2</sup> calculated as  $\frac{\Gamma_m 10^{-21} N_A}{17600}$ , with 17600 the molecular mass of myoglobin and  $N_A$  the Avogadro number.

All isotherms in Fig. 3.12 show an initial increase and then reach a plateau. In the hypothesis that under the experimental conditions the proteins form a monolayer, the presence of a plateau suggests that these isotherms can be fitted to the Langmuir isotherm equation (Eq. 3.2).

$$\frac{\Gamma}{\Gamma_m} = \frac{KC}{1+KC} \quad (\text{Eq. 3.2})$$

where  $\Gamma$  is the protein surface density coverage,  $\Gamma_m$  is the maximum value of protein surface density coverage (full coverage of surface, or monolayer adsorption density) and indicates the monolayer adsorption ability on the surface,  $C$  is the protein concentration,  $K$  is the adsorption-to-desorption ratio, or Langmuir binding constant for the adsorption process.

The values of the monolayer adsorption density ( $\Gamma_m$ ) and of the Langmuir binding constant ( $K$ ) calculated by fitting the adsorption isotherms with Eq. (3.2) are reported in table 3.2. From the calculated  $\Gamma_m$  and  $K$  values it is evident that our porous support is a better candidate for biomolecule adsorption than the PS thin film and the glass slide. In particular, the number of myoglobin biomolecules adsorbed per  $\text{nm}^2$  on our supports ( $n_{\text{Mb}}$ , see table 3.2) is  $\sim 9 \times 10^{-2}$  units/ $\text{nm}^2$  in the case of the nanoporous support (etched blend) and  $n_{\text{Mb}} \sim 6 \times 10^{-2}$  units/ $\text{nm}^2$  in the case of non porous supports (PS and glass), corresponding to a single Mb biomolecule adsorbed on an area  $A$  of  $\sim 11 \text{ nm}^2$  in the case of the porous support and  $\sim 17 \text{ nm}^2$  in the case of the non porous supports. This is due to the large surface area and opened pore structure that allows high protein loadings in the case of the etched blend. The results that our support exhibits an increased adsorption ability with respect to both a flat and hydrophilic surface (glass slide) and a flat and hydrophobic surface

(PS) indicates the importance of the nanochannels and of their hydrophilic nature due to the PEO presence.

It is worth noting that in the case of our porous surface (curves a, a' of Fig. 3.12) a deviation from the Langmuir fit (curve a of Fig. 3.12) is observed (curve a' of Fig. 3.12) [36].

To further evaluate the ability of our nanoporous support to absorb the myoglobin we have performed adsorption kinetics experiments (Figure 3.13). To this aim 750  $\mu\text{L}$  of myoglobin solutions with a fixed concentration (7.95, 6.39, 4.03 or 3.75 mg/L) have been placed on the films of the etched blend and retrieved after different incubation times (ranging from 5 to 75 min). The surface density coverage of Mb ( $\Gamma$ ) for each incubation time has been determined by UV-visible spectrometry using the same procedure previously described (Eq. 3.1). Two kinetic regimes are identified depending on the initial concentration of Mb used for incubation (curves a and b of Fig. 3.13).

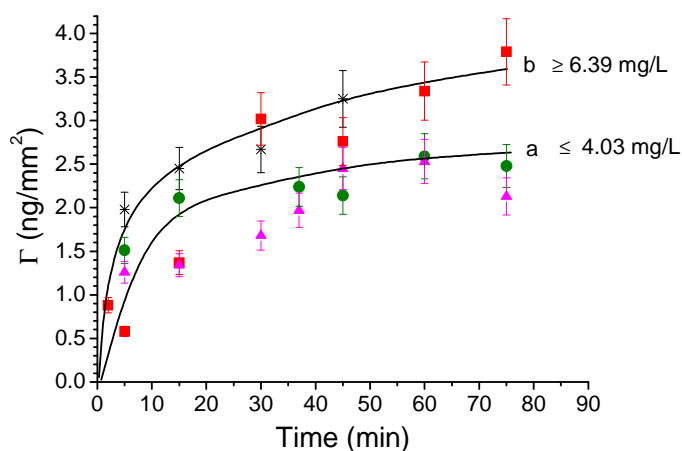


**Fig. 3.13** Adsorption kinetics experiments of myoglobin on the etched blend. The surface density coverage of Mb ( $\Gamma$ ) have been determined after different incubation times (ranging from 5 to 75 min) for different concentrations of the initial solutions of Mb; 3.75 ( $\blacktriangle$ ), 4.03 ( $\bullet$ ), 6.39 ( $\blacksquare$ ) and 7.95 ( $*$ ) mg/L.

The Langmuir isotherm (Eq. 3.2) has been used to fit the experimental data of Fig. 3.13 after linearization of kinetic data as reported in the appendix (A.3.2). From Fig. A3.2 it is apparent that for incubation time less than 15 min no regular behavior is observed, probably because the equilibrium surface coverage is not reached. However, for incubation times higher than 15 min the adsorption kinetics can be described in terms of an equilibrium Langmuir behavior, with parameters  $K = 1$  and  $\Gamma_m = 2.7$  (see table 3.2), due to the formation of a monolayer. This result confirms that the isothermal adsorption kinetics of Mb reported in Fig. 3.12 for an incubation time of 30 min as an example well describes the adsorption behavior of the etched blend in the formation of a monolayer.

We have performed Mb adsorption kinetics experiments also on PS thin films. A comparison between the kinetics performed on PS and on etched blend is reported in Fig. 3.14 for two different initial Mb concentrations, 7.95 (A) and 4.03 (B) mg/L. The results confirmed that our porous material is able to absorb higher amounts of Mb.

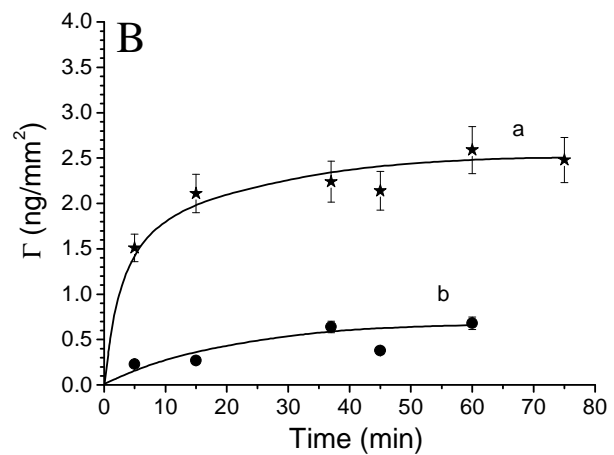
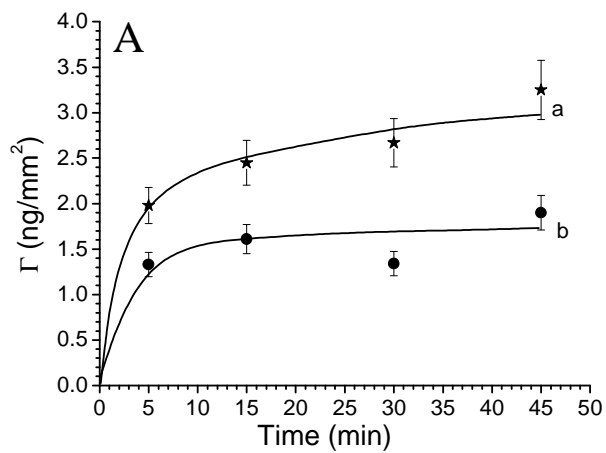


**Fig. 3.14** Comparison between the Mb adsorption kinetics on the etched blend (*a*) and on a PS thin film (*b*) for an initial Mb concentration of 7.95 (A) and 4.03 (B) mg/L.

In order to confirm the ability of our porous surface to absorb Mb, we have also determined the amount of absorbed biomolecules using quartz crystal microbalance (QCM) measurements, a well-established technique for monitoring mass depositions via changes in the resonant frequency of an AT-cut piezoelectric quartz crystal with metal electrodes deposited on its two faces [37]. To perform QCM measurements we have prepared our porous thin films on the gold working electrode of an AT-cut crystals with a fundamental resonant frequency of 10 MHz. We have verified that the lamellar morphology is retained on a gold surface (Fig. A3.3 in the appendix). Then, Mb has been physically adsorbed on our support following the same procedure previously described. In particular, we have determined the dry mass of absorbed Mb measuring the resonant frequency of the crystal after washing the quartz crystal with water in order to remove loosely bound proteins and successive drying at room temperature overnight. A comparison between the Mb adsorption kinetics obtained using QCM and UV-visible technique is reported in Fig. 3.15.

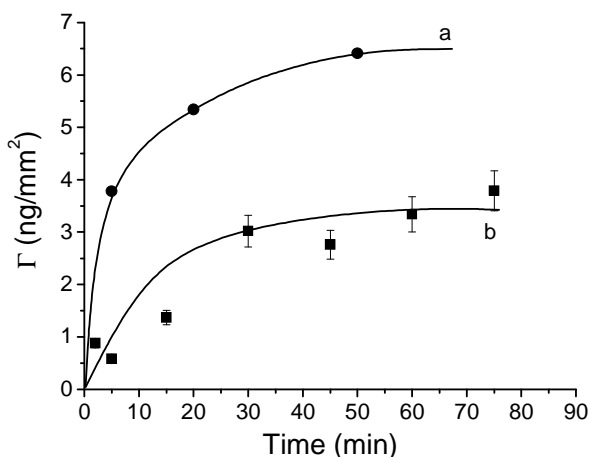


**Fig. 3.15** Adsorption kinetics experiments of myoglobin on the etched blend obtained using the QCM (a) and UV-Vis (b) technique.  $\Gamma$  is the surface density coverage of protein. Incubation temperature: 5 °C. The initial concentrations of the Mb solutions are 6.6 mg/L and 6.4 mg/L in the case of the kinetic measured with QCM and UV-Vis technique, respectively.

Qualitatively, the general shapes and time-scales of the adsorption curves resulted similar for the UV-Vis and QCM techniques but the measured mass of adsorbed protein determined with QCM is larger than that measured with the UV-visible technique. This is quite obvious because the mass obtained via the measured frequency shift of the QCM also includes water coupled to the protein and water trapped in the hydrophilic cavities of our film. Also, the underlying surface is different for the two experiments; the films have been prepared on a glass slide for UV-Vis measurements and on gold for QCM experiments. Therefore, due to the intrinsic differences in the experimental set-up of the two techniques and the different nature of supports (glass *vs* Au), a direct comparison between the amounts of adsorbed Mb determined with QCM and by UV-Vis measurements is quite hazardous. However in both cases a quasi-plateau regime in protein surface density coverage is reached after  $\sim 30$  min.

We also have studied the myoglobin adsorption on our supports, both before and after the pores formation, by neutron reflectivity. Preliminary results, reported in Fig. A3.4 in the appendix, clearly show differences between the non porous and porous layers in the mechanisms of myoglobin adsorption to the interface.

As a general remark, it is of great interest to understand protein adsorption from an aqueous environment to a solid surface and many authors have investigated adsorption of protein to solid surfaces in the last decade. However identification of general statements for describing protein adsorption on solid surfaces is still a challenge. Biomolecules adsorption is a very complex process that depends not only on the chemical and physical characteristic of the surface but also by different protein-surface forces, including van der Waals, hydrophobic and

electrostatic forces. Attention has to be also paid to the sub processes like structural rearrangements in the protein, dehydration of the protein and parts of the surfaces and redistribution of charged groups in the interfacial layer. The effect of many variables like pH, temperature, the ionic strength, and the nature of the solvent protein adsorption have to be taken also into account.

### **3.5 Catalytic performance of immobilized horseradish peroxidase (HRP)**

For biosensing applications, maintenance of structure and functions of immobilized proteins is of primary importance. Non-porous materials, to which enzymes are attached to the surfaces, are subjected to minimum diffusion limitation while enzyme loading per unit mass of support is usually low. On the other hand, porous materials can afford high enzyme loading, but usually suffer a much greater diffusional limitation of substrate. For these reasons the evaluation of the catalytic performance of immobilized enzymes is a critical issue.

In this paragraph, we evaluate the catalytic performance of the enzyme horseradish peroxidase (HRP) immobilized on our porous surfaces and we compare it with the enzyme immobilized on PS thin films and glass slides.

HRP is an important heme-containing enzyme that has been studied for more than a century [38 *a*]. It is a single chain polypeptide containing four disulfide bridges. It is a glycoprotein containing 18% carbohydrate and has a total molecular mass of 44000 Da [38 *b*] and dimensions of 4.0 nm x 6.7 nm x 11.7 nm (Fig. 3.16) [38 *c*].

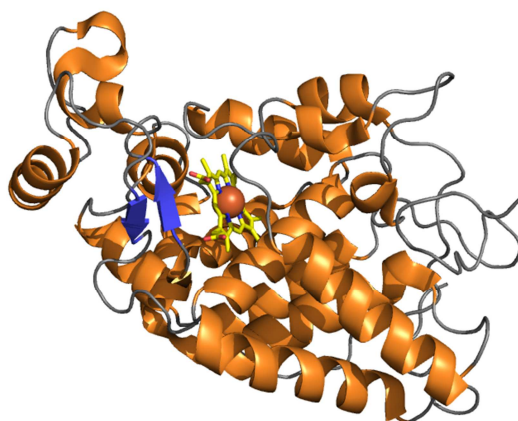


**Fig. 3.16** Overall fold of EST2 of Horseradish Peroxidase (HRP) [38 c].

HRP readily combines with hydrogen peroxide ( $\text{H}_2\text{O}_2$ ) and the resultant [HRP- $\text{H}_2\text{O}_2$ ] complex can oxidize a wide variety of substrates. To evaluate the activity of immobilized HRP, we have selected a well-known peroxidase-catalyzed reaction, the one-electron oxidation of 2,2'-azino-bis(3-ethylbenzothiazoline-6-sulfonate) (ABTS) into the corresponding radical-cation,  $\text{ABTS}^{\bullet+}$  (Fig. 3.17). The radical-cation  $\text{ABTS}^{\bullet+}$  has an absorption maximum at 420 nm ( $\epsilon_{420}=3.6 \times 10^4 \text{ M}^{-1} \text{ cm}^{-1}$ ); it absorbs also at 340 nm ( $\epsilon_{340} = 5.4 \times 10^3 \text{ M}^{-1} \text{ cm}^{-1}$ ) and 740 nm [34].

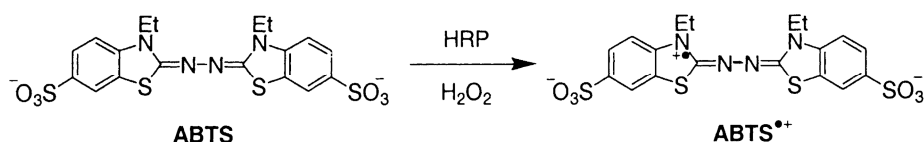


**Fig. 3.17** One-electron oxidation of 2,2'-azino-bis(3-ethylbenzothiazoline-6-sulfonate) (ABTS) into the corresponding radical-cation ( $\text{ABTS}^{\bullet+}$ ) catalyzed by the enzyme horseradish peroxidase (HRP) and  $\text{H}_2\text{O}_2$ .

The activity of the immobilized HRP on the different surfaces has been analyzed by Visible spectrometry. In a *first step* the enzyme HRP has been physically absorbed on the various surfaces and in a *second step* the activity of the enzyme has been evaluated by placing a fresh prepared

solution of ABTS and H<sub>2</sub>O<sub>2</sub> on the surfaces containing immobilized HRP (see Paragraph 3.2.4 for details about the experimental procedure). The formation of the reaction product (ABTS<sup>•+</sup>), resulting from the catalysis of ABTS by the immobilized HRP, has been verified both visually, due to a color change in the solution from clear to green (color of the radical-cation ABTS<sup>•+</sup>), and quantitatively by recording the UV-Vis spectrum of the solutions.

We have performed different experiments by varying the time of contact between the enzyme solutions and the surfaces during the immobilization phase (*step 1*). In particular, we have used three different incubation times (30, 90 and 150 min). The enzyme solution concentration in *step 1* and the experimental conditions during the *step 2* to verify the enzyme activity, instead, have been kept identical in the three experiments. In particular we have deposited on the surfaces (containing immobilized HRP) 500 μL of a phosphate buffer solution (pH 4.6) containing ABTS and H<sub>2</sub>O<sub>2</sub> in the concentrations 2.45 mM and 9.75 mM, respectively. In a few minutes, we have observed a change in color of the ABTS/H<sub>2</sub>O<sub>2</sub> solutions deposited on the surfaces. The color of the solutions becomes green, indicating ABTS<sup>•+</sup> formation. The UV-Vis spectra of the solutions acquired after 5 minutes of contact between the ABTS/H<sub>2</sub>O<sub>2</sub> solutions and the etched blend, PS and glass slide surfaces containing immobilized HRP are reported in figure 3.18 A-C, for three different incubation time.

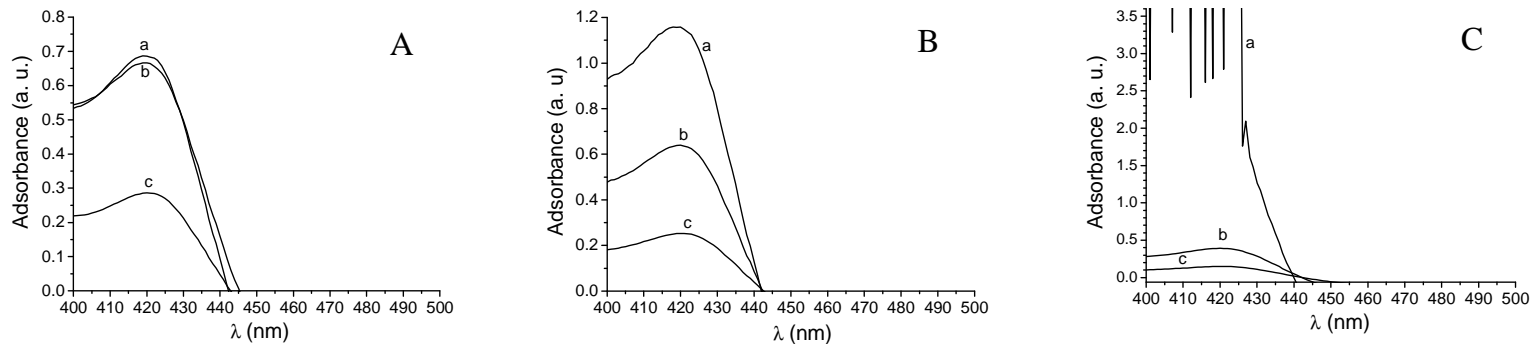


**Fig. 3.18 A-C** UV-Visible spectra of the ABTS/ABTS<sup>•+</sup> solutions retrieved after 5 minutes of contact with the HRP enzyme immobilized on the etched blend (*a*), PS (*b*) and the glass slide (*c*) for different HRP incubation times; 30 (**A**), 90 (**B**) and 150 (**C**) min.

All the profiles of Fig. 3.18 show the absorption peak at 420, indicating the presence of ABTS<sup>•+</sup> in the solutions. However, the intensity of the peak, proportional to the amount of the reaction product and therefore indicative of the catalytic efficiency of the immobilized enzyme, is different for the solutions retrieved from the different surfaces. In all the spectra of the Fig. 3.18 A-C the absorbance of the solutions exposed to the glass slide (curves c of Fig. 3.18) is less than the solutions exposed to etched blend (curves a of Fig. 3.18) and PS (curves b of Fig. 3.18) indicating a lower activity of the enzyme immobilized on the glass. Using an incubation time of 30 min, no appreciable differences have been observed in the spectra of the solutions retrieved from PS (curve b of Fig. 3.18A) and etched blend (curve a of Fig. 3.18A). Notably, using longer incubation time (Fig. 3.18 B and C), the intensity of the ABTS<sup>•+</sup> characteristic peaks in the solution retrieved from our porous support (curves a of Fig. 3.18 B and C) sensibly increases with respect to the solution deposited on the PS surface (curves b of Fig. 3.18 B and C). Using an incubation time of 150 min, the peak at 420 nm in the case of the etched blend is so intense that is out of scale (curve a of Fig. 3.18 C). The results of Fig. 3.18 indicate that using a short incubation time the quantity of the HRP immobilized on the PS film and on the etched blend is approximately the same but using longer incubation times the quantity of enzyme that is able to absorb on our porous support is higher. This is reasonable considering that a longer time is required to allow the penetration of the enzyme in the pores of our support.

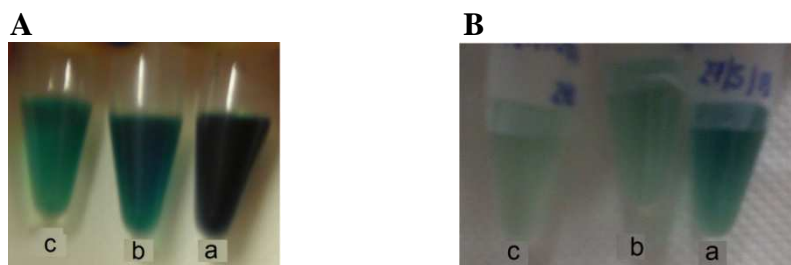


**Fig. 3.19** Photographs of the ABTS/ABTS<sup>+</sup> solutions retrieved from the etched blend (a), the PS (b) and glass slide (c) in the case of the experiment reported in Fig. 3.18 C (A) and in the case of the experiment reported in Fig. 3.20 C (B).

The development of the reaction product ABTS<sup>+</sup> can be also visually verified. As example, in figure 3.19 A the photographs of the solutions retrieved from the etched blend (a), the PS thin film (b) and glass slide (c) in the case of the experiment of fig. 3.18 C are reported. The intensity of the color solution, proportional to the concentration of the radical-cation, is higher in the solution retrieved from our porous support. The obtained concentrations of ABTS<sup>+</sup> are reported in table 3.3

**Table 3.3** concentrations of ABTS<sup>+</sup> in the retrieved solutions after 5 minutes of contact with the HRP enzyme immobilized on the etched blend, PS and the glass slide for different incubation times (IT) of the enzyme on the different supports. In the case of IT 30 min, the activity tests have been performed immediately after the enzyme immobilization (A) and after 7 (B) and 18 (C) days from the immobilization. The activity tests for IT 90 and 150 min have been performed immediately after the enzyme immobilization. For all the tests we have used an initial ABTS and H<sub>2</sub>O<sub>2</sub> concentration of 2.45 and 9.75 mM, respectively.

	<b>C<sub>ABTS+</sub></b> (mg/mL)				
	<b>IT 30 min</b>			<b>IT 90 min</b>	<b>IT 150 min</b>
	<b>A</b>	<b>B</b>	<b>C</b>		
<b>Etched blend</b>	102	48	17	176	(a)
<b>PS</b>	99	20	4	97	60
<b>Glass slide</b>	41	16	1	38	23

(a) The absorbance is out of scale.

All the data suggest that the enzyme retained its activity after immobilization on the different surfaces and that it shows an increased activity when immobilized on our porous support if the incubation time is

long enough. The result that the incubation protocol of the HRP on our porous surfaces entails a threshold time to significantly differentiate the enzymatic activity of HRP adsorbed on the flat supports suggests that the immobilization process is diffusion limited. In the case of PS and glass supports, indeed, HRP is adsorbed on a flat surface, and only the specific balance of hydrophobic/hydrophilic interactions with the plays a key role. In the case of the porous surface of our etched blend, instead, also the diffusion of HRP inside the pores comes into play, since the pore dimensions are comparable with the average dimensions of the enzyme molecules.

We also have studied the enzyme activity by varying the concentrations of hydrogen peroxide and ABTS (Fig. A3.5 in the Appendix). The enzyme immobilized on our porous support shows an increased activity with respect to the enzyme immobilized on a glass and PS thin film in all the performed experiments. The total activity is much greater for immobilization onto the porous support, as expected as a result of its much greater surface area, provided that the incubation time is higher than a threshold.

Stability of the immobilized enzyme with aging is also critical. Therefore we have characterized the surfaces in terms of long term stability of enzyme activity by measuring the activity of the enzyme upon aging the supports for 7 and 18 days after immobilization, using a fixed incubation time (30 min). The experimental procedure to test the HRP catalytic performance is the same previously described. The recorded UV-Visible spectra of the ABTS/ABTS<sup>•+</sup> solutions and the amount of ABTS<sup>•+</sup> obtained in the different activity tests are reported in Fig. 3.20 and table 3.3, respectively. The photographs of the solutions of the experiment reported in Fig. 3.20 C are reported in Fig. 3.19 B.

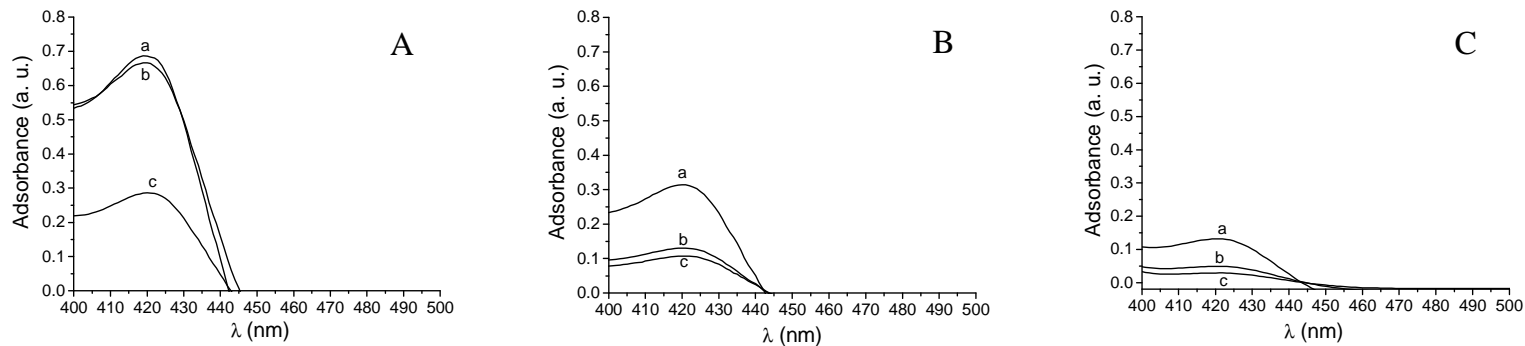


**Fig. 3.20 A-C** UV-Visible spectra of the ABTS/ABTS<sup>++</sup> solutions retrieved after 5 minutes of contact with the HRP enzyme immobilized on the etched blend (*a*), PS (*b*) and the glass slide (*c*), immediately after the enzyme immobilization (**A**) and after 7 (**B**) and 18 (**C**) aging. The incubation time is 30 minutes for all the tests.

As previously discussed (Fig. 3.18 A), when we perform the activity test immediately after the enzyme immobilization after 30 min incubation time, the HRP over the glass slide exhibits the lowest activity while the HRP immobilized on our porous support shows an activity similar to that immobilized on PS thin film (curves a and b of Fig. 3.20 A). The absorbance intensities decrease with increase of aging time for all the surfaces (Fig. 3.20 B, C) indicating that the ability of the HRP to catalyze the ABTS oxidation progressively decreases over the time. However, for the enzyme immobilized on our porous support there is a less pronounced loss in enzyme activity with aging time (curves a of Fig. 3.20 B, C). In particular, after 7 days, the loss of activity is 53% in the case of the etched blend and 80% and 61% in the case of the PS thin film and the glass slide, respectively. Therefore for non-porous supports there is significant activity loss. After 18 days (Fig. 3.20 C), the HRP immobilized on our porous support shows a residual activity of 17% while almost a total absence of activity is observed for the HRP immobilized on PS and glass slide. HRP immobilized on non-porous support displays a more significant decrease in enzyme activity. In other words, enzyme immobilized on non-porous supports is deactivated at a higher rate and our porous matrix is significantly superior in maintaining enzyme activity. It is possible that the porous structure provides an environment that protects enzyme from deactivation. Therefore the use of porous supports not only yields greater enzymatic activity, but also significantly improves its long term stability. It is worth noting that these results have been obtained after storage the dried samples for 7 or 18 days at 4 °C without particular precautions. Probably, a major control of the storage conditions could possibly lead to better performances of immobilized enzyme upon aging with use of our nanoporous support.

### 3.6 Immobilized Esterase 2 (EST2) as biosensor for the detection of specific organophosphate pesticides

The phosphorus-based compounds, known as organophosphates (OPs), have become the most diffuse neurotoxic chemical compounds [39 *a*]. The general structure of these molecules is shown in Figure 3.21 A. The mechanism of action of these neurotoxic compounds concerns mainly the irreversible inhibition of acetylcholinesterase, a key enzyme for the correct activity of the nervous system [39 *b*]. Among the organophosphates compounds, paraoxon (Fig. 3.21 B) is one of the most used pesticide in agriculture [30 *a*]. It is also widely studied for its neurotoxic, cancerous, and teratogenic effects, which have been observed even at very low concentrations [30 *b, c*]. The compound is slowly degraded in the environment, allowing frequently its recovery in the food chain [40].

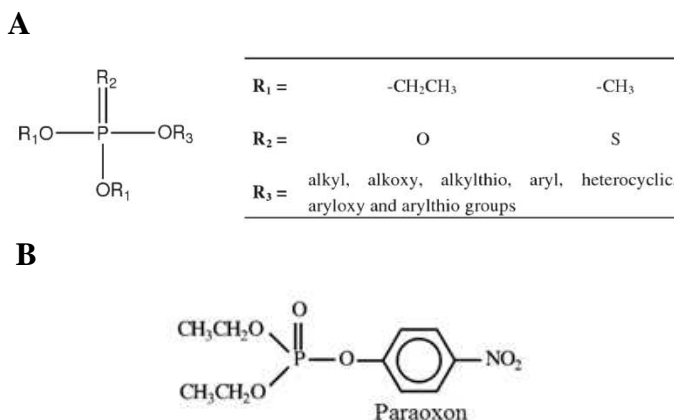


**Fig. 3.21** General molecular formulas of organophosphates (A) and paraoxon structure (B).

Because of toxicity to humans, the removal of excess of organophosphates compounds from the environment is mandatory, but a preliminary action of detection and monitoring is also required. At the

present, the classical methods of pesticide detection makes use of gas chromatography (GC), high pressure liquid chromatography (HPLC), and recently mass spectrometry (MS) approaches [41]. These techniques are very powerful tools for monitoring toxic analytes, but they are expensive, time-consuming, and sometimes are not adapt for in situ and real-time detection. In contrast, the easy handling of a pesticide biosensor would make possible carrying out the analysis also from part of untrained people, suggesting a future diffusion of such devices in the domestic market. Pesticides biosensors have the potential to complement or replace the classical analytical methods by simplifying or eliminating sample preparation protocols and making the testing in the field easier and faster with a significant decrease of the analysis costs.

In this paragraph we describe the possibility to use the enzyme Esterase 2 from *Alicyclobacillus acidocaldarius* (EST2), immobilized on our block-copolymer based porous support (etched blend, Fig. 3.7 A and 3.8 A), as biosensor for the detection of paraoxon (Fig. 3.21 B). The detection strategy is based on the fact that paraoxon can covalently link to the EST2 active site irreversibly inhibiting the enzyme hydrolase activity. In paragraph 3.6.1 we evaluate the hydrolase catalytic performance of the immobilized EST2 enzyme using *p*-nitrophenyl butyrate (*p*-NP-C4) as substrate (Fig. 3.23). In paragraph 3.6.2 we test the EST2 inhibition by paraoxon. In particular, we have measured residual activity of the immobilized enzyme after the contact with paraoxon, in order to evaluate the capability of the immobilized enzyme to detect this specific organophosphate compound.

### 3.6.1 Catalytic performance of immobilized EST2

EST2 is a thermophilic carboxylesterase isolated and cloned from *Alicyclobacillus acidocaldarius*. It is a monomeric protein of about 34 KDa and its structural model [42] revealed a roughly ellipsoidal shape with approximate dimensions of 4.4 nm x 4.7 nm x 5.4 nm. Its structure shows the typical features of the  $\alpha/\beta$ -hydrolase fold; in particular, it consists of a central eight-stranded mixed  $\beta$ -sheet surrounded by five helices (Fig. 3.22).

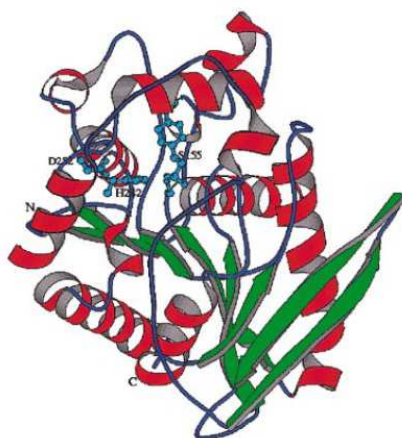


**Fig. 3.22** Overall fold of EST2: helices are shown in red,  $\beta$ -strands in green and others in blue. The residues of the catalytic triad are shown in cyan. Reproduced from ref. 42.

EST2 hydrolyses monoacyl esters of different acyl chain lengths and different compounds of pharmacological and industrial interest [31]. The enzyme displays maximum activity on *p*-nitrophenyl (*p*NP) esters characterized by an acyl chain length of 6-8 carbon atoms, at an optimum temperature of 70 °C and shows a discrete activity also at room temperature. The three-dimensional structure of EST2 shows that its catalytic triad consists of the three residues, Ser155, His282 and Asp252, all located on the C-terminal side of the mixed central  $\beta$ -sheet (Fig. 3.22).

In the following, we compare the catalytic performance of the EST2 immobilized on our BCP based porous surfaces (etched blend, Fig. 3.7 A and 3.8 A) and on a glass slide, using the *p*-nitrophenyl butyrate (*p*-NP-C4) as substrate. The relevant reaction is reported in Figure 3.23. The released *p*-nitrophenol (*p*-NP) shows an absorption maximum at 405 nm, therefore its formation can be monitored by following the increase of the absorbance at this wavelength. We have selected the substrate *p*-NP-C4, containing an acyl chain length of 4 carbon atoms, because of the poor water solubility of the substrates containing longer carbon chains.

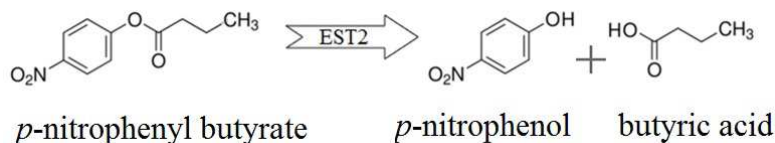


**Fig. 3.23** EST2-catalyzed hydrolysis of *p*-nitrophenyl butyrate (*p*-NP-C4). The reaction products are *p*-nitrophenol (*p*-NP) and butyric acid. The *p*-nitrophenol formation can be followed by visible spectrometry monitoring the adsorption peak at 405 nm.

In a *first step* the EST2 enzyme has been physically absorbed on the surfaces by placing 110  $\mu\text{L}$  of the enzyme solution in contact with the surfaces for a fixed time (incubation time).

In a *second step* we have evaluated the catalytic performance of the immobilized enzyme at room temperature by placing a freshly prepared solution of *p*-nitrophenyl butyrate (*p*-NP-C4) on the surfaces containing the immobilized EST2 and by monitoring the absorbance increment at 405 nm, due to the formation of the reaction product *p*-nitrophenol (*p*-NP) (Fig. 3.23). See part *a* in paragraph 3.2.5 for experimental details.

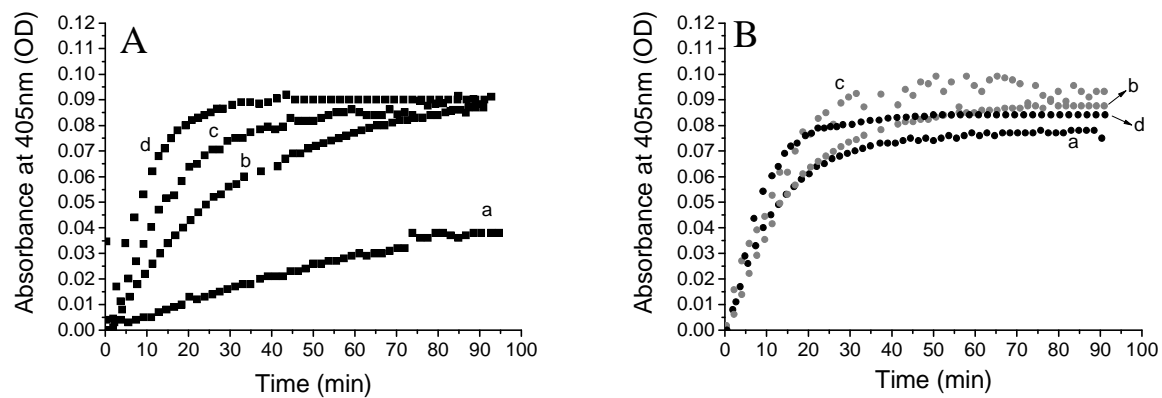


**Fig. 3.23** Absorbance at 405 nm of *p*-nitrophenol (*p*-NP) produced in the reaction between the substrate *p*-nitrophenyl butyrate (*p*-NP-C4) and the EST2 enzyme immobilized on the etched blend (A) and a glass slide (B) for different enzyme incubation time; 90 min (a), 2 days (b), 3 days (c) and 6 days (d).

We have performed different experiments by using different incubation time, that is the time of contact between the enzyme and the surfaces during the immobilization step (*step 1*). In particular, we have used the following incubation times: 90 min and 2, 3 and 6 days. After these incubation times, the samples have been rinsed to remove enzyme molecules that are weakly adsorbed on the surface and the enzyme activity has been tested as previously described (*step 2*, part *a* of the paragraph 3.2.5). The results are reported in Fig. 3.23 in the case of the enzyme immobilized on our porous support (etched blend) (A) and a glass slide (B). An increase in the absorbance at 405 nm, due to the *p*-nitrophenol (*p*-NP) released by the reaction between the substrate *p*-NP-C4 and the immobilized EST2 enzyme, is observed for both the etched blend (Fig. 3.23 A) and the glass slide (Fig. 3.23 B), demonstrating that the immobilized enzyme retains its activity on both surfaces. In the case of the glass slides, the maximum enzyme activity is already reached using the lowest explored incubation time (90 min) (curve a of Fig. 3.23 B); no significant increments in enzyme activity are observed by further increase of the incubation time (curves b-d of Fig. 3.23 B). On the contrary, the activity of the enzyme immobilized on our porous support increases by using longer incubation time (Fig. 3.23 A). This is reasonable considering that a longer time is required to allow the penetration of the enzyme in the porous of our material. The slopes of the kinetics curves obtained by the linear fitting of the initial kinetic data of Fig. 3.23 are reported in Fig. 3.24. It is apparent that after ~ 120 h incubation time the activity of the EST2 immobilized on the glass and porous supports becomes almost identical.

We also have verified the morphology of our etched blend after the enzyme immobilization step and subsequent activity test with *p*-NP-

C4 (Fig. A3.6 in the Appendix). Notably, our the thin film retains its lamellar porous structure also after the contact with aqueous solutions for long time (6 days), the rinsing, and the activity test, demonstrating the high potential of our support to fabricate active layers in biosensors.

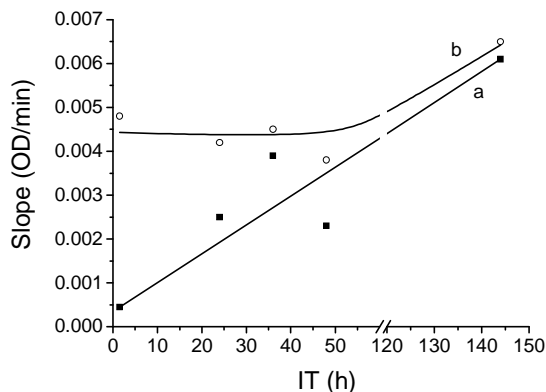


**Fig. 3.24** Slopes obtained by the linear fit of the initial points of the kinetics data reported in Fig. 3.23 in function of the incubation time (IT) in the case of the enzyme immobilized on the etched blend (a, ■) and on the glass slide (b, ○).

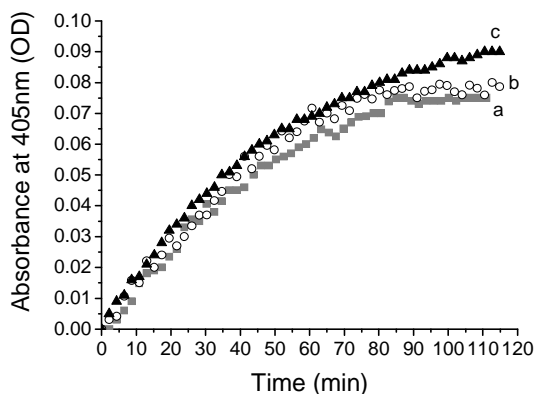


**Fig. 3.25** Absorbance at 405 nm of *p*-nitrophenol (*p*-NP) obtained by the reaction between the substrate *p*-nitrophenyl butyrate (*p*-NP-C4) and the EST2 enzyme immobilized on the etched blend after aging the immobilized enzyme for 1h (a, ■), 3 days (b, ○) and 7 days (c, ▲). The enzyme incubation time during the immobilization step is fixed at 90 min.

To evaluate the stability over the time of the enzyme immobilized on the etched blend, we have performed enzymatic activity tests after 1h,

3 days and 7 days from immobilization, using a fixed incubation time (90 min). The results are reported in Fig. 3.25. Notably, no activity loss is observed even by aging the immobilized enzyme for 7 days with the time (curve c of Fig. 3.25), demonstrating the high stability of the EST2 enzyme.

### 3.6.2 EST2 residual activity after contact with paraoxon

It has been demonstrated that the EST2 enzyme can be used as a biosensor for the detection of specific organophosphate pesticides because its activity is highly sensible to organophosphates (OP) inhibition [29 b] . The inhibition mechanism by paraoxon is reported in Fig. 3.26. Paraoxon, one of the most used pesticide in agriculture and also widely studied for its neurotoxic, cancerous, and teratogenic effects [30], covalently links to the Ser 155 residue of the EST2 active site, inhibiting the carboxylesterase activity of the enzyme.

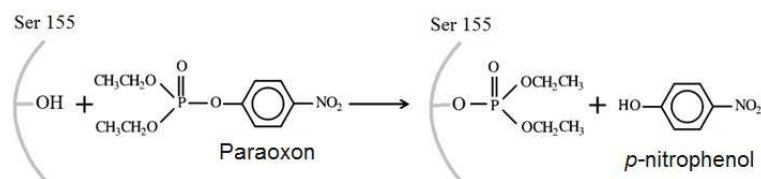


**Fig. 3.26** Inhibition mechanism of EST2 by paraoxon. The paraoxon covalently links to the Ser 155 residue of the EST2 active site, inhibiting the carboxylesterase activity of the enzyme. *p*-nitrophenol (*p*-NP) is released after the covalent binding.

The evidence that carboxylesterase activities are sensible to the organophosphates inhibition, dates back to the '70ies, and was associated to the pesticide resistance in aphids and mosquitoes [43] but only recently these enzymes have raised interest as part of biosensors in environmental monitoring [44].

The direct monitoring of EST2 inhibition by paraoxon could be possible by measuring the release of *p*-nitrophenol (*p*-NP) from paraoxon hydrolysis, as the consequence of covalent binding of phosphoryl group to serine 155 in the catalytic site of EST2 (Fig. 3.26). However the signal at 405 nm (maximum of absorbance for *p*-NP) monitored in this way results low due to the poor level of *p*-NP generated in the assay. Better results in the paraoxon detection can be obtained by monitoring the EST2 residual activity after inactivation by paraoxon. Therefore we have used this strategy to test the ability of the enzyme immobilized on our porous supports, on PS thin films and on glass slides, to detect paraoxon. The experimental procedure has been described in part *b* of paragraph 3.2.5. We have tested the catalytic performance of the EST2 enzyme immobilized on the different supports before and after the contact with paraoxon solutions at different concentrations (range 0.02 – 0.50  $\mu\text{M}$ ). The substrate *p*-nitrophenyl butyrate (*p*-NP-C4) has been used to test the enzyme activity, as described in the previous paragraph. Typical results, obtained in the case of the etched blend and by using concentrations of paraoxon solutions in the range 0.04 – 0.5  $\mu\text{M}$ , are reported in Fig. 3.27 as example. The EST2 activity in absence of paraoxon is also reported (curve a of Fig. 3.27). After the contact with paraoxon, a remarkable decrease in enzyme activity is observed. In particular, the enzyme activity is reduced by more than 60% already for the lowest reported paraoxon concentration (curve b of Fig. 3.27). This concentration corresponds to 0.04  $\mu\text{M}$  that is  $\sim 4$  pmol of paraoxon in 110  $\mu\text{L}$  of solution, indicating that the immobilized enzyme can be used to detect paraoxon in the pmoles range. These results confirm that our porous support containing the immobilized EST2 enzyme can be used as active part for the construction of a biosensor for the paraoxon detection.

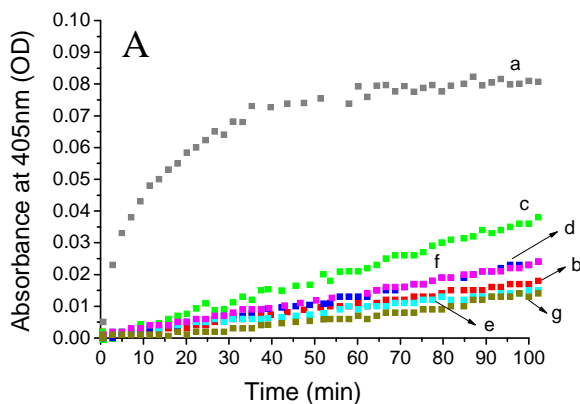


**Fig. 3.27** Residua activity of EST2 immobilized on the etched blend in absence of paraoxon (a, ■) and after contact with paraoxon solutions at different concentrations in the range 0.04 – 0.50  $\mu\text{M}$ . In particular, the paraoxon concentrations are 0.04 (b, ■), 0.14 (c, ■), 0.23 (d, ■), 0.32 (e, ■), 0.41 (f, ■) and 0.50 (g, ■)  $\mu\text{M}$ . These concentrations correspond to  $\sim 4, 15, 25, 35, 45$  and  $55$  pmol of paraoxon in  $110 \mu\text{L}$  of solution, respectively.

Similar kinetic curves for the determination of residual activity of EST2 have been measured also using PS and glass as supports. In Fig. 3.28 the slope of the kinetic curves describing the residual activity of EST2 immobilized on the different supports as a function of the concentration of paraoxon solutions, used as inhibitor, is compared. Roughly a unique behavior is identified, showing that the rate of the hydrolysis reaction of *p*-NP-C4 with residual EST2 decays by addition of inhibitor identically, with the advantage that our BCP based nanoporous surface can be finely tuned for the pore size and hydrophilicity, and can be also used as coating over different materials.

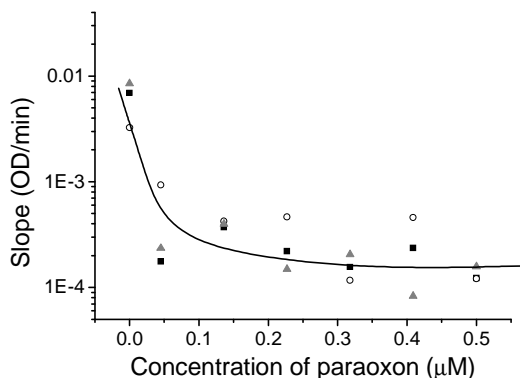


**Fig. 3.28** Slope of the kinetic curves describing the residual activity of EST2 immobilized on the different supports as a function of the concentration of paraoxon solutions; etched blend (■), PS (▲) and glass (○). Paraoxon solutions with concentrations ranging between 0.02 and 0.5 μM have been used.

The value of adsorbance at 100 min reaction time at each paraoxon (inhibitor) concentration  $C$  ( $A_{100min}(C)$ ) and in absence of inhibitor ( $A_{100min}(0)$ ) have been used to calculate the relative drop in absorbance at 100 min as:

$$\Delta A_{100min} = \frac{A_{100min}(0) - A_{100min}(C)}{A_{100min}(0)} \quad (\text{Eq. 3.3})$$

where the values of absorbance have been corrected for the spontaneous hydrolysis of paraoxon at 100 min. The value of the relative drop in absorbance ( $\Delta A_{100min}$ ) undergoes a linear increase with concentration of inhibitor, up to reach a value of 1 when all EST2 active sites have been inhibited by paraoxon.

The values of  $\Delta A_{100min}$  as a function of the concentration of paraoxon in the case of our porous support are reported in Fig. 3.29.

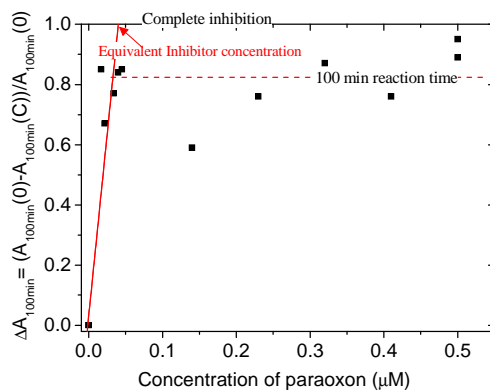


**Fig. 3.29** Relative drop in absorbance ( $\Delta A_{100min}$ ), calculated according to the Eq. 3.3, vs the concentration of paraoxon in the case of our porous supports. The linear extrapolation used to evaluating the equivalent inhibitor concentration is also reported.

The linear extrapolation of the relative drop in absorbance, due to addition of paraoxon, allows evaluating the equivalent inhibitor concentration needed for full inhibition, equal to 0.04  $\mu\text{M}$  (Fig. 3.29). Since the ratio between active sites in EST2 to paraoxon is 1:1, the number of active EST2 molecules present on our substrate is 4.4 pmol (= 0.04  $\mu\text{M}$  x 110  $\mu\text{L}$ , with 110  $\mu\text{L}$  the volume of paraoxon solutions used for each measurements).

### **3.7 Conclusions to Chapter III**

Exploiting the partial miscibility of polyethylene oxide (PEO) and poly(L-lactide) (PLLA), and the possibility to easily remove PLLA blocks by basic hydrolysis, we have set up a procedure that allows building nanostructured membranes with well defined architecture containing pores ( ~ 20 nm in width) delimited by PEO hydrophilic walls. The large surface area, the tailored pore sizes and the functionalization with hydrophilic PEO blocks make the designed nanostructured material suitable supports for the immobilization of specific biomolecules (myoglobin, HRP and EST2). The porous structure is beneficial for the loading of large amount of myoglobin, moreover the use of our porous supports as confining agent for the HRP improves the catalytic performance of the enzyme without mass-transfer limitations. The total activity of HRP immobilized onto porous supports is greater than that of HRP immobilized onto flat hydrophilic (glass) and hydrophobic (PS) surfaces and the presence of pores makes the long term stability of immobilized enzyme high. Finally, we have also demonstrated that the EST2 immobilized on our porous support can act as active layer in biosensors for the detection of the organophosphate compound paraoxon.

## BIBLIOGRAPHY CHAPTER III

- [1] a) S. Rodriguez-Mozaz, M. P. Marco, M. J. Lopez de Alda, D. Barceló, *Pure Appl. Chem.* **2004**, 76, 4, 723. b) K. Reder-Christ, G. Bendas, *Sensors* **2011**, 11, 9450. c) L. D. Mello, L. T. Kubota, *Food Chemistry* **2002**, 77, 237.
- [2] a) K. Cammann, U. Lemke, A. Rohen, J. Sander, H. Wilken, B. Winter, *Angew. Chem.* **1991**, 103, 519. b) Y. K. Cho, J. F. Bailey, *Biotechnology and Bioeng.* **1978**, 20, 1651. c) D. Thevenot, K. Thot, R. Durst, G. Wilson, *Pure Appl. Chem.* **1999**, 71, 2333.
- [3] a) A. F. Collings, F. Caruso, *Rep. Prog. Phys.* **1997**, 60, 1397. b) J. L. Blum, P. R. Coulet, *Biosensor: Principle and Application* **1989**, Oxford Univ. Press, NY.
- [4] S. L. Brook, I. J. Higgins, J. D. Newmann, A. P. F. Turner, *Enzyme Microb. Technology*, **1991**, 13, 946. A. P. F. Turner, *Analytical Proceedings* **1991**, 28, 376.
- [5] a) I. Willner, R. Baron, B. Willner, *Biosens. Bioelectron.* **2007**, 22, 1841. b) B. Bhushan, *Springer Handbook of Nanotechnology* **2010**, 3rd ed. Springer, Heidelberg. c) K. Hernande, R. Fernandez-Lafuente, *Enzyme Microb. Technol.* **2011**, 48, 107.
- [6] a) A. P. Fang, H. T. Ng, S. F. Y. Li, *Biosens. Bioelectron.* **2003**, 19, 43. b) P. B. Lippa, L. J. Sokoll, D. W. Chan, *Clinica Chimica Acta* **2001**, 314, 1.
- [7] H. H. Weetall, *Biosens. Bioelectron.* **1999**, 14, 237.
- [8] a) B. Kasemo, *Surface Science* **2002**, 500, 656. b) D. G. Castner, B. D. Ratner, *Surface Science* **2002**, 500, 28.
- [9] a) J. D. Hoheisel, *Nat. Rev. Genet.* **2006**, 7, 200. b) M. C. Pirrung, *Angew. Chem. Int. Ed.* **2002**, 41, 1279. c) S. Draghici, P. Khatri, A. C. Eklund, Z. Szallasi, *Trends Genet.* **2006**, 22, 101.

- [10] a) A. Guo, X. Zhu, *Int. J. Nanosci.* **2007**, 6, 109. b) C. H. Jang, M. L. Tingey, N. L. Korpi, G. J. Wiepz, J. H. Shiller, P. Bertics, N. L. Abbott, *J. Am. Chem. Soc.* **2005**, 25, 8912.
- [11] A. Fersht, *Structure and Mechanism in Protein Science. A Guide to Enzyme Catalysis and Protein Folding* **1999**, W. H. Freeman and Company, New York.
- [12] B. Lee, G. Vasmatzis, *Curr. Opin. Biotechnol.* **1997**, 8, 423.
- [13] C.ò. Fàgaàin, *Enzyme Microbial Technol.* **2003**, 33, 137.
- [14] N. A. Chaniotakis, *Anal. Bioanal. Chem.* **2003**, 378, 89.
- [15] a) E. Casero, M. Darder, F. Pariente, L. Encarnacio, J. Martìn-Benito, L. Vázquez, *Nano Lett.* **2002**, 2, 577. b) J. M. Abad, M. Velez, C. Santamaria, J. M. Guisan, P. R. Matheus, L. Vazquez, I. Gazaryan, L. Gorton, T. Gibson, V. M. Fernandez, *J. Am. Chem. Soc.* **2002**, 124, 12845. c) T. R. Besanger, Y. Chen, A. K. Deisingh, R. Hodgson, W. Jin, S. Mayer, M. A. Brook, J. D. Brennan, *Anal. Chem.* **2003**, 75, 2382.
- [16] a) N. J. Geddes, E. M. Paschinger, D. N. Furlong , Y. Ebara, Y. Okahata, K. A. Than, J. A. Edgar, *Sens. Actuators B* **1994**, 17 125. b) F. Caruso, E. Rodda, D. N. Furlong, *J. Colloid Interface Sci.* **1995**, 178 104. c) F. Caruso, P. S. Vukusic, K. Matsuura, R. S. Urquhart, D. N. Furlong, Y. Okahata. *Colloids Surfaces A: Physicochem. Eng. Aspects* **1995**, 103, 147.
- [17] P. Roach, D. Farrar, C. C. Perry, *J. Am. Chem. Soc.* **2005**, 127, 8168.
- [18] a) J. R. Lu, X. Zhao, M. Yaseen, *Curr. Opin. Colloid Interface Sci.* **2007**, 12, 9. b) N. Brouette, G. Fragneto, F. Cousin, M. Moulin, M. Haertlein, M. Sferrazza, *J. Colloid Interface Sci.* **2013**, 390, 114.
- [19] a) Z. Holland, E. Katchalski-Katzir, *Mol. Immunol.* **1986**, 23, 927. b) J. E. Butler, L. Ni, R. Nessler, K. S. Joshi, M. Suter, B. Rosenburg, J. Chang, W. R. Brown , L. A. Cantarero, *J. Immunol. Methods* **1992**, 150, 77.

- [20] a) J. N. Lin, J. Herron, J. D. Andrade, M. Brizgys, *IEEE Trans Biomed. Eng.* **1988**, 35, 466. b) G. J. Leggett, C. J. Roberts, P. M. Williams, M. C. Davies, D. E. Jackson, S. J. B. Tendler, *Langmuir* **1993**, 9, 2356. c) M. Thompson, C. L. Arthur, G. K. Dhaliwal, *Anal. Chem.* **1986**, 58, 1206.
- [21] a) J. Huang, C. M. Hooijmans, C. A. Briasco, S. G. M. Geraats, K. C. A. M. Luyben, D. Thomas, J. N. Barbotin, *Appl. Microbiol. Biotechnol.* **1990**, 33, 619. b) H. Gunasingham, P. Y. T. Teo, Y. H. Lai, S. G. Tang, *Biosensors* **1989**, 4, 349.
- [22] G. H. T. Luong, A. L. Nguyen, G. G. Guilbault, *Adv. Biotechnol. Bioeng.* **1993**, 50, 86.
- [23] a) V. Vamvakaki, N. A. Chaniotakis, *Biosensors and Bioelectronics* **2007**, 22, 2650. b) R. Ravindra, S. Zhao, H. Gies, R. Winter, *J. Am. Chem. Soc.* **2004**, 126, 12224. c) A. J. Garcia, M. D. Vega, D. Boettiger, *Mol. Biol. Cell* **1999**, 10, 785. d) L. Baugh, V. Vogel, *J. Biomed. Mater. Res. Part A* **2004**, 69, 525. e) M. L. B. Palacio, S. R. Schricker, B. Bhushan, *J. Biomed. Mater. Res. Part A* **2012**, 100, 978.
- [24] M. A. Hillmyer, *Adv. Polym. Sci.* **2005**, 190, 137.
- [25] M. L. B. Palacio, B. Bhushan, *J. Vac. Sci. Technol. A* **2012**, 30, 050607.
- [26] a) M. Baiardo, G. Frisoni, M. Scandola, M. Rimelen, D. Lips, K. Ruffieux and E. Wintermantel, *J. Appl. Polym. Sci.* **2003**, 90, 1731. b) Y. Hu, M. Rogunova, V. Topolkaev, A. Hiltner, E. Baer, *Polymer* **2003**, 44, 5701. c) Y. H. Na, Y. He, X. Shuai, Y. Kikkawa, Y. Doi and Y. Inoue, *Biomacromolecules* **2002**, 3, 1179.
- [27] a) H. Y. Lu, Z. Li, N. F. Hu, *Biophys. Chem.* **2003**, 104, 623. b) N. F. Hu, *Pure Appl. Chem.* **2001**, 73, 1979. c) C. H. Fan, H. Y. Wang, S. Sun, D. X. Zhu, G. Wagner, G. X. Li, *Anal. Chem.* **2001**, 73, 2850. d) S. Q. Liu, Z. H. Dai, H. Y. Chen, H. X. Ju, *Biosens. Bioelectron.* **2004**, 19, 963.
- [28] a) M. L. Ferrer, F. Del Monte, C. R. Mateo, J. Gomez, D. J. Levy, *Sol-Gel Sci. Technol.* **2003**, 26, 1169. b) K. E. Chung, E. H. Lan, M. S. Davidson, B. S. Dunn, J. S. Valentine, J. I. Zink, *Anal. Chem.* **1995**, 67,

1505. c) D. J. Blyth, J. W. Aylott, D. J. Richardson, D. A. Russell, *Analyst* **1995**, 120, 2725.
- [29] a) F. Febbraio, S. Esposito D'Andrea, L. Mandrich, L. Merone, M. Rossi, R. Nucci, G. Manco, *Extremophiles* **2008**, 12, 719. b) F. Febbraio, L. Merone, G. P. Cetrangolo, M. Rossi, R. Nucci, G. Manco, *Anal. Chem.* **2011**, 83, 1530.
- [30] a) S. M. Zakir Hossain, R. E. Luckham, M. J. McFadden, J. D. Brennan, *Anal. Chem.* **2009**, 81, 9055. b) D. S. Barber, M. Ehrich, *In Vitro Mol. Toxicol.* **2001**, 14, 129. c) A. M. Saleh, C. Vijayasarathy, M. Fernandez-Cabezudo, M. Taleb, G. Petroianu, *J. Appl. Toxicol.* **2003**, 23, 23.
- [31] a) G. Manco, E. Adinolfi, F. M. Pisani, G. Ottolina, G. Carrea, M. J. Rossi, *Biochem.* **1998**, 332, 203. b) G. Manco, G. Carrea, E. Giosue, G. Ottolina, G. Adamo, M. Rossi, *Extremophiles* **2002**, 6, 325.
- [32] a) E. Antonini, M. Brunori, *Hemoglobin and Myoglobin in Their Interactions with Ligands* **1971**, North Holland, Amsterdam. b) K. Imai, *Metalloproteins, Chemical Properties, Biological Effects: Bioactive Molecules* **1988**, C. I. Otsuka and Y. Yamanaka eds, New York: Elsevier, p. 115.
- [33] H. Delincée, B. J. Radola, *Eur. J. Biochem.* **1975**, 52, 321.
- [34] R. E. Childs, W. G. Bardsley, *Biochem. J.* **1975**, 145, 93.
- [35] a) P. D. Darbre, A. E. Romero-Herrera, H. Lehmann, *Biochim. Biophys. Acta* **1975**, 393, 201. b) D. Farnan, D. D. Frey, C. Horvath, *Biotechnol. Prog.* **1997**, 13, 429. c) M. McCoy, K. Kalghatgi, F. E. Regnier, N. Afeyan, *J. Chromatogr. A.* **1996**, 743, 221. d) T. Takano, *J. Mol. Biol.* **1997**, 110, 569.
- [36] J. H. Kim, J. Y. Yoon, *Encyclopedia of Surface and Colloid Science*, **2002**, 4373.
- [37] G. Z. Sauerbrey, *Z. Phys* **1964**, 155, 206.

- [38] a) N. C. Veitch, *Phytochemistry* **2004**, 65, 249. b) K. G. Welinder, *Eur. J. Biochem.* **1978**, 96, 483. c) G. H. Carlsson, P. Nicholls, D. Svistunenکو, G. I. Berglund, J. Hajdu, *Biochemistry* **2005**, 44, 635.
- [39] a) G. M. Abdel Rasoul, M. E. Abou Salem, A. A. Mechael, O. M. Hendy, D. S. Rohlman, A. A. Ismail, *Neurotoxicology* **2008**, 29, 833. b) J. Bajgar, *Adv. Clin. Chem.* **2004**, 38, 151.
- [40] B. Albero, C. Sàncnez-Brunete, J. L. Tadeo, *J. Agric. Food. Chem.* **2003**, 51, 6915.
- [41] a) M. M. Galera, M. D. García, R. S. Valverde, *Talanta* **2008**, 76, 815. b) L. Wang, Y. Liang, X. Jiang, *Bull. Environ. Contam. Toxicol.* **2008**, 81, 377. c) G. Gervais, S. Brosillon, A. Laplanche, C. J. Helen, *Chromatogr. A* **2008**, 1202, 163. d) M. J. Hengel, M. J. Miller, *Agric. Food Chem.* **2008**, 56, 6851.
- [42] G. De Simone, S. Galdiero, G. Manco, D. Lang, M. Rossi, C. Pedone, *J. Mol. Biol.* **2000**, 303, 761.
- [43] a) A. L. Devonshire, *Biochem. J.* **1975**, 149, 463. b) A. L. Devonshire, *Biochem. J.* **1977**, 167, 675. c) C. Mouchès, N. Pasteur, J. B. Bergè, O. Hyrien, M. Raymond, B. R. de Saint Vincent, M. de Silvestri, G. P. Georghiou, *Mosq. Sci.* **1986**, 233, 778.
- [44] a) G. Manco, R. Nucci, F. Febbraio, *Protein Pept. Lett.* **2009**, 16, 1225. b) C. E. Wheelock, B. M. Phillips, B. S. Anderson, J. L. Miller, M. J. Miller, B. D. Hammock, *Rev. Environ. Contam. Toxicol.* **2008**, 195, 117.

### **DIMETHACRYLATE BASED PHOTOPOLYMERIC SYSTEMS MODIFIED WITH A POLYSTYRENE-*BLOCK*-POLY(ETHYLENE OXIDE) COPOLYMER FOR 3D PRINTING**

#### **4.1 Introduction to Chapter IV**

3D printing is one of the possible routes for making a three-dimensional object from a 3D model or other electronic data source primarily through *additive processes* in which successive layers of material are laid down under computer control. The 3D printer used in the present work is the FreeForm Pico (Asiga) (Figure 4.1 A and B). With native XY pixel resolutions down to 27 microns and 250 nanometer Z-axis servo resolution, the Pico is the highest resolution 3D printer available today. The Pico 3D printer uses a solid state UV LED light source and UV curable resin precursors to construct three-dimensional (3D) objects based on computer-designed models (Fig. 4.1 C). The employed manufacturing process, named stereolithography, is schematized in Fig. 4.1 D. Stereolithography (also known as optical fabrication, photo-solidification, solid free-form fabrication, solid imaging and Resin printing) was invented by Chuck Hull in 1986 who patented it as a method for making solid objects by successively “printing” thin layers of an ultraviolet curable material one on top of the other [1].

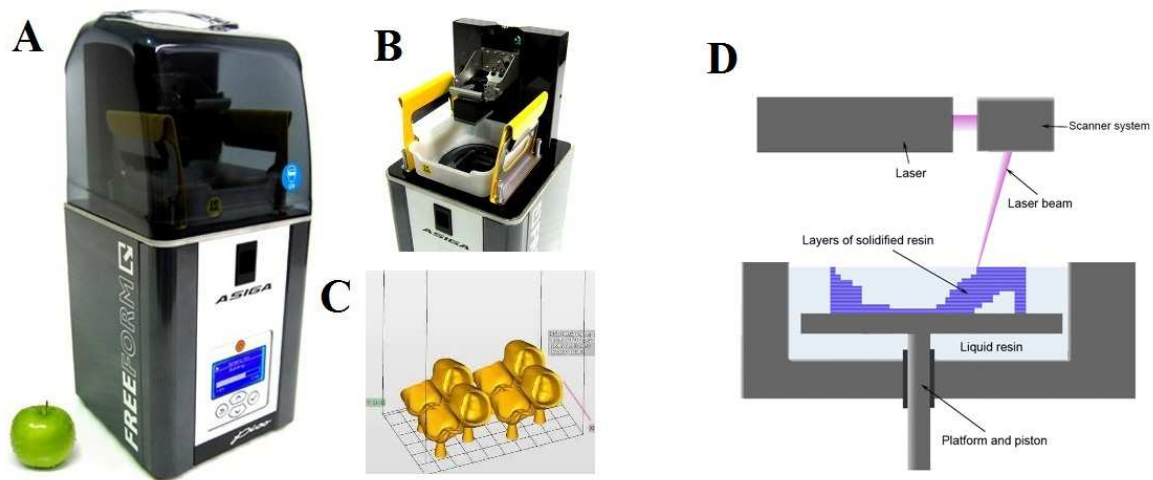


**Fig. 4.1** FreeForm Pico Asiga 3D printer (A) and its opened top-view (B) showing the tray containing the liquid photopolymerizable resin precursors and the elevator platform on which the solid object is constructed. C) Example of computer-designed model that can be used as input in Asiga 3D printer. D) Scheme of the stereolithography process (described in the text).

The process (Fig. 4.1 D) employs a vat of liquid photopolymerizable materials and an ultraviolet laser to build solid parts layer by layer. For each layer, the laser beam traces a cross-section of the part pattern on the surface of the liquid materials. Exposure to the UV laser light cures and solidifies the pattern traced and joins it to the layer below. After the pattern has been traced, the elevator platform descends by a distance equal to the thickness of a single layer, typically 0.05 mm to 0.15 mm. Then, a resin-filled blade sweeps across the cross section of the part, re-coating it with fresh material. On this new liquid surface, the subsequent layer pattern is traced, joining the previous layer. A complete 3D part is formed by this process. Therefore the involved chemistry is the UV curing of a liquid formulation, containing photopolymerizable monomers and/or oligomers, to produce solid densely crosslinked networks (resins) (see paragraph 1.4.3). The formulation also contains an appropriate photoinitiator. It absorbs the UV light and undergoes a photoreaction that produces the reactive energetic species capable of initiating the polymerization of the constituents in the formulation. We have used the commercial formulation by Asiga (PlasClear) (of unrevealed chemical composition) to construct different 3D objects with the Asiga 3D printer (Fig. 4.2 A and B).

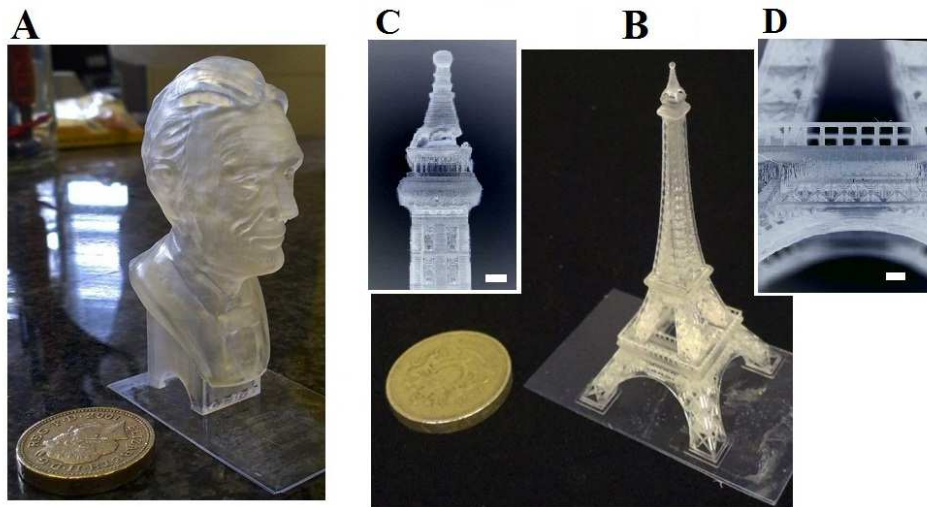


**Fig. 4.2.** Photographs of a bust of Lincoln (A) and a model of the Eiffel Tower (B) printed with Asiga 3D printer. The insets C and D are magnifications, acquired with an optical microscope, of some parts of the printed object (scale bars: 1mm).

In the present thesis work, we have used a formulation containing acrylate unsaturations, in particular a mixture of Bisphenol A bis(2-hydroxy-3-methacryloxypropyl)ether (Bis-GMA) and triethylene glycol dimethacrylate (TEGDMA) (Fig. 4.3 A and B). Bis-GMA (Fig. 4.3 A) is a dimethacrylates ester of Bisphenol A, a long and rigid molecule with reactive carbon-to-carbon double bonds at both ends. Its high molecular weight, relatively high viscosity, and the presence of aromatic groups contribute to the rigidity of the molecular chain. The high viscosity of Bis-GMA is lowered by dilution with TEGDMA (Fig. 4.3 B), a monomer of lower molecular weight; a relatively flexible linear molecule with carbon unsaturated bonds at both ends of lower

The molecule Phenylbis(2,4,6-trimethylbenzoyl)phosphine oxide (Irgacure819) has been used as photoinitiator (Fig. 4.3 C). It is a versatile photoinitiator for radical polymerization of unsaturated resins upon UV light exposure. The mechanism of the reaction, in the case of 1,6-hexanediol diacrylate (HDDA) as diacrylate substrate, is reported in Fig. 4.4 A [2]. We have selected Irgacure819 as photoinitiator because its absorption spectrum (with maxima at 365 and 400 nm) (Fig. 4.4 B) well overlaps with the emission spectrum of the irradiation source used in this work (irradiation wavelength 365 nm) [3]. This overlap is fundamental to the improvement of photochemical reaction efficiency. The formulation we have selected can be used in the 3D printer ASIGA; after 1 min curing in the 3D printer, in fact, the solid cross-linked product is obtained (Fig. 4.4 C).

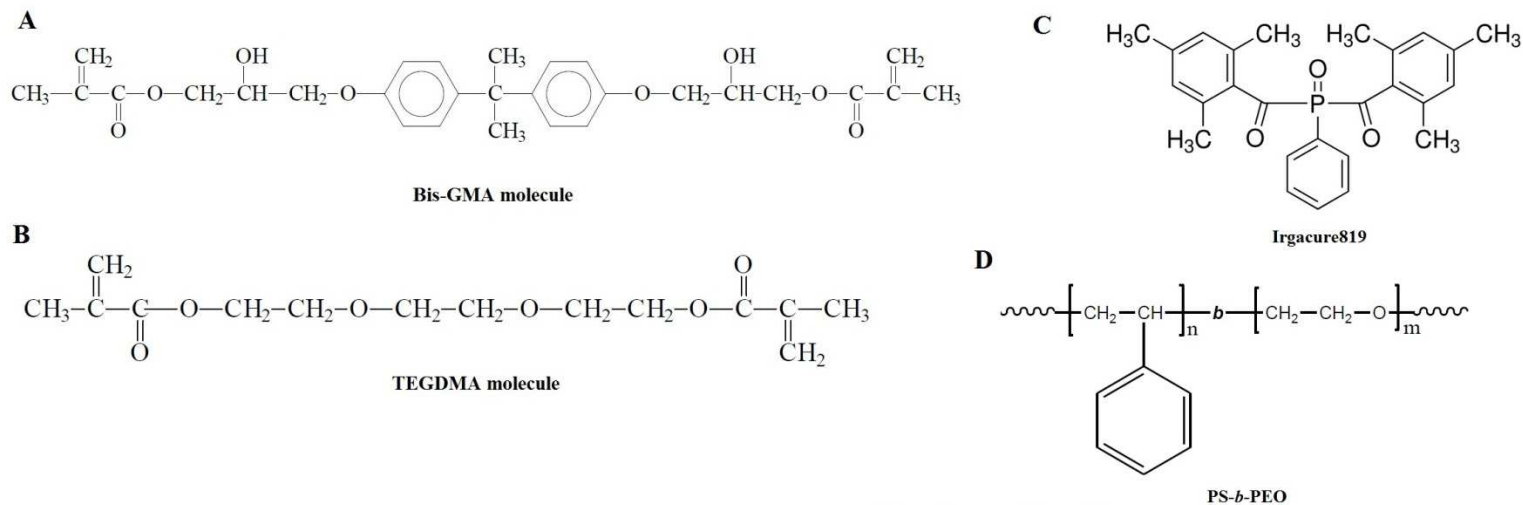


**Fig. 4.3** Structure of the materials employed in the present work. The two acrylate monomers: Bisphenol A bis(2-hydroxy-3-methacryloxypropyl)ether (Bis-GMA) (**A**) and Triethyleneglycol dimethacrylate (TEGDMA) (**B**). The photoinitiator Phenylbis(2,4,6-trimethylbenzoyl)phosphine oxide (Irgacure819) (**C**) and the block copolymer polystyrene-*block*-poly(ethylene oxide) (PS-*b*-PEO) (**D**).

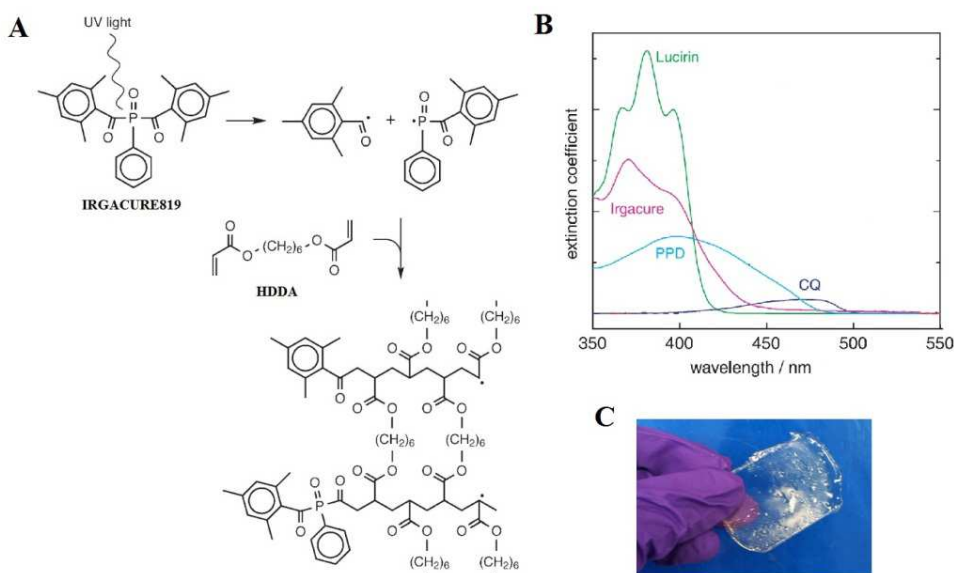


**Fig. 4.4** **A**) Reaction scheme for the photopolymerization of an acrylate oligomer, 1,6-Hexanediol Diacrylate (HDDA), initiated by Irgacure819. When the photoinitiator absorbs photons of UV wavelengths, species with free radicals are produced. These free radicals react with the HDDA monomers to initiate polymerization, until the final solid cross-linked product is formed. Reproduced from [2]. **B**) Extinction coefficients of some commercial photoinitiators; 2,4,6-trimethylbenzoyl-diphenylphosphine oxide (Lucirin), *dl*-2,3-diketo-1,7,7-trimethylnorcamphane (CQ), 1-phenyl-1,2-propanedione (PPD) and phenylbis(2,4,6-trimethylbenzoyl)phosphine oxide (Irgacure). Reproduced from [3]. **C**) Solid product obtained after 1 min curing of our formulation in ASIGA 3D printer.

We have added small amounts of a block copolymer (BCP) in the photopolymerizable formulation in order to evaluate the possibility to induce the formation of nanostructures in the system, without altering the capability of the components to photopolymerize. In particular, we have used a polystyrene-*block*-poly(ethylene oxide) (PS-*b*-PEO) copolymer (Fig. 4.3 D) because of its structural analogy, and therefore miscibility, of one block (PEO) with one component of the resin precursors (TEGDMA) (compare the structures in Fig. 4.3 B and D). Different experimental techniques have been used to characterize the systems before and after UV curing. Fourier transform infrared spectroscopy (FT-IR) and

differential scanning calorimetry (DSC) have been used to determine the levels of conversion and to study the thermal characteristics of the formulations, respectively. Small-angle X-ray scattering (SAXS) experiments have been conducted to underline the presence of a phase separation at nanometer length scale and, finally, transmission electron microscopy (TEM) has been used to study the morphology of some cured samples.

## 4.2 Materials and methods

*Materials.* Bisphenol A bis(2-hydroxy-3-methacryloxypropyl)ether (Bis-GMA), Triethyleneglycol dimethacrylate (TEGDMA) and the photoinitiator Phenylbis(2,4,6-trimethylbenzoyl)phosphine oxide (Irgacure819) have been purchased from Sigma-Aldrich. The block copolymer polystyrene-*block*-poly(ethylene oxide) (PS-*b*-PEO) with number average molecular mass ( $M_n$  in  $\text{Kg mol}^{-1}$ ) of 22.0-21.5 and polydispersity of 1.09 has been purchased from Polymer Source Inc. The volume fraction of the two blocks is  $\sim 50\%$ . At this value of fraction the bulk BCP is able to give rise to a lamellar morphology by self-assembly [4]. The chemical structures of the materials are reported in figure 4.3. All the materials have been used as received without further purification. Four mixtures of these materials have been prepared, the composition of which is shown in Table 4.1. Bis-GMA and TEGDMA have been always used in a ratio 50 : 50 by weight. They have been vigorously stirred for few minutes at around  $60^\circ\text{C}$  and then at room temperature until the mixture appeared clear. The block copolymer PS-*b*-PEO has been added in the mixture BisGMA/TEGDMA and the resulting system vigorously stirred at  $65^\circ\text{C}$  for at least 7 hours.

Using this procedure, samples without block copolymer and samples containing 1, 3 and 6 wt% of BCP have been prepared. Then, in order to make the samples light curable, a fixed amount of the photoinitiator Irgacure819 (0.5 wt% with respect to the photocurable resin precursors, that is the total Bis-GMA and TEGDMA) has been added to each sample. Also in this case magnetic stirring has been used until homogenous, clear yellow systems have been obtained.

**Table 4.1** Names and compositions of the samples used in this study. Bis-GMA and TEGDMA have been always used in a ratio 50 : 50 by weight. The amount of the photoinitiator (Irgacure819) is the same in all the samples, that is 0.5 wt% with respect to the photocurable resin precursors (total of Bis-GMA and TEGDMA).

Sample name	Sample composition (wt%)	
	BisGMA + TEGDMA	PS- <i>b</i> -PEO
Neat resin	100	0
Resin + BCP1	99	1
Resin + BCP3	97	3
Resin + BCP6	94	6

Photopolymerization has been performed by placing the samples in the ASIGA pico flash, that is equipped with an UV light source with a maximum emission wavelength at 365 nm. The source irradiation wavelength is appropriate for the Irgacure819 photoinitiator, that exhibits an absorption maximum at 365 nm (Fig. 4.4 B).

*Fourier transform infrared spectroscopy (FT-IR) measurements.*

The degree of photopolymerization of a very thin film formed by the curable samples has been determined by FT-IR measurements, using a Thermo Scientific Nicolet iS5 FT-IR Spectrometer. A small drop of each sample has been placed between two translucent polyethylene strips, which have been pressed between two CaF<sub>2</sub> crystals to produce a very thin layer. Polyethylene film has been used mainly to avoid adhesion of

the cured resin on CaF<sub>2</sub> crystals and also to prevent oxygen inhibition of polymerization. The samples have been irradiated for successive short periods of time. The FT-IR spectra have been recorded at zero time (before curing) and immediately after each period of exposure to UV-light, in transmission with 128 scans at a resolution of 4 cm<sup>-1</sup>. All experiments have been carried out in triplicate and the results have been averaged.

*Differential scanning calorimetry (DSC) experiments.* DSC has been carried out using a TA Instruments DSC Q2000 Instrument in a flowing N<sub>2</sub> atmosphere. DSC thermograms have been acquired on the as received BCP and on the four samples reported in Table 4.1. For these four samples, DSC thermograms have been acquired both before and after UV curing for ~ 5 min. A scanning rate of 10 °C/min has been used to acquire the first heating, cooling and second heating scans in the range of temperature -90 – 150 °C.

*Small-Angle X-ray Scattering (SAXS) measurements.* The SAXS measurements have been performed at room temperature at beam line BM26B (DUBBLE) located at the European Synchrotron Radiation Facility (ESRF) in Grenoble, France. A sample-detector distance of 2 m and a wavelength of 1.033 Å have been employed to acquire the data. The sample holder scattering has been subtracted from each measurement.

*Transmission electron microscopy (TEM) analyses.* TEM analysis has been carried out in bright field mode using a Philips EM 208S TEM with an accelerating voltage of 100 kV. 70 nm thick ultrathin sections of the cured samples have been obtained at room temperature using a Reichert-Jung Ultracut E Ultramicrotome equipped with a diamond knife. The thin sections have been picked up on carbon coated Cu grid and stained with uranyl acetate.

## 4.3 Results and discussion

### 4.3.1 Fourier transform infrared spectroscopy (FT-IR) measurements

The majority of analyses done to assign conversion in methacrylate resins are based on the use of infrared spectroscopy, which provides a direct measure of unreacted methacrylate groups [4]. Therefore we have used Fourier transform infrared spectroscopy (FT-IR) measurements to determine the degree of photopolymerization of the samples shown in Table 4.1. We have prepared, according to the procedure described in paragraph 4.2, four different samples. The first of them, named “neat resin”, contains only the acrylate monomers (Bis-GMA and TEGMA). The other samples contain also the block copolymer (BCP) at different concentrations, that is 1, 3 and 6 wt%. These samples are named “resin + BCP1”, “resin + BCP3” and “resin + BCP6”, respectively. Obviously, all the samples contain the photoinitiator, Irgacure819, at a fixed concentration (0.5 wt% with respect to the total of photopolymerizable resin precursors).

FT-IR spectra have been recorded for each sample at zero time (before curing) and immediately after a fixed time of exposition to UV-light (curing time). The obtained spectra in the case of the neat resin and of the sample containing 3 wt% of BCP (RESIN + BCP3) are reported in figure 4.5 as an example.

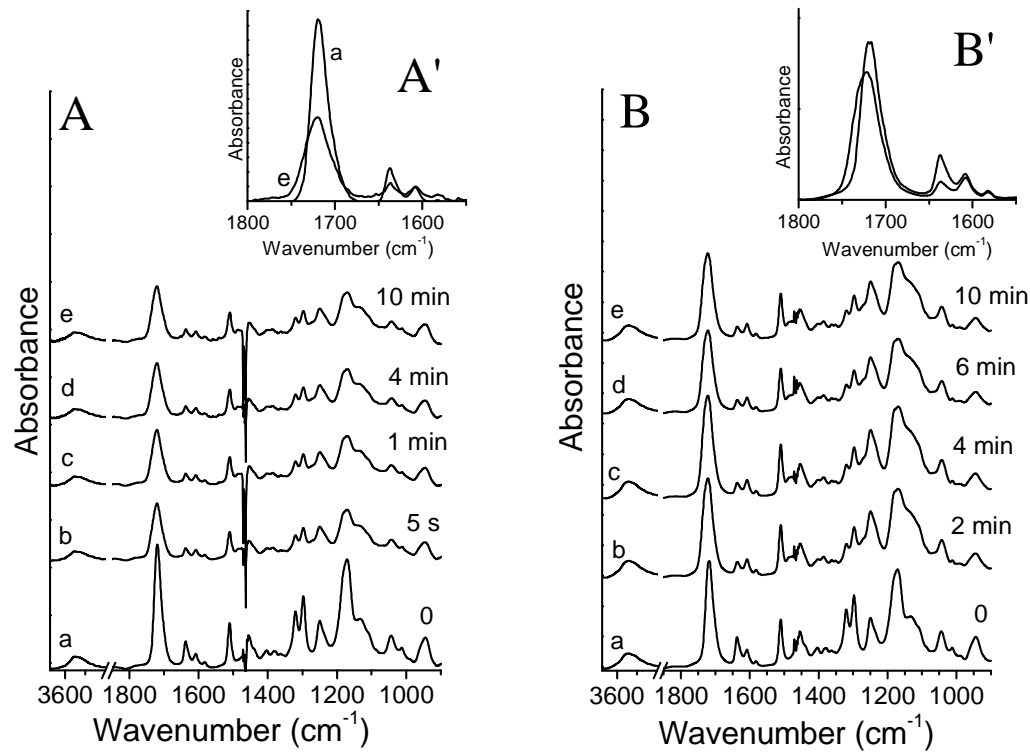


**Fig. 4.5** FT-IR spectra of the Neat Resin (**A, A'**) and of the samples containing 3 wt% block copolymer (**B, B'**), before curing (*a*) and after curing for the indicates times. In **A'** and **B'** the magnifications of the 1800-1550 cm<sup>-1</sup> region in the case of the samples before curing (*a*) and after curing for 10 min (*e*) are reported.

**Table 4.2** Positions and assignments of relevant peaks present in the FT-IR spectra.

Peak position (cm <sup>-1</sup> )	Peak assignment
945	
1045	C-O stretching
1133	
1170	CH <sub>2</sub> bending
1250	C-O stretching and CH <sub>2</sub> rock
1297	
1319	
1456	CH <sub>2</sub> and CH <sub>3</sub> deformation
1608	aromatic C=C bond
1637	aliphatic C=C stretching
1720	C=O stretching
3500	OH stretching

The assignments of main FTIR peaks are reported in Table 4.2. The spectra at low wavenumbers, in the region 1500-900 cm<sup>-1</sup> (fingerprint region) are quite complex and this makes difficult to assign all the absorption bands. The most significant signals in our study occur in the range 1800-1550 cm<sup>-1</sup>. In Fig. 4.5 A', B', magnifications of this region in the case of the samples before curing (curves a of Fig. 4.5) and after curing for 10 min (curves e of Fig. 4.5) are reported. The relevant signals are the aromatic C=C bond (1608 cm<sup>-1</sup>), the aliphatic C=C stretching (1637 cm<sup>-1</sup>) and the carbonyl stretching vibration (1720 cm<sup>-1</sup>). In Figure 4.6 the chemical structure of one of the component formulation (Bis-GMA) is reported, together with the absorption IR wavenumbers of these relevant groups.

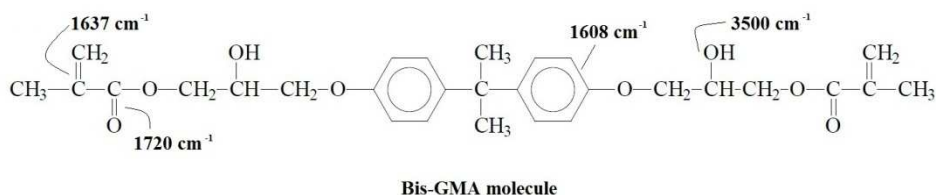


**Fig. 4.6** Structure of Bisphenol A bis(2-hydroxy-3-methacryloxypropyl)ether (Bis-GMA) with indicated the absorption IR wavenumbers of some relevant groups.

The amount of double vinyl bonds remaining in the sample exposed to irradiation is shown by the intensity of the peak at  $1637\text{ cm}^{-1}$  relative to the C=C stretching. The intensity of this peak, in fact, decreases during the photopolymerization (Fig. 4.5 A', B'). Therefore the degree of conversion (*DC*) is directly related to the decrease of  $1637\text{ cm}^{-1}$  absorption band and has been calculated, as a function of curing time, using the equation 4.1:

$$DC(\%) = \left(1 - \frac{R_{cured}}{R_{uncured}}\right) \times 100 \quad \text{where} \quad R = \frac{A_{1637\text{ cm}^{-1}}}{A_{1608\text{ cm}^{-1}}} \quad (\text{Eq. 4.1})$$

where  $A_{1637\text{ cm}^{-1}}$  is the absorption value at  $1637\text{ cm}^{-1}$  and  $A_{1608\text{ cm}^{-1}}$  is the absorption at  $1608\text{ cm}^{-1}$ . The peak at  $1608\text{ cm}^{-1}$  is used as internal standard [4 d] as this adsorption band, assigned to aromatic bonds, does not change as a consequence of polymerization (Fig. 4.5 A', B'). It is worth noting that during the photopolymerization also the position and the intensity of the peak at  $1720\text{ cm}^{-1}$  (assigned to the carbonyl stretching vibration) changes [6]. In the uncured state the carbonyl group is conjugated with the C=C bond (see Fig. 4.6) and upon curing this conjugation is lost. This results in a slight shift of the carbonyl peak to higher wavenumbers in the cured state, as the bond becomes stronger, owing to the fact that the electrons are no longer delocalized. A simultaneous decrease of this peak is also observed in the cured state.

The degree of conversion (*DC*) calculated as a function of curing time for all the samples is shown in Fig. 4.7 and reported in Table 4.3. These data are the averaged over at least three independent measurements experiments. The lowest explored curing time in the case of the samples containing 1 and 3 wt% BCP has been 2 min (curves b and c of Fig. 4.7, respectively). In the case of the neat resin (curve a in Fig. 4.7) and of the

sample containing 6 wt% BCP (curve d of Fig. 4.7) curing times lower than 2 min have been also explored.

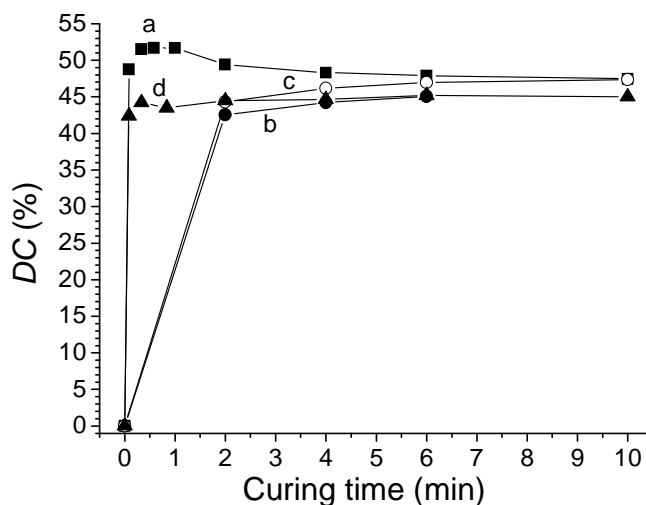


**Fig 4.7** Degrees of conversion (*DC*) vs curing time for the neat resin (*a*, squares) and the samples containing 1 (*b*, circles), 3 (*c*, opened circles) and 6 (*d*, triangles) wt% BCP. The curing times for each sample are reported in table 4.3.

From Fig. 4.7 it is evident that the photopolymerization, under the employed experimental conditions, is a quite fast process, since the degree of conversion reaches already a plateau after a short UV irradiation time, corresponding to 5 s in the case of the neat resin and sample containing 6 wt% BCP (curves a and d of Fig. 4.7). In particular, after 5 s of polymerization, 48.7% and 42.4% of the double bonds is reacted in the case of neat resin and of the sample containing 6 wt% BCP and, after 2 min of polymerization, a degree of conversion of 42.5 and 44.3 % is reached in the case of the samples containing 1 and 3 wt% BCP, respectively (table 4.3). The neat resin shows the highest *DC* (average value 49.6%). The introduction of the block copolymer doesn't significantly influence the degree of conversion. The *DC* average values

are, in fact, 43.9, 46.1 and 44.2 % in the case of the samples containing 1, 3 and 6 wt% of BCP, respectively.

**Table 4.3** Degrees of conversion (*DC*) observed at different curing time for all the samples.

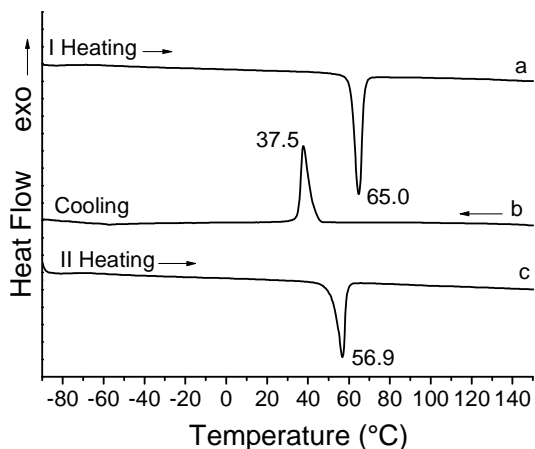
Curing time	<i>DC</i> (%)			
	Neat resin	Resin + BCP1	Resin + BCP3	Resin + BCP6
5 s	48.7	/	/	42.4
20 s	51.5	/	/	44.2
35 s	51.7	/	/	/
50 s	/	/	/	43.5
1 min	51.6	/	/	/
2 min	49.4	42.5	44.3	44.4
4 min	48.3	44.2	46.1	44.6
6 min	47.9	45.0	46.9	45.2
10 min	47.4	/	47.3	45

The room-temperature polymerization of dimethacrylates usually leads to glassy resins in which only a part of the available double bonds are reacted. This is due to the fact that the mobility of the reacting medium decreases as the polymerization proceeds. In particular, as the degree of cross-linking increases, the propagation step, which involves the reaction of small monomer molecules with macroradicals, becomes more difficult because unreacted pendant double bonds, macroradicals and free monomer become trapped among network units and completely immobilized. As a consequence, these systems are characterized by a maximum limiting conversion, which is significantly less than unity, in spite of the presence of unreacted double bonds and trapped radicals. On the basis of literature data, the limiting degree of conversion, calculated for a system with a composition similar to our resin, is 60.9 % [4 a]. This indicates that the *DC* values achieved by our systems (about 50% in the case of the neat resin and 45% in the case of the resins containing the BCP) may be considered good.

### 4.3.2 Differential scanning calorimetry (DSC) experiments

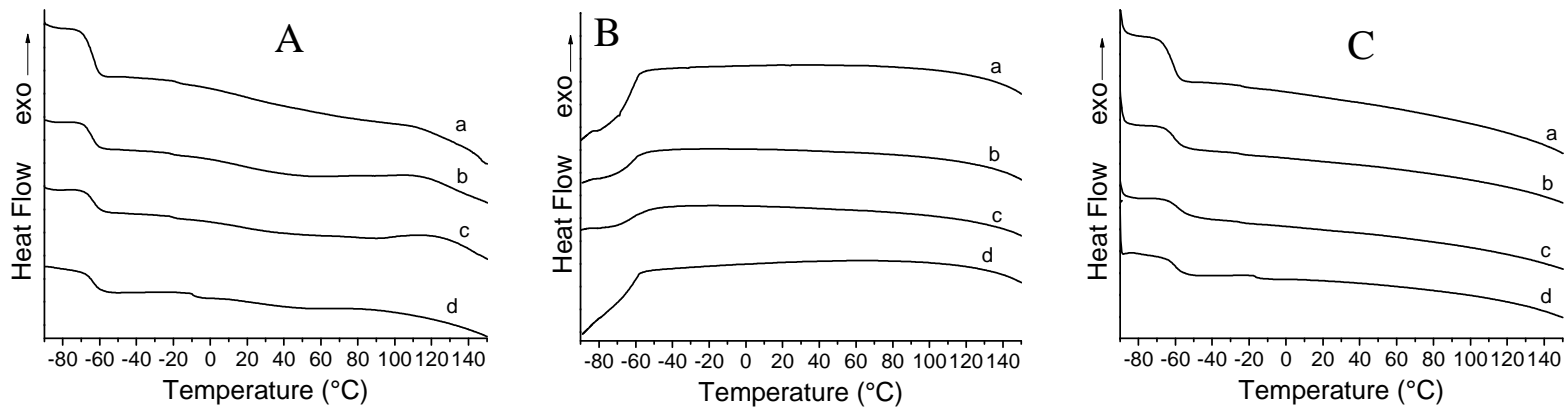
Differential scanning calorimetry (DSC) experiments have been carried out on the as received block copolymer (BCP) and on the four mixtures reported in Table 4.1. For these four samples, DSC thermograms have been acquired both before and after UV curing for ~ 5 min.

The DSC analysis (first heating, cooling and second heating scans) of the as received BCP, polystyrene-*block*-poly(ethylene oxide) (PS-*b*-PEO), is reported in figure 4.8. The PS-*b*-PEO copolymer is semicrystalline, with PEO and PS being the crystalline and amorphous blocks, respectively, as confirmed by the wide angle X-ray scattering (WAXS) profile reported in Fig. A4.1 of the appendix. In the first heating scan (curve a of Fig. 4.8) the endothermic peak, due to the melting of the crystalline PEO, is present at 65.0 °C. The exothermic peak due to the crystallization of the PEO block appears in the cooling scan at 37.5 °C (curve b of Fig. 4.8), in agreement with literature data [7]. Finally, the melting peak in the second heating scan occurs at 56.9 °C (curve c of Fig. 4.8). The glass transition temperatures ( $T_g$ ) of PS and PEO domains, expected at 107 and -65 °C, respectively, are not well discernible in Fig. 4.8.



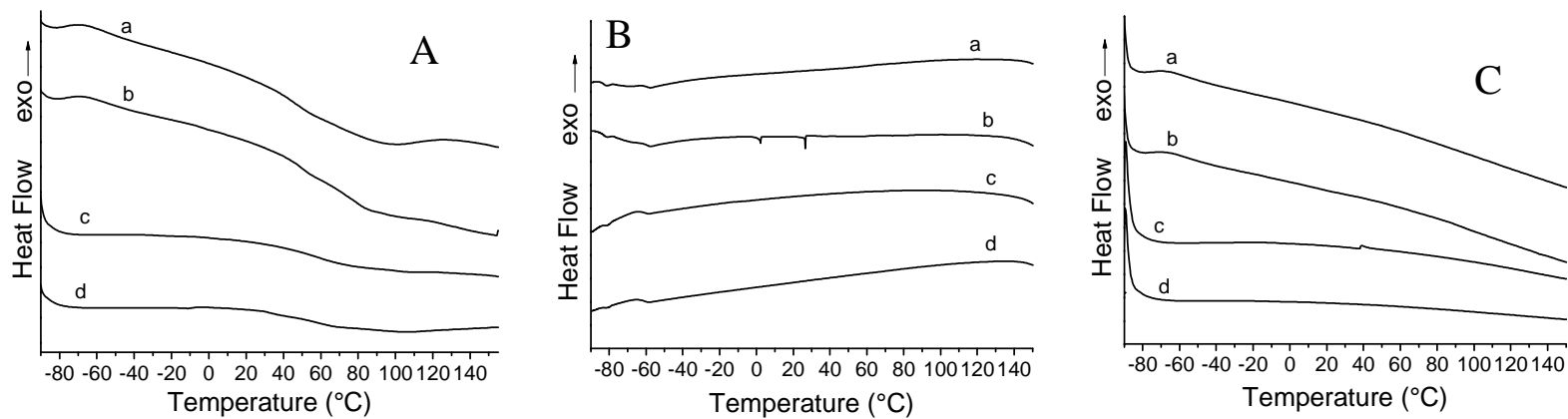
**Fig. 4.8** DSC thermogram of the as received PS-*b*-PEO block copolymer (scanning rate, 10°C/min).

Figure 4.9 shows the first heating (A), cooling (B) and second heating (C) DSC scans of the four samples reported in Table 4.1 before curing. All the samples display a glass transition temperature ( $T_g$ ) of about  $-65\text{ }^\circ\text{C}$ , typical of TEGDMA/Bis-GMA uncured mixture [5 *a*], and no endothermic or exothermic peaks. As previously discussed, PEO is a semicrystalline polymer with a melting point of  $65\text{ }^\circ\text{C}$  (Fig. 4.8). The absence of melting and crystallization peaks in the DSC thermograms of samples containing the BCP (curves b-d of Fig. 4.9) suggests that the PEO block is unable to crystallize because PEO chains are well dispersed in the acrylate formulations.



**Fig. 4.9** First heating (A), cooling (B) and second heating (C) DSC scans of the samples before curing; neat resin (*a*) and samples containing the BCP (*b-d*). The concentrations of the BCP are 1 (*b*), 3 (*c*) and 6 (*d*) wt%. Scanning rate, 10°C/min.

The samples have been cured at room temperature by exposition to UV-light for ~ 5 min and the DSC thermograms of the cured samples have been acquired (Fig. 4.10). As expected, the DSC thermograms dramatically change after the curing of the samples. All specimens show a broad endotherm, centred at around 80 °C, in the first heating scans (Fig. 4.10 A) that can be due either to the occurrence of cross-linking reactions activated by the increase of mobility during heating and/or to the large heterogeneities segmental dynamics at the glass transition temperature ( $T_g$ ) of the partially cross-linked networks. The  $T_g$ , in fact, is usually not easily detectable by DSC in the case of cured dimethacrylates, due to the intrinsic broadness of the transition region [8]. The  $T_g$  is an important physical property of cured matrices [9]. The polymerization of multifunctional monomers produces network polymers with highly heterogeneous environments as they contain densely cross-linked regions alternate to less densely cross linked regions. This heterogeneity results in a broad distribution of motilities or relaxation times [10]. No relevant transition is detected in the cooling (Fig. 4.10 B) and second heating (Fig. 4.10 C) scans, confirming that the heating of the UV cured samples increases the cross-linking density of the network.



**Fig. 4.10** First Heating (A), cooling (B) and second heating (C) DSC scans of the samples after curing for ~ 5 min; neat resin (a) and samples containing the BCP (b-d). The concentrations of the BCP are 1 (b), 3 (c) and 6 (d) wt%. Scanning rate, 10°C/min.

### 4.3.3 Small-Angle X-ray Scattering (SAXS) and transmission electron microscopy (TEM) experiments

Small-Angle X-ray Scattering (SAXS) measurements have been performed to characterize the microphase structures of the samples. The room temperature SAXS profile of the as received PS-*b*-PEO BCP is reported in figure 4.11A. Multiple orders of Bragg reflection are observed, indicating a phase separated morphology at nanoscale. In particular, the first (1), third (3) and fifth (5) order reflections of the lamellar (Lam) morphology appear (see table 2.2), as expected for a BCP with volume fraction of blocks around 50 % [11]. The SAXS positions of the peaks and the lamellar periodicity are reported in Table 4.4.

SAXS experiments have been conducted also on the neat resin and on the samples containing 1 and 3 wt% BCP, before and after UV curing. The room temperature SAXS profiles acquired before curing are reported in figure Fig. 4.11 B. No peaks appear in the SAXS profile of the neat resin (curve a of Fig. 4.11 B), indicating the absence of a phase separation at nanoscale due to complete miscibility between the components of the resin (BisGMA and TEGDMA). Scattering peaks are instead observed for the samples containing the BCP, indicating the presence of a phase separation at nanometer length scale. In particular, one broad peak centered at  $0.23 \text{ nm}^{-1}$  is observed in the case of the sample containing 1 wt% BCP (curve b of Fig. 4.11 B) whereas two peaks centered at  $0.14$  and  $0.24 \text{ nm}^{-1}$  are present in the SAXS profile of the sample containing 3 wt% BCP (curve c of Fig. 4.11 B). The SAXS positions of the peaks and the domain spacing corresponding to the peaks ( $d_i$ ) are reported in Table 4.4.

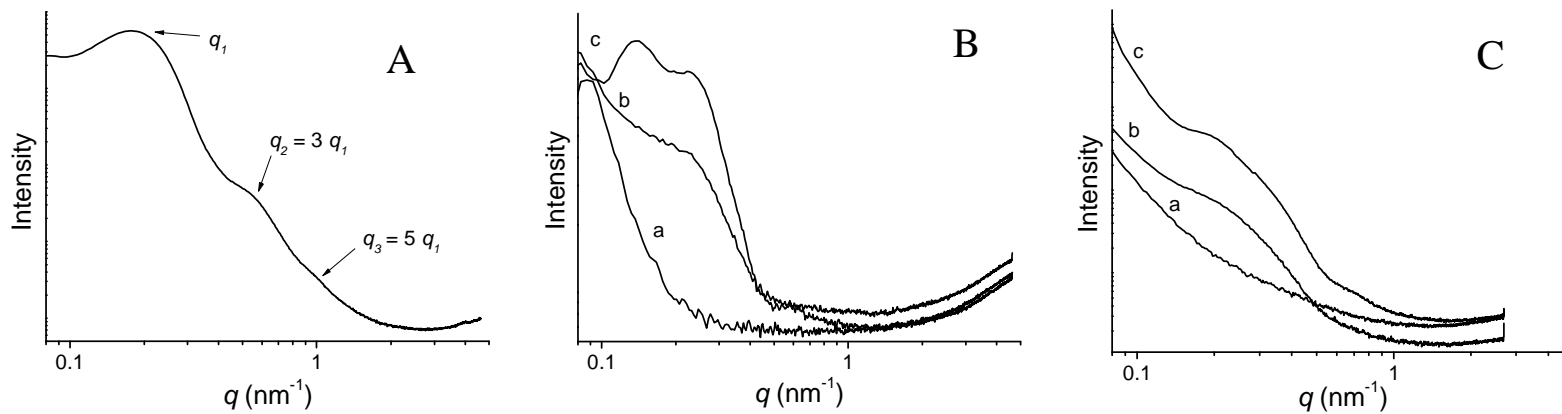


**Fig. 4.11** Room temperature SAXS profiles in logarithmic scale of the as received BCP (A) and of the samples before (B) and after (C) curing in the case of the neat resin (a) and the samples containing 1 (b) and 3 (c) wt% BCP. In A the peaks at  $q_2 = 3 q_1$  and  $q_3 = 5 q_1$  typical of the lamellar morphology are indicated.

**Table 4.4** SAXS peak positions ( $q$ ) and  $d$ -spacings ( $d$ ) for the indicated samples. Values obtained from the SAXS profiles of Fig 4.11.

Sample	$q_1$ (nm <sup>-1</sup> )	$q_2$ (nm <sup>-1</sup> )	$q_3$ (nm <sup>-1</sup> )	$d_1, d_2, d_3$ (nm)
Neat BCP <sup>(a)</sup>	0.19	0.56	0.95	33, 11, 7
Resin + BCP1 before curing	0.23	/	/	27
Resin + BCP3 before curing	0.14	0.24	/	45, 26
Resin + BCP1 after curing	0.27	/	/	23
Resin + BCP3 after curing	0.21	0.37 (shoulder)	/	30

(a)  $q_2 = 3 q_1$  and  $q_3 = 5 q_1$

Since the mixtures of photopolymerizable resin precursors and PS-*b*-PEO BCP are transparent at room temperature, no phase separation occurs at macroscopic scale. However, at nanometric length scale, the good miscibility of PEO with Bis-GMA and TEGDMA and the scarce affinity of PS with the mixture probably leads to formation of micellar aggregates characterized by a PS core covalently linked to PEO chains placed at the interface with the not cured photopolymerizable components.

The SAXS profiles acquired after UV curing are reported in figure Fig. 4.11 C. Again, no scattering peaks are observed in the case of the neat resin (curve a of Fig. 4.11 C) indicating that the cured system in absence of BCP remains isotropic at nanometer length scale. Broad peaks appear in the profiles of the samples containing the BCP (curves b and c of Fig. 4.11 C) indicating that the nanoscale structure formed in the pre-cure stage (Fig. 4.11 B) is roughly retained after the UV curing. In particular, a broad peak, corresponding to a spacing of 23 nm, is present in the sample containing 1 wt% BCP (curve b of Fig. 4.11 C) as in the case of the profile acquired before curing (curve b of Fig. 4.11 B). In the case of the sample containing 3 wt% BCP (curve c of Fig. 4.11 C), a broad peak at 0.21 nm<sup>-1</sup> and a faint shoulder at ~ 0.37 nm<sup>-1</sup> appear. Therefore the morphology of the corresponding uncured mixture (curve c of Fig. 4.11 B) is only partly retained in the cured system probably

because the cross-linking reaction induces a break-out of the initial nanostructure.

The presence of a phase separation at nanometer scale in the case of the sample containing the BCP has been confirmed by transmission electron microscopy (TEM). TEM images of 70 nm thin sections of the neat resin and of sample containing 3 wt% BCP after 10 min UV curing are reported in Fig. 4.12 A and B, respectively. In order to achieve a good contrast between the different components of the resin, the thin sections have been stained with uranyl acetate.

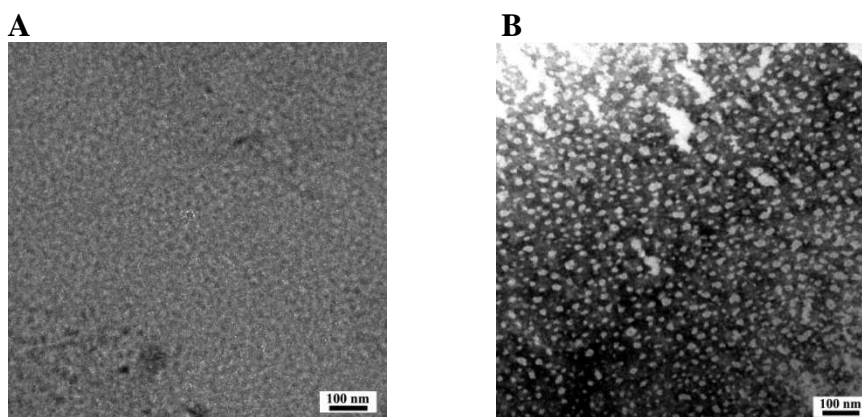


**Fig. 4.12** TEM images of 70 thin sections of the neat resin (**A**) and of the sample containing 3 wt% BCP (**B**). Both samples have been subjected to 10 min UV curing. Staining with uranyl acetate has been performed before the TEM observation.

No phase separation is observed in the case of the neat resin (Fig. 4.12 A), whereas the nano phase separation is evident in the case of the sample containing the BCP (Fig. 4.12 B). In this case bright pseudo-spherical domains with diameters ranging from 10 to 25 nm, most likely due to PS aggregates, appear in a dark matrix. The center-to-center distance between the bright domains obtained from TEM image of Fig. 4.12 B (~30 nm) well agrees with the dimension of the nanoscopic phase separation resulting from SAXS data (Table 4.4), confirming the hypothesis that PS domains tend to form micellar aggregates fringed with PEO chains.

## 4.4 Conclusions to Chapter IV

An investigation of acrylate photopolymerizable formulations modified with small amounts of PS-*b*-PEO block copolymer (BCP) has been conducted. The influence of the BCP addition on the chemical and thermal properties of the formulations has been evaluated both before and after UV curing by different techniques (FT-IR, DSC). Notably, nanostructured systems have been obtained by adding the BCP in the formulations, without strong alteration in the capability of the resin to photopolymerize. The nanoscale organization is present both before and after the UV induced photopolymerization, as confirmed by SAXS and TEM experiments. A new effect has been identified in the use of a BCP as additive in photopolymerizable resin precursors, involving a phase separation at nanometric length scale via micelle formation before cross-linking, followed by partial break out of the nanostructure upon irradiation and consequent formation of the glassy network.

Our experimental findings are interesting for the study of processing-morphology-property relationships in these complex systems, to develop new principles for creating structures of controlled length scales that would result in novel materials with distinct (and unusual) properties.

## BIBLIOGRAPHY CHAPTER IV

- [1] C. W. Hull, *Apparatus for Production of Three-Dimensional Objects by Stereolithography* **1986**, U.S. Patent 4575330.
- [2] J. Muskin, M. Ragusa, T. Gelsthorpe *J. Chem. Educ.* **2010**, 87, 512.
- [3] M. G. Neumann, C. C. Schmitt, G. C. Ferreira, I. C. Corrêa, *Dental Materials* **2006**, 22, 576.
- [4] F. S. Bates, G. H. Fredrickson, *Annu. Rev. Phys. Chem.* **1990**, 41, 525.
- [5] a) I. Sideridou, V. Tserki, G. Papanastasiou, *Biomaterials* **2002**, 23, 1819. b) J. D. N. Filho, L. T. Poskus, J. G. A. Guimarães, A. A. L. Barcellos, E. M. Silva, *Journal of Oral Science* **2008**, 50, 315. c) J. W. Stansbury, S. H. Dickens, *Dental Materials* **2001**, 17, 71. d) F. Heatley, Y. Pratsitsilp, N. McHugh, D. C. Watts, H. Derlin, *Polymer* **1995**, 36, 1859.
- [6] S. Chambers, J. Guthrie, M.S. Otterburn, J. Woods, *Polym. Commun.* **1986**, 27, 209.
- [7] E. A. Grulke, J. Brandup, E. H. Immergut, *Polymer Handbook* **1999** Wiley, New York.
- [8] W. D. Cook. *Polymer* **1992**, 33, 2152.
- [9] J. C. S. Moraes, M. M. D. S. Sostena, C. R. Grandini. *The Glass Transition Temperature in Dental Composites, Metal, Ceramic and Polymeric Composites for Various Uses* **2011**, Dr. J. Cuppoletti Ed., ISBN: 978-953-307-353-8, InTech, DOI: 10.5772/21289.
- [10] A. R. Kannurpatti, K. J. Anderson, J. W. Anseth, C. N. Bowman, *Journal Polymer Science Part B: Polymer Physics* **1997**, 35, 2297.
- [11] a) F. S. Bates, G. H. Fredrickson, *Annu. Rev. Phys. Chem.* **1990**, 41, 525. b) I. W. Hamley, V. Castelletto, *Prog. Polym. Sci.* **2004**, 29, 909.

---

---

## CONCLUSIONS

---

---

In the present thesis different classes of nanomaterials based on di-block copolymers (BCPs) have been studied, with the purpose to design, characterize and fabricate functional nanostructures to be used as active elements in selective sensing and/or biosensing devices with high sensitivity.

The work has been mainly focused on the creation of two classes of BCP based materials: nanocomposite materials, characterized by the selective inclusion of functional nanoparticles (NPs) in specific BCP nanodomains, and nanoporous materials able to act as ideal support for the physical immobilization of specific biomolecules. Also, an explorative study regarding the use of BCPs as additives in photopolymerizable resins has been conducted.

Regarding the first class of materials (**Chapter II**), we have reported a simple method to fabricate ordered arrays of palladium (Pd) nanoclusters and palladium oxide (PdO) nanoparticles with tunable dimensions and lateral spacing by using cylinder forming polystyrene-*block*-poly(ethylene oxide) copolymers (PS-*b*-PEO) as both stabilizers for Pd nanoparticles and templates controlling the distribution of them. The cylindrical self-assembled nanostructure formed from PS-*b*-PEO block copolymers has been used as *host* for selectively sequestering a nanoparticles precursor (palladium(II) acetate) in PEO domains. Then, two different methods have been used to obtain Pd NPs from the precursor in presence of the BCPs: electron irradiation of the thin films

containing the BCPs and palladium precursor, and solution reduction by thermal treatment before thin films preparation. In both cases, highly ordered nanocomposite thin films containing Pd NPs selectively included in hexagonally packed cylinders of PEO blocks have been obtained. Then, PdO nanoparticles of improved stability against aggregation have been obtained on a solid and conductive support (silicon wafer) by treating the films in air at elevated temperatures. We were able to modulate the dimensions of Pd nanoclusters and PdO NPs and their inter-distance by using as template two different PS-*b*-PEO copolymers having different molecular mass of both PS and PEO block.

This part of the thesis work is an example confirming that the ability to control the length and the spatial and orientational organization of block-copolymer morphologies makes these materials particularly attractive as scaffolds for engineering of ordered nanocomposites in which the distribution of the guest particles is guided by the ordering of the host matrix. The ability to create morphologically and dimensionally controlled Pd and PdO nanoparticles would be the key point in the process of transforming these systems from promising materials into integrated devices and the compatibility of these systems with the existing silicon-based technology makes them even more attractive.

Regarding the second class of materials (**Chapter III**), we have optimized a procedure that allows building nanoporous thin film with well-defined architecture containing functionalized pores delimited by hydrophilic walls, exploiting self-assembly of lamellar block copolymers and the concept of sacrificial block. We have employed a blend of polystyrene-*block*-poly(L-lactide) (PS-*b*-PLLA) and polystyrene-*block*-poly(ethylene oxide) (PS-*b*-PEO) diblock copolymers to generate thin

films with lamellar morphology in which the PEO and PLLA blocks form lamellae within a PS matrix. Then, by selective chemical etching of the PLLA block, the nanoporous thin film, patterned with nanometric channels containing pendant hydrophilic PEO chains, has been generated. We have demonstrated that our nanoporous surfaces constitute the ideal support for the physical absorption of proteins such as myoglobin (Mb) and peroxidase from horseradish (HRP), largely used in electrochemical and optical sensing devices. The porous structure is beneficial for the loading of a large amount of myoglobin and HRP enzyme. In the case of HRP we have demonstrated that confinement resulted in a noticeable improvement of its catalytic performance and long term stability. Furthermore, we have evaluated the possibility to use our nanoporous materials as support to immobilize esterase 2 (EST2) from *Alicyclobacillus acidocaldarius*, able to act as active element in biosensors for the detection of specific organophosphate pesticides (OPs) like paraoxon, that is one of the most used pesticides in agriculture and also widely studied for its neurotoxic, cancerous, and teratogenic effects. After optimizing the experimental conditions to physically absorb the enzyme EST2 on our nanoporous thin films without an excessive loss of its hydrolytic activity, we have performed some experiments for the determination of paraoxon by immobilized EST2. Preliminary results are quite promising and suggest that the enzyme immobilized on our porous support could be used as active layer of a biosensor for the detection of organophosphate compounds.

The developed BCPs-based approach for building nanoporous patterned surfaces is a robust and versatile tool useful not only in applicative research for fabrication of lab-on-chip biosensors, but also in basic research to study the adsorption mechanism of proteins in

constrained environment with controlled geometry at fundamental level. Therefore a new research line has been initiated aimed at the use of neutron reflectivity to understand the process of protein adsorption onto porous surfaces with tailored pores geometry.

Finally, in **Chapter IV** we have studied a photopolymerizable formulation containing acrylate unsaturations, in particular a mixture of Bisphenol A bis(2-hydroxy-3-methacryloxypropyl)ether (Bis-GMA) and triethylene glycol dimethacrylate (TEGDMA) and we have added small amount of a PS-*b*-PEO block copolymer to the formulation in order to evaluate the possibility to induce a nanostructuration in the system. Different experimental techniques have been used to characterize the systems before and after UV curing. We have found that the introduction of the block copolymer induces a phase separation in the system at nanometer length scale both before and after UV curing. We successfully have tested the developed formulations in a high resolution commercial 3D printer. A new effect has been identified in the use of a BCP as additive in photopolymerizable resin precursors, involving a phase separation at nanometric length scale via micelle formation before cross-linking, followed by partial break out of the nanostructure upon irradiation and consequent formation of the glassy network. These results suggest significant potential for the use of block copolymers as additives in photopolymerizable acrylate formulations, in order to build nanostructured resins that could eventually improve the final properties of these materials and their range of application.

In conclusion, the present thesis work has confirmed that the self-organization of block copolymers offers a wide variety of methods for structuring and functionalizing materials on the nano length scale. The

spontaneous self-assembly of BCPs has been used to prepare a large number of tailor-made nanostructured materials, that can be used as nanoscopic device components, templates or active layers in biosensors, demonstrating the unparalleled versatility of these materials in the creation of nanostructured materials that could overcome several of the intrinsic limitations of current top-down fabrication technologies.



# APPENDIX



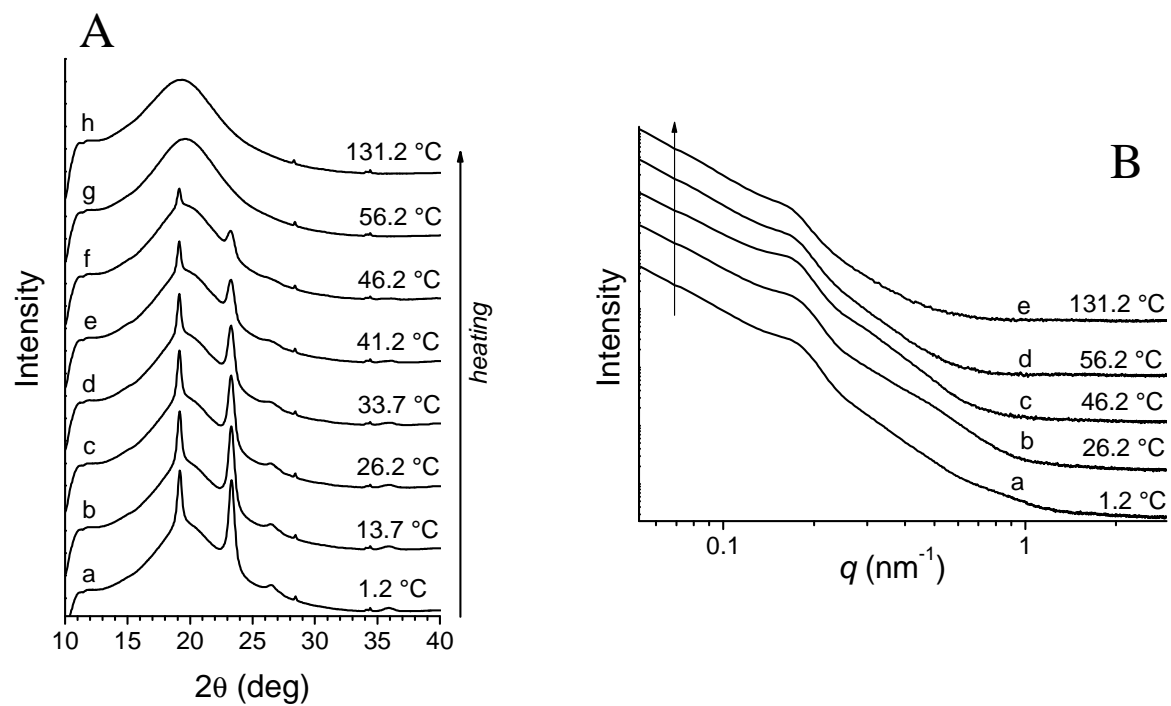


**Fig. A2.1** WAXS profiles (A) and SAXS data in logarithmic scale (B) of the as received SEO sample acquired during the second heating scan at the indicated temperatures (scanning rate, 5 °C/min).

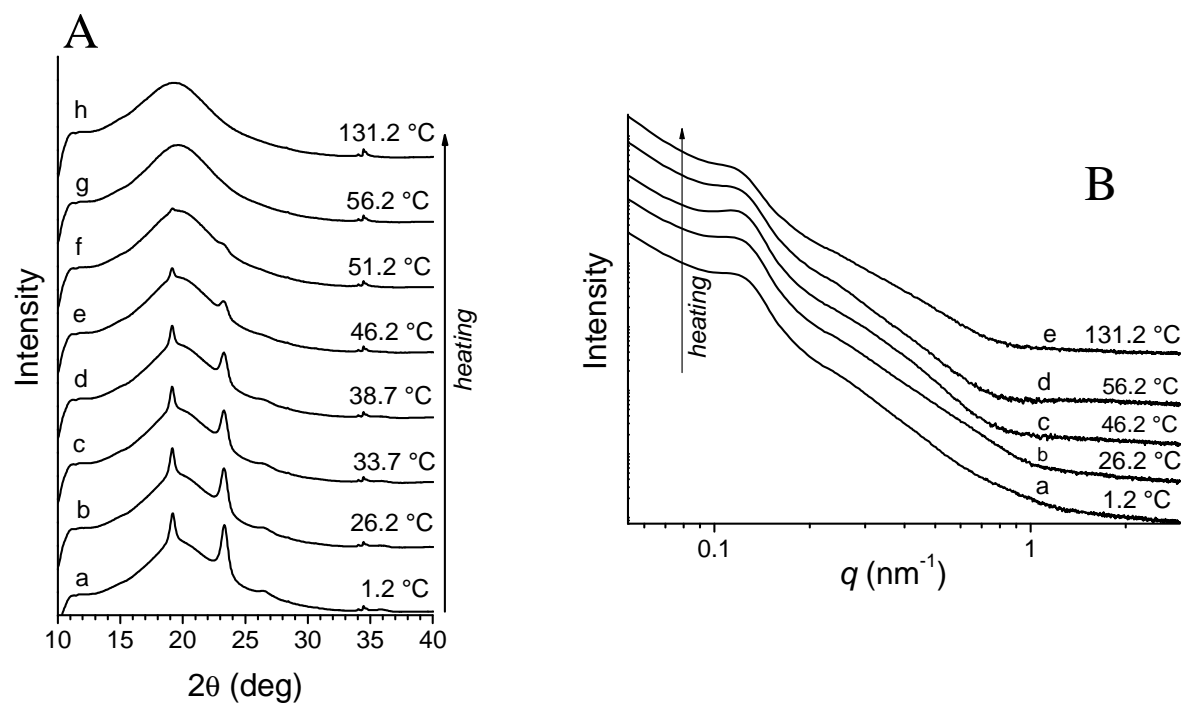


**Fig. A2.2** WAXS profiles (A) and SAXS data in logarithmic scale (B) of the as received HSEO sample acquired during the second heating scan at the indicated temperatures (scanning rate, 5 °C/min).

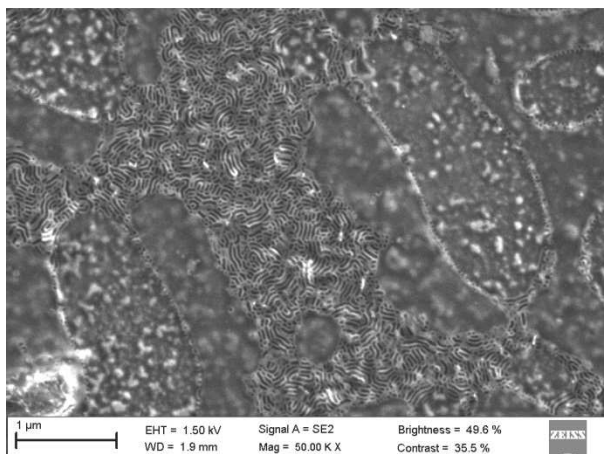


**Fig. A3.1** SEM image of an etched PS-*b*-PLLA thin film. The film has been prepared by spin coating a solution (1wt% in DCE) of PS-*b*-PLLA on a silicon wafer and then by immersing the so prepared thin film into a 0.5 M sodium hydroxide water/methanol solution (60:40 by volume) at 65°C for 30 seconds.

### A 3.2 Linearization of the kinetics data of Myoglobin adsorption

The linearized Langmuir equation (Eq.3.2) is

$$\frac{\Gamma_m}{\Gamma} = \frac{1}{KC} + 1 \quad (\text{Eq. A.1})$$

that can be transformed into

$$\frac{C}{\Gamma} = \frac{1}{K\Gamma_m} + \frac{C}{\Gamma_m} \quad (\text{Eq. A.2})$$

Eq. A.2 suggests that the kinetic adsorption data of Fig. 3.13 can be linearized by plotting  $C/\Gamma$  vs  $C$ , as shown in Fig. A3.3. For incubation time less than 15 min no regular behavior is observed, probably because the equilibrium surface coverage is not reached. However, for incubation times higher than 15 min the adsorption kinetics (at 5 and 10 °C) can be described in terms of an equilibrium Langmuir behavior with parameters  $K = 1$  and  $\Gamma_m = 2.7$  due to the formation of a monolayer.

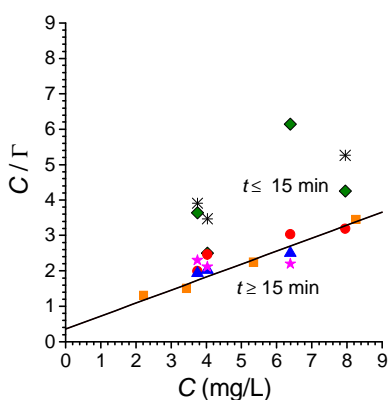


**Fig. A3.2** Fit of Mb kinetic adsorption data on nanoporous supports of Fig. 3.13 using the linear form of the Langmuir equation (Eq. A.2). The solid line corresponds to  $\Gamma_m = 2.7$  and  $K = 1$  as indicated in Table 3.2. The data have been obtained at 5 °C, except for the incubation time 30 min where a temperature of 10 °C has been used. Incubation times: 5 (\*), 15 (◆), 30 (■), 45 (●), 60 (▲) and 75 (★) min.

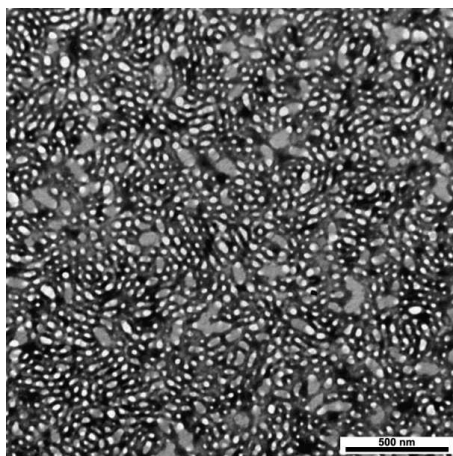


**Fig. A3.3** Bright-field TEM image of a thin film of the blend PS-*b*-PLLA/PS-*b*-PEO prepared on a gold support. The film has been prepared by spin coating a solution (1 wt% in DCE) of PS-*b*-PLLA/PS-*b*-PEO (90/10 w/w) on a gold support, then the film has been transferred on a TEM grid and stained with RuO<sub>4</sub> before observation.

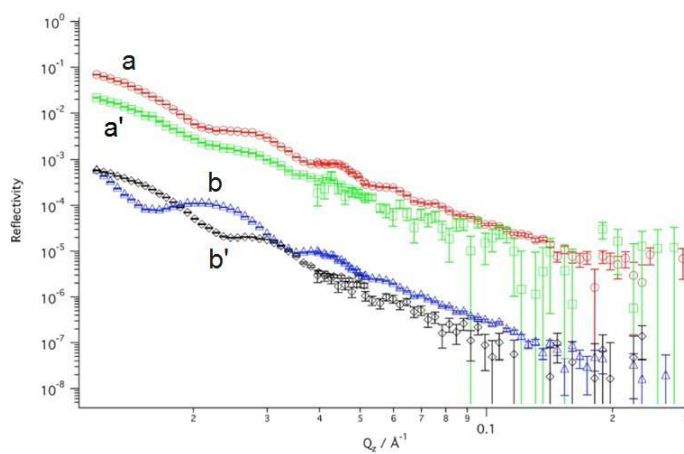


**Fig. A3.4** Reflectivity profiles of the non etched blend (*a*, *a'*) and etched blend (*b*, *b'*) before (*a*, *b*) and after (*a'*, *b'*) after adsorption of Mb from a 0.23 μM solution. The profiles have been acquired in H<sub>2</sub>O contrast. The measurements have been performed at the Institut Laue-Langevin (ILL, Grenoble, France) using the FIGARO reflectometer.

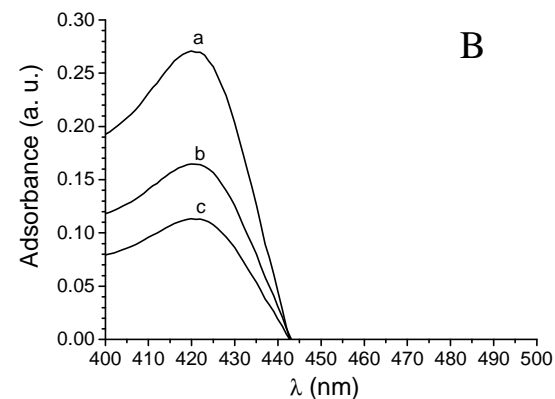
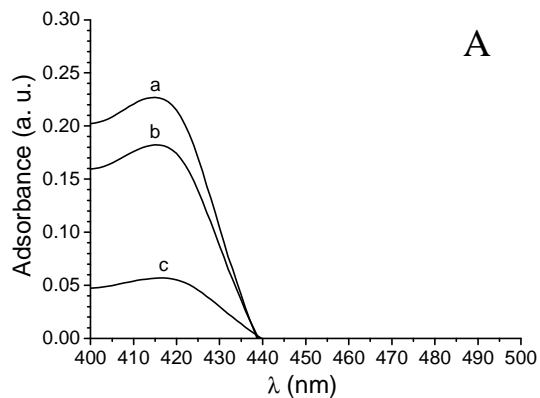


**Fig. A3.5** UV-Visible spectra of the ABTS/ABTS<sup>••</sup> solutions retrieved after 5 minutes of contact with the HRP enzyme immobilized on the etched blend (*a*), PS (*b*) and the glass slide (*c*). **A**) The activity test has been performed using an ABTS and H<sub>2</sub>O<sub>2</sub> concentration of 0.245 mM and 9.75 mM, respectively. The enzyme incubation time is 150 min. **B**) The activity test has been performed using an ABTS and H<sub>2</sub>O<sub>2</sub> concentration of 2.45 and 0.0975 mM, respectively. The enzyme incubation time is 90 min.

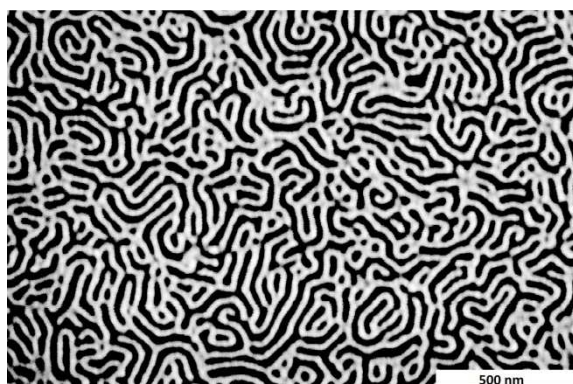


**Fig. A3.6** SEM image of the etched blend after the EST2 enzyme immobilization using an incubation time of 6 days and subsequent test activity with *p*-NP-C4.

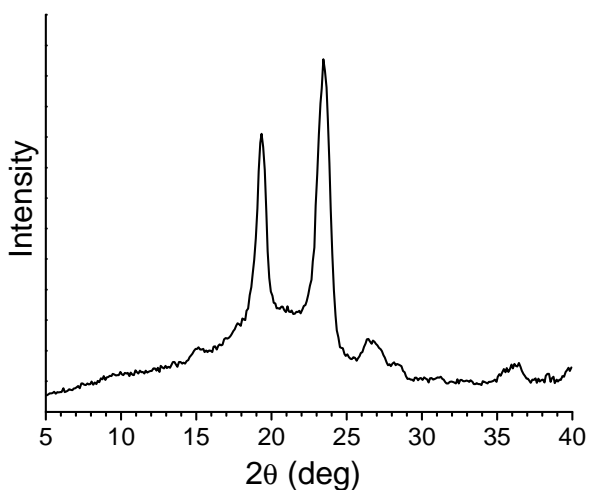


**Fig. A4.1** Wide angle X-ray scattering (WAXS) profile of the as received PS-*b*-PEO copolymer. The diffraction pattern shows two distinct peaks centred at  $2\theta \approx 19$  and  $23^\circ$ , characteristic of PEO. These peaks are superposed to an amorphous halo due to the contribution of amorphous phases of PEO and PS blocks.